Development of High Efficiency Bulk Heterojunction Organic Solar Cell and Hydrogen Fuel Cell

A Dissertation Presented

by

Cheng Pan

to

The Graduate School

in Fulfillment of the

Requirements

for the Degree of

Doctor of Philosophy

in

Materials Science and Engineering

Stony Brook University

December 2013

Stony Brook University

The Graduate School

Cheng Pan

We, the dissertation committee for the above candidate for the

Doctor of Philosophy degree, hereby recommend

acceptance of this dissertation.

Miriam H. Rafailovich
Distinguished Professor, Materials Science and Engineering

Jonathon Sokolov
Professor, Materials Science and Engineering

Dilip Gersappe
Professor, Materials Science and Engineering

Chang-Yong Nam
Assistant Scientist, Brookhaven National Laboratory

This dissertation is accepted by the Graduate School

Charles Taber
Dean of the Graduate School

Abstract of the Dissertation

Development of High Efficiency Bulk Heterojunction Organic Solar Cell and Hydrogen Fuel Cell

by

Cheng Pan

Doctor of Philosophy

in

Materials Science and Engineering

Stony Brook University

2013

With the urgency to conserve finite fossil fuels and control the carbon release within the framework of Kyoto agreement regarding global warming effect, the society shows great interest for the renewable energy. Varieties of energy generation devices using renewable energy sources are then created. However, most of the technologies are still at early stage and the applications of these devices are limited due to their relatively low efficiency and high cost.

For bulk heterojunction (BHJ) solar cell, the disordered morphology within the active layer for conventional BHJ solar cell construction significantly prevents the free movement of charge carriers, leading to low short circuit current and power conversion efficiency. In this thesis, a novel approach that introduces polystyrene that organizes the poly(3-hexylthiophene) (P3HT) into columnar phases decorated by [6,6]-phenyl C61-butyric acid methyl ester (PCBM) at the interface is presented. This structure represents a realization of an idealized morphology of an organic solar cell, in which, both exiciton dissociation and the carrier transport are optimized leading to increased power conversion efficiency. This feasibility of this idea was first tested by Molecular Dynamics (MD) simulations and then experimentally realized by optimization of ratios between P3HT, PS and PCBM. Columnar structure inside the polymer blends thin film was observed under TEM cross section measurement and the power conversion efficiency was indeed increased by 30% by constructing this specific structure inside active layer of BHJ solar cell.

For polymer electrolyte membrane (PEM) fuel cell, the utilization of expensive platinum (Pt) catalysts limits the cost efficiency while the poisoning effect of Pt catalyst by the impurities in reforming hydrogen gas shortens the lifetime of the fuel cell. In this thesis, thiol-stabilized gold nanoparticles are synthesized through classic two-phase method and a monolayer of as prepared gold nanoparticles is deposited onto the surface of Nafion® membrane by Langmuir-Blodgett (LB) trough. X-ray reflectivity (XRR) determines the thickness of the monolayer and the fuel cell performance results show that the monolayer deposition of gold nanoparticles could not only enhance the output power of PEM fuel cells significantly (up to 80%) but also increase the tolerance to the impurities in hydrogen gas, which is probably due to the active perimeter sites at the interface of gold and Nafion® membrane support proven by output gas analysis. Further research shows that the activity of this deposited layer is a strong function of surface pressure that's applied for nanoparticles deposition, which indicates the important of direct contact between nanoparticles and membrane support. Meanwhile, similar construction of GO or rGO monolayer onto membrane surface can also greatly increase the output power of PEM fuel cells with even lower cost than the application of gold nanoparticles, which is mainly due to the enhanced ion conductivity for GO deposition and enhanced electron conductivity for rGO deposition.

Table of Contents

List of Figures

List of Tables

List of Abbreviations

PV	photovoltaic
eV	electron voltage
Si	silicon
D	electron donor
A	electron acceptor
PCE	power conversion efficiency
HOMO	highest occupied molecular orbital
LUMO	lowest unoccupied molecular orbital
FF	fill factor
CdTe	cadmium telluride
CdS	cadmium sulfide
CIGS	copper indium gallium selenide
GaAs	gallium arsenide
DSSC	dye sensitized solar cell
TCO	transparent conducting oxide
TiO_2	titanium dioxide
Pt	platinum
Al	aluminum
Au	gold
Mg	magnesium
Ca	calcium

ITO	indium tin oxide
BHJ	bulk heterojunction
P3HT	poly (3-hexylthiophene-2,5-diyl)
PCBM	[6,6]-Phenyl C_{61} butyric acid methyl ester
MD	molecular dynamics
TEM	transmission electron microcopy
HRTEM	high resolution transmission electron microscopy
Fcc	face centered cubic
AFM	atomic force microscopy
NR	neutron reflectivity
PEMFC	polymer electrolyte membrane fuel cell
CO	carbon monoxide
CO_2	carbon dioxide
H_2	hydrogen
O_2	oxygen
DFT	density functional theory
H_2O	water
MEA	membrane electrode assembly
GO	graphene oxide
rGO	reduced graphene oxide

Acknowledgments

I would first thank my advisor, Prof. Miriam H. Rafailovich. She is a fantastic mentor throughout my research in Stony Brook University. She can indicate the right way for me when I was lost in my research and she is always willing to discuss with me about my new research ideas and topics. She also encourages and supports me to present my research results in national conferences, which significantly benefits my academic career.

I would also thank my committee members, Prof. Sokolov, Prof. Gersappe and Dr. Nam. Prof. Sokolov helped me a lot with equipment build up and troubleshootings. Prof. Gersappe provided solid theoretical explanations for the experimental results, which constitutes the important part of my research. Dr. Nam guided me how to assemble a high efficient polymer solar cell device in Brookhaven National Lab. In addition, their comments and suggestions provided on my dissertation and thesis defense have been extremely helpful and definitely will result in a significantly improved dissertation.

I would thank my collaborators. Prof. Yimei Zhu and Dr. Kim Kisslinger from Brookhaven National Lab helped me with the transmission electron microscopy characterization of my samples, which lead to a nanometer scale scope of the structures on the surface and interface. Dr. Sushil Satjia and Dr. Bulent Akgun from National Institute of Standards and Technology helped me with the neutron scattering, which greatly enhanced my understanding with diffusion between different polymer layers. Steve Bennett from Brookhaven National Lab helped me with the X-ray reflectivity. Hazem Tawfik from State University of New York at Farmingdale helped me with the industry use fuel cell test. Di Xu and Dr. Joseph Ortiz helped me with the theoretical

simulations for my research. Cameron Akker contributes to the research on graphene-derivative fuel cell.

I would like to thank all the previous and current members of Prof. Rafailovich’s group for their kind help. I want to thank Dr. Ying Liu, Dr. Chang-Chueh Chang, Hongfei Li, Zhenhua Yang, Sisi Qin, Kai Yang, Liudi Zhang, Yingjie Yu, Yichen Guo, Linxi Zhang, Yan Xu, Ke Zhu. We have been working together for a long time and experienced a wonderful time. I also want to thank all my friends that I met in Stony Brook.

Finally, I should thank my family. Without their love and support, I would not be able to finish my Ph.D. study. I want to give special thanks to my wife, Tianyuan Wu, who is always accompanying and encouraging me to conquer all the obstacles on the road.

Publications

1. **C. Pan**, H. Li, K. Kao, S. Qin, M. H. Rafailovich. “Gold Nanoparticles Enhancement for Polymer Electrolyte Membrane Fuel Cell”, in preparation
2. **C. Pan**, H. Li, C. Akker, M. H. Rafailovich. “Langmuir-Blodgett Film of Graphene-derivatives on Improving the Performance of Polymer Electrolyte Membrane Fuel Cell”, in preparation
3. **C. Pan**, H. Li, B. Akgun, S. K. Satijia, Y. Zhu, D. Xu, J. Ortiz, D. Gersappe, and M. H. Rafailovich. “Enhancing the Efficiency of Bulk Heterojunction Solar Cells via Templated Self-Assembly”, *Macromolecules* 46 (2013) 1812-1819
4. R. Isseroff, A. Chen, S. Chittabathini, A. Tse, **C. Pan**, B. Goldman, H. Li, B. Akhavan, J. Sokolov, and M. Rafailovich. “Increasing Polymer Solar Cell Active Layer Efficiency and Organization by Adding Gold-Functionalized Reduced Graphene Oxide”, *MRS Online Proceedings Library* 1500 (2013): mrsf12-1500
5. Z. Wu, K Yu, Y. Huang, **C. Pan**, and Y. Xie. “Facile solution-phase synthesis of γ-Mn”, *Chemistry Central Journal* 1 (2007) 8
6. Z. Wu, **C. Pan**, T. Li, G. Yang, and Y. Xie. “Formation of uniform flowerlike patterns of NiS by macrocycle polyamine assisted solution-phase route”, *Crystal Growth and Design* 7 (2007) 2454-2459
7. Z. Wu, **C. Pan**, Z. Yao, Q. Zhao, and Y. Xie. "Large-scale synthesis of single-crystal double-fold snowflake Cu2S dendrites." *Crystal Growth & Design* 6 (2006) 1717-1719
8. Z. Wu, Z. Xi, **C. Pan**, Z. Yao, and Y. Xie “Synthesis and characterization of beta-Ni (OH)(2) flower-like patterns”, *CHINESE JOURNAL OF INORGANIC CHEMISTRY* 22 (2006) 1371-1374

Chapter 1

Prologue

1.1 Summary

Fossil fuels, including coal, petroleum, and natural gas, have been dominant energy sources for decades and contributed significantly for the development of the society. They are generated by anaerobic decomposition of buried plants or animals over millions of years, so they are considered as non-renewable energy sources. With the growing energy consumption every year, the exploited fossil fuels can hardly meet the demands pressure from both industry and daily life. In addition, the utilization of fossil fuels unavoidably brings the environmental issues, such as global warming effect and air/water pollution. These factors make it urgent to find renewable and clean energy sources as alternative choices. Solar energy and hydrogen fuel are top promising candidates since both of them are renewable, clean and abundant. With the most recent development in catalyst synthesis and morphology control, the efficiency of devices using these energy sources is enhanced significantly, which accelerates the commercial application of such devices. In this chapter, related technologies are discussed

1.2 World's energy consumption

There are five main energy sources that are consumed to meet the demands, including liquids (crude oil and biofuels), coal, natural gas, renewables (wind, solar, hydro, etc.) and nuclear. Based on the recent released International Energy Outlook 2013 (IEO 2013) report by U.S. Energy Information Administration (EIA) [1], the world energy consumption will grow by 56 percent between 2010 and 2040, reaching over 700 quadrillion Btu (1 quadrillion Btu = 1.055×10^{18} J). Although renewable energy and nuclear power are the fastest growing energy sources, increasing by 2.5 percent every year, fossil fuels will still supply almost 80 percent of world energy use in 2040, which is around 560 quadrillion Btu.

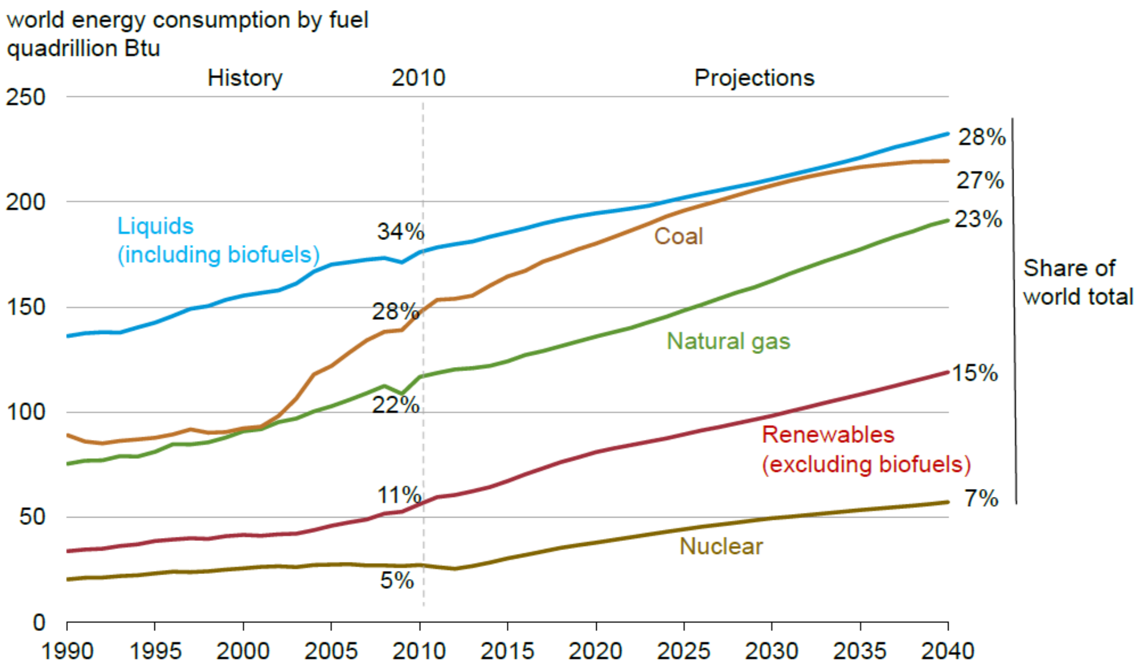

Figure 1-1 World energy consumption by fuel from 1990 to 2040. Reproduced from Ref [1]

However, as mentioned above, fossil fuels are non-renewable energy sources and their reserves are limited on earth. The proved reserves of fossil fuels are listed in Table 1-1 based on the BP's "Statistical Review of World Energy" published in mid 2013 [2]. Considering the world's energy consumption rates discussed above, the crude oil will be used up by the year of 2065 and the natural gas will be extracted three years after that. The reserves of coal will be the last one to be exhausted, but only persist for 50 years more. Therefore, it is very urgent to find alternative energy sources with huge reserves or renewable properties to satisfy nearly 80 percent of world's energy demands due to the exhaustion of fossil fuels.

Table 1-1 World's Reserves of Fossil Fuels and Estimated Years of Extraction Remaining

Energy sources	Total proved reserves	Years of extraction remaining
Coal	860938 million tonnes	109
Natural Gas	187 trillion cubic meters	56
Crude Oil	1669 thousand million barrels	53

Renewable energy includes sunlight, wind, hydro and geothermal heat etc. The reserve of renewable energy on earth, especially solar power and wind power, is much more than fossil fuels. Furthermore, renewable energy is available to generate electricity in rural areas that are far away from the national electricity grid. Therefore, renewable is very capable of replacing fossil fuels as energy consumption sources. However, limited by the cost and technology of utilization, only about 11% of global final energy consumption comes from renewable energy sources (excluding biofuels) in 2010, according the report provided by EIA. This share is expected to rise to 15% in 2040 based on the current growing of renewable energy, but still not enough to significantly reduce the reliance on fossil fuels. Accelerating the development of renewable energy related technology is in high demand.

1.3 Environmental effects

Due to the chemical components of fossil fuels, combustion of those fuels generates carbon dioxide and nitrogen oxides, which are the main components of greenhouse gases. Currently, more than 90% greenhouse gas release In U.S. comes from the combustion of fossil fuels [3]. The distribution of carbon dioxide emissions by types of fossil fuels is shown in Figure 1-2. The greenhouse gases absorb and emit radiation within the thermal infrared range. When these gases are concentrated in atmosphere, the earth is covered by a thicker thermal insulation shell and becomes warmer than it is supposed to be.

The growing carbon dioxide emissions has already lead to the increase of carbon dioxide concentration in atmosphere from 280 ppm in 1750 to 392 ppm in 2012 [4], and achieved highest increase rate during the last 800,000 years. Considering the current policies and regulations, the world's carbon dioxide emissions are estimated to increase 46 percent by 2040, reaching 45 billion metric tons per year [1]. To slow down the accumulation of greenhouse gases in atmosphere, an international treaty which is called Kyoto Protocol was prompted in 1998 by United Nations to set binding obligations on most countries to reduce emissions of greenhouse gases [5]. Since the main sources of greenhouse gases come from the combustion of fossil fuels, it is necessary to reduce the share of fossil fuels in world's energy consumption.

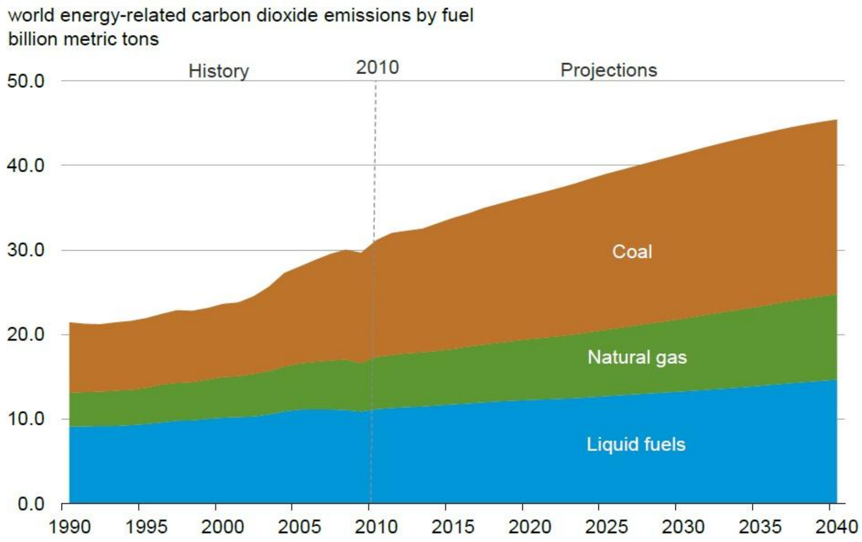

Figure 1-2 World energy-related carbon dioxide emissions by types of fuels, reproduced from Ref [1]

Renewable energy performs much better than fossil fuels regarding the environmental aspects. In most cases, utilization of renewable energy generates no emissions, such as solar power, wind power, hydro power or harmless emissions, such as hydrogen fuel cell (only pure water is released). This feature makes renewable energy a very environmentally friendly energy source to use.

1.4 Solar energy

Solar energy is normally referred as radiant light and heat from the sun. The incoming solar energy to the earth is approximately 439 EJ (1 EJ = 1.0×10^{18} J) per hour, which is almost equal to the whole primary energy use in the year of 2010 [6]. Apart from the energy that is reflected and absorbed by atmosphere, more than 50% of the solar energy travels through the atmosphere and is applicable for utilization [7].

The use of solar energy can trace back to the ancient time when humans learned to use woods as fuel to start and keep fire. This is actually indirect application of solar energy since most plants that grow on earth absorb sunlight and convert it to chemical energy in the form of components consist of carbon, oxygen and hydrogen, which is commonly called as "photosynthesis" (the most common chemical reaction equation is shown in Equation 1-1) [8].

$$6\mathrm{CO_2} + 6\mathrm{H_2O} + \text{light energy} \rightarrow \mathrm{C_6H_{12}O_6} + 6\mathrm{O_2} \tag{1-1}$$

The as produced components can support the activities of living plants and will be released as heat energy during combustion of the plants or their residuals. With the exploration of similar biological materials that can also be used in the same way to generate energy, all these materials are classified as "biomass", which refers to the biological materials derived from living, or recently living organisms, and they can either be used directly via combustion to produce heat or indirectly used to be converted to different forms of biofuels. Currently only approximately 1.5% of global energy production comes from a solar source, and most of it is through biomass [9]. In most rural areas of developing countries, biomass is still the main incoming source of energy for their daily life.

The second way of using solar energy is called as "concentrating solar power basics". Concentrating solar power technology use mirrors to reflect and focus sunlight onto receivers that collect solar energy and convert it to heat [10]. This thermal energy can be utilized to heat water or air for heating in buildings. In the 1980s, solar water heaters were being used all over the United States since they were proved to be a big improvement over wood and coal-combustion stoves. However, as large deposits of oil and natural gas were discovered and became available at low cost, these solar water systems began to be replaced by heaters burning fossil fuels. This concentrating solar power technology can also be used to produce electricity [11]. A highly curved mirror is used to focus the sunlight on a tube that contains flowing water. The temperature inside tube becomes very high and boils water into steam, which can then be used to drive a conventional steam-turbine to generate electricity.

Photovoltatic technology is a very important application of solar energy, which directly converts solar power to electricity due to the photovoltatic effects for semiconductors [12]. When the sunlight is incident upon the surface of semiconductor materials, the electrons that stay at the valence band absorb photons from sunlight and are excited to the conduction band. As a result, this leaves behind a positively charged electron hole, which attracts the excited electron by Coulomb force and forms an exciton. Due to the force of electrical field built up due to the P-N junction in the semiconductor, the electron and hole are separated and the electrons can be captured in the form of electric current [13]. The energy consumption from photovoltaic power has reached 67.4 GW in 2011 and is growing very fast [14]. Conventional solar cells are mostly made from crystalline silicon and are the most efficient. Second-generation solar cells are called thin-film solar cells since they are made from amorphous silicon and nonsilicon materials such as copper indium gallium selenide (CIGS) [15]. The layers of these thin film solar cells are only a few micrometers thick and possess good flexibility, which makes it promising for building integration and other special purposes [16]. The third-generation solar cells are made from variety of new materials, including solar dyes and photoactive polymers. Besides flexibility and light weight features, these solar cells are 1,000 times thinner than silicon cells and the production process is usually under room temperature [17], which means much less energy consumption compared to silicon solar cells production. Moreover, most of these solar cells are produced by solution process method, making them much easier to manufacture than silicon ones [18]. However, due to the low power conversion efficiency, these third generation solar cells are not cost effective enough for wide applications. How to enhance the efficiency of them is one of the major goals of this thesis.

1.5 Hydrogen fuels

As the lightest element on the earth, pure hydrogen possesses the highest energy density by weight (123 KJ/kg) among all available fuels [19]. In fact, hydrogen is an energy carrier, like electricity, rather than an energy source, because it does not exist naturally and must be manufactured via gas reforming, electrolysis or other specific ways [20]. Limited by the energy conversion law, hydrogen production always requires more energy than can be retrieved from the hydrogen as a fuel afterwards [21]. Even though, hydrogen is still considered as renewable energy due to its extraordinarily huge reserve on earth and benefit to the environment. Hydrogen is the most abundant chemical element on earth, and most of it exists in molecules such as water and organic compounds because hydrogen readily forms covalent compounds with most non-metallic elements [22]. Varieties of technology have been developed to produce pure hydrogen from water or hydrogen rich organic compounds, which makes the sources of pure hydrogen become incredibly wide [23][24]. Moreover, the utilization of hydrogen as fuels is very environmentally friendly. From the chemical Equation 1-2 for the usage of hydrogen fuel in combustion engine or hydrogen fuel cells, the only by products are water and heat (there may be little amount of nitrogen oxides generated during combustion of hydrogen fuels due to the high temperature and nitrogen exists in the air) [25].

$$2H_2(g) + O_2(g) \rightarrow 2H_2O(l) + 286kJ/mol \quad (1\text{-}2)$$

Since the combustion of pure hydrogen can release a lot more power than fossil fuels with the same weight of fuel loading, it is first utilized as the fuels to power the rockets into the space [26]. Hereafter, with the wide application of polymer electrolyte membrane that can conduct hydrogen ions through the membrane, the hydrogen fuel cells have been developed and widely applied on portable devices, transportation vehicles, backup power and distributed generation due to its light weight, high energy density and low operation temperature [27].

The primary hydrogen production method used in industry is through steam reforming, which consumes non-renewable sources, such as coal and natural gas, to produce hydrogen. The chemical reaction for natural gas reforming is shown in Equation 1-3, 1-4 [28].

$$CH_4 + H_2O \leftrightarrow CO + H_2 \quad (1\text{-}3)$$

$$CO + H_2O \rightarrow CO_2 + H_2 \quad (1\text{-}4)$$

As one of the fossil fuels, natural gas is non-renewable sources and has limited reserve. Moreover, this process generates considerable carbon release. Therefore, this traditional way of producing hydrogen is somehow opposite to the primary purpose, which requires renewable and clean energy. Moreover, the outlet gas from gas reforming usually contains up to 25% of carbon dioxide in the hydrogen gas and removal of it to achieve high purity is very costly [29]. Instead of gas reforming, water electrolysis is a much more environmentally friendly way to generate hydrogen. The chemical reaction for water electrolysis is shown in Equation 1-5. The precursors are only pure water and some electrolytes (usually alkaline, such as sodium hydroxide). Under the direct electrical current, water can be split to hydrogen gas and oxygen gas. Since the outlet gas from hydrogen generator is hydrogen with some alkaline solution, it is very easy to separate them and get very pure hydrogen (purity higher than 99.9%) [30]. The challenge remains for this

$$2\mathrm{H_2O} \xrightarrow{\text{Electricity}} 2\mathrm{H_2} + \mathrm{O_2} \tag{1-5}$$

method is the cost and the source of the electricity. Currently, the average electricity consumption to produce 1 cubic meter (under standard condition) is 4.5 kWh [31], which is still much higher than natural gas considering the cost to generate same amount of energy. Moreover, 75% of the electricity is generated by combustion of fossil fuels all over the world [32]. If the electricity that used for water electrolysis comes from combustion of fossil fuels, it does not actually solve the problem. Therefore, renewable energy sources, such as solar energy and wind energy, are used to provide electricity for hydrogen manufacture [33][34]. Since the power generated by solar or wind is intermittent and difficult to store, converting these renewable energy to hydrogen and use it to reproduce energy when necessary is actually a good solution for energy storage. In this way, the hydrogen fuel can finally be considered as a renewable fuel for application. Although there is only 5% of commercial hydrogen is produced renewably now, this area is attracting attention and growing very fast [35].

References

[1] Conti, J. J., P. D. Holtberg, J. A. Beamon, S. A. Napolitano, and A. M. Schaal. "Annual Energy Outlook 2013 with Projections to 2040." *US Energy Information Admin., Washington, DC, Rep. EIA-0383* (2013).

[2] Petroleum, British. "BP statistical review of world energy." *Retrieved September* 9 (2008): 2008.

[3] Meinshausen, Malte, Nicolai Meinshausen, William Hare, Sarah CB Raper, Katja Frieler, Reto Knutti, David J. Frame, and Myles R. Allen. "Greenhouse-gas emission targets for limiting global warming to 2 C." *Nature* 458, no. 7242 (2009): 1158-1162.

[4] Pearson, Paul N., and Martin R. Palmer. "Atmospheric carbon dioxide concentrations over the past 60 million years." *Nature* 406, no. 6797 (2000): 695-699.

[5] Grubb, Michael, Christiaan Vrolijk, Duncan Brack, and Tim Forsyth. *The Kyoto Protocol: a guide and assessment*. London: Royal Institute of International Affairs, 1999.

[6] Crabtree, George W., and Nathan S. Lewis. "Solar energy conversion."*Physics today* 60, no. 3 (2007): 37-42.

[7] Tiwari, G. N., ed. *Solar energy: fundamentals, design, modelling and applications*. CRC press, 2002.

[8] Lawlor, David W. *Photosynthesis: molecular, physiological and environmental processes*. No. Ed. 2. Longman scientific & technical, 1993.

[9] Hall, David O., Frank Rosillo-Calle, Robert H. Williams, and Jeremy Woods.*Biomass for energy: supply prospects*. Earthscan, 1993.

[10] Kalogirou, Soteris A. *Solar energy engineering: processes and systems*. Academic Press, 2009.

[11] Garg, H. P. *Advances in Solar Energy Technology: Volume 1: Collection and Storage Systems*. Vol. 1. Springer, 1987.

[12] Green, Martin A. "Solar cells: operating principles, technology, and system applications." *Englewood Cliffs, NJ, Prentice-Hall, Inc., 1982. 288 p.* 1 (1982).

[13] Shah, Arvind, P. Torres, R. Tscharner, N. Wyrsch, and H. Keppner. "Photovoltaic technology: the case for thin-film solar cells." *Science* 285, no. 5428 (1999): 692-698.

[14] Bagnall, Darren M., and Matt Boreland. "Photovoltaic technologies." *Energy Policy* 36, no. 12 (2008): 4390-4396.

[15] Parida, Bhubaneswari, S. Iniyan, and Ranko Goic. "A review of solar photovoltaic technologies." *Renewable and Sustainable Energy Reviews* 15, no. 3 (2011): 1625-1636.

[16] Britt, J., and C. Ferekides. "Thin‐film CdS/CdTe solar cell with 15.8% efficiency." *Applied Physics Letters* 62 (1993): 2851.

[17] Brabec, Christoph J. "Organic photovoltaics: technology and market." *Solar energy materials and solar cells* 83, no. 2 (2004): 273-292.

[18] Brabec, Christoph, Ullrich Scherf, and Vladimir Dyakonov, eds. *Organic photovoltaics: materials, device physics, and manufacturing technologies*. Wiley. com, 2011.

[19] Crabtree, George W., Mildred S. Dresselhaus, and Michelle V. Buchanan. "The hydrogen economy." *Physics Today* 57 (2004): 39.

[20] Barreto, Leonardo, Atsutoshi Makihira, and Keywan Riahi. "The hydrogen economy in the 21st century: a sustainable development scenario."*International Journal of Hydrogen Energy* 28, no. 3 (2003): 267-284.

[21] Gregory, Derek P., D. Y. C. Ng, and G. M. Long. *The hydrogen economy*. Institute of Gas Technology, 1972.

[22] Bossel, Ph. D, Ulf, Baldur Eliasson, Ph. D, and Gordon Taylor. "The future of the hydrogen economy: Bright or bleak?." *Cogeneration and Distributed Generation Journal* 18, no. 3 (2003): 29-70.

[23] Muradov, N. Z., and T. N. Veziroğlu. "From hydrocarbon to hydrogen–carbon to hydrogen economy." *International Journal of Hydrogen Energy* 30, no. 3 (2005): 225-237.

[24] Stojić, Dragica Lj, Milica P. Marčeta, Sofija P. Sovilj, and Šćepan S. Miljanić. "Hydrogen generation from water electrolysis—possibilities of energy saving."*Journal of Power Sources* 118, no. 1 (2003): 315-319.

[25] Melis, Anastasios, and Thomas Happe. "Hydrogen production. Green algae as a source of energy." *Plant physiology* 127, no. 3 (2001): 740-748.

[26] Ross, D. K. "Hydrogen storage: the major technological barrier to the development of hydrogen fuel cell cars." *Vacuum* 80, no. 10 (2006): 1084-1089.

[27] Mehta, Viral, and Joyce Smith Cooper. "Review and analysis of PEM fuel cell design and manufacturing." *Journal of Power Sources* 114, no. 1 (2003): 32-53.

[28] Oertel, Michael, Johannes Schmitz, Walter Weirich, Ditmar Jendryssek - Neumann, and Rudolf Schulten. "Steam reforming of natural gas with intergrated hydrogen separation for hydrogen production." *Chemical engineering & technology* 10, no. 1 (1987): 248-255.

[29] Heinzel, Angelika, B. Vogel, and P. Hübner. "Reforming of natural gas—hydrogen generation for small scale stationary fuel cell systems." *Journal of Power Sources* 105, no. 2 (2002): 202-207.

[30] Rasten, Egil, Georg Hagen, and Reidar Tunold. "Electrocatalysis in water electrolysis with solid polymer electrolyte." *Electrochimica acta* 48, no. 25 (2003): 3945-3952.

[31] Choi, Pyoungho, Dmitri G. Bessarabov, and Ravindra Datta. "A simple model for solid polymer electrolyte (SPE) water electrolysis." *Solid State Ionics* 175, no. 1 (2004): 535-539.

[32] Turner, John A. "A realizable renewable energy future." *Science* 285, no. 5428 (1999): 687-689.

[33] Rajeshwar, Krishnan, Robert McConnell, and Stuart Licht, eds. *Solar hydrogen generation: toward a renewable energy future*. Springer, 2008.

[34] Turner, John, George Sverdrup, Margaret K. Mann, Pin‐Ching Maness, Ben Kroposki, Maria Ghirardi, Robert J. Evans, and Dan Blake. "Renewable hydrogen production." *International Journal of Energy Research* 32, no. 5 (2008): 379-407.

[35] Navarro, R. M., M. C. Sanchez-Sanchez, M. C. Alvarez-Galvan, F. Del Valle, and J. L. G. Fierro. "Hydrogen production from renewable sources: biomass and photocatalytic opportunities." *Energy & Environmental Science* 2, no. 1 (2009): 35-54.

Chapter 2

Solar Cells and Organic Solar Cells

2.1 Introduction

Solar cells are electrical devices that can directly convert solar energy to electricity by the photovoltaic effect. It is a more effective way of utilizing solar energy than concentrating method since it’s a one-step energy transfer process with less energy loss. Due to the significant advantages compared to fossil fuels, solar cells have been developing very fast in recent years. Figure 2-1 shows the efficiency of different types of solar cells in according to the years [1]. Under the extensive efforts, the highest efficiency for III-IV based multijunction solar cells in lab research has achieved 44.0%, 30% higher than the efficiency achieved 10 years ago, which indicates the fast technology changing in this area. However, according to the U.S. Energy Information Administration (EIA)’s report “Levelized Cost of New Generation Resources in the Annual Energy Outlook 2013”, solar energy will still be 55.3% more expensive than coal in 2017 due to the high cost of solar cell device manufacture [2]. Therefore, developing low cost solar cells with acceptable power conversion efficiency is the biggest challenge that remains to be solved.

In order to develop such solar cells, it is very important to fully understand the working mechanism of solar cells. Generally, when the sunlight is absorbed at the P-N junction of semiconductor material, the new hole-electron pair (also called as “exciton”) is formed. Under the electrical field of P-N junction, the generated hole-electron pair is separated and the hole flows to P-type area while the electron flows to N-type area [3]. At this point, if there is an external electrical circuit built up, the current is formed. This is the basic working mechanism of solar cells and is named as “photovoltaic effect” [4]. Upon this mechanism, the power conversion efficiency of solar cells relay on (1) how efficient the hole-electron pair can be generated; (2) how strong the electrical field of P-N junction can reach to separate hole-electron pair; (3) how freely hole and electron can move inside the semiconductor [5].

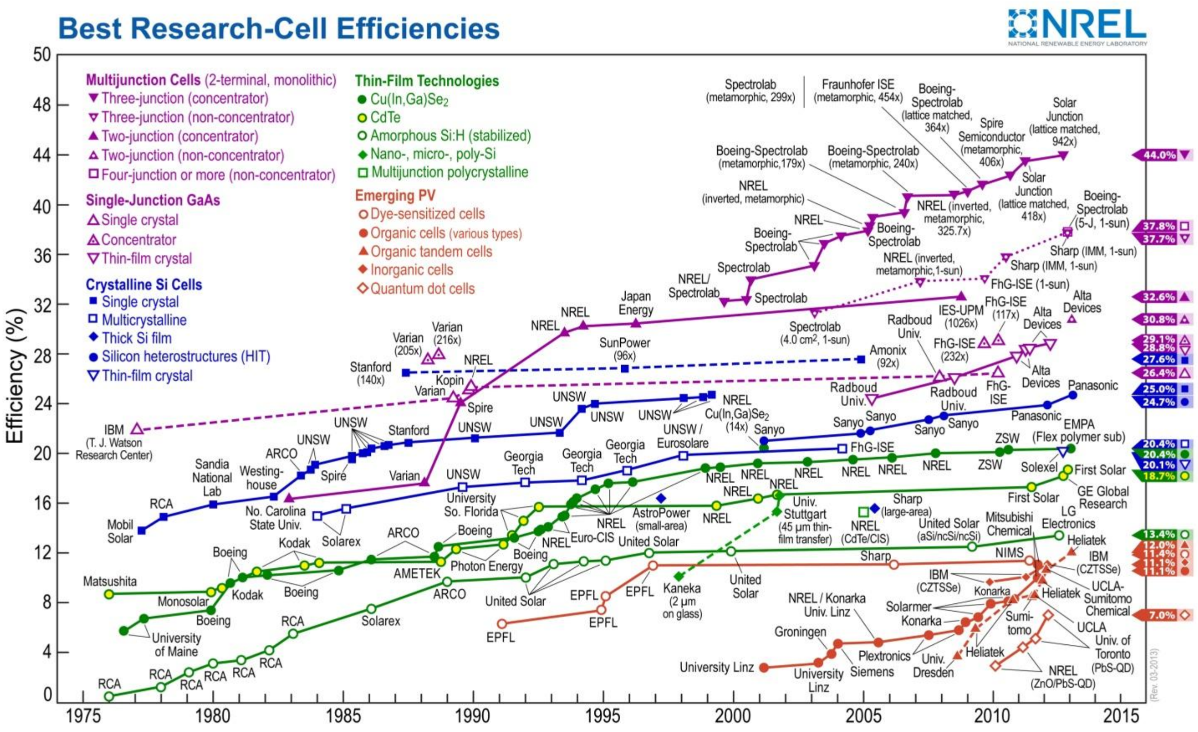

Figure 2-1 Reported timeline of solar cell energy conversion efficiencies, reproduced from National Renewable Energy Laboratory (USA)

Due to the specific applications and availability of materials, different types of solar cells have been developed. They are usually divided by the materials that are utilized to manufacture the major part of the solar cells. Silicon solar cell is the earliest type of solar cells and is the most prevalent type currently. It possesses very high power conversion efficiency and is becoming cost effective thanks to the cost reduction of silicon production [6]. Thin films solar cells, including cadmium telluride solar cell, copper indium gallium selenide solar cell, gallium arsenide multijunction solar cell, dye sensitized solar cell and organic solar cell, etc., possess good flexibility, ease of large scale processing and relatively low cost advantages [7]. The most promising application for thin films solar cells is integration of such solar cells into the parts of buildings, such as roof, windows, doors, etc.

As a newly developed type of solar cells, organic solar cell attracts great attention due to its low manufacture cost, compatibility with different substrates and possibility of tailoring molecular properties [8]. Related research covers the organic chemistry synthesis, semiconductor polymer physics, nano-science, materials characterization and engineering [9]. Its power conversion efficiency increases from 1% in 1986 to 11% in 2012 under the extensive efforts [10]. However, a lot of work still needs to be done to further enhance the performance of BHJ solar cells with less cost of manufacture.

2.2 Working mechanism of solar cells

As mentioned in introduction, photovoltaic effect is the crucial key for the function of solar cells. This effect occurs only when light is absorbed by a semiconductor material. The energy of the photons is then transferred to electrons in the valence band of the semiconductor, exciting them into the conduction band and leading to the formation of electron-hole pair [11][12]. Only photons with energy that is higher than the band-gap energy of the semiconductor can induce the excitation. Therefore, if the semiconductor possesses a smaller band gap, more incident photons can be absorbed and generate more electron-hole pairs. As a result, the current is higher while the voltage across the solar cell is lower. If the semiconductor has a larger band gap, the voltage becomes higher while the current becomes lower. It is considered that the optimal band gap for achieving highest power conversion efficiency is about 1.5 eV since most of the photons have energy between 1 eV and 3eV [13].

However, no useful electric energy takes place in an isolated semiconductor because the excited electron ends up with recombining with a hole in the valence band, emitting its excess energy as photoemission or heat. A charge separation junction, known as p-n junction is needed to extract the electricity from the excited charge carriers. A p-n junction is an interface where two types of semiconductor material, p-type and n-type in contact with each other [14]. The addition of trivalent electron acceptor impurities (usually described as "doping"), such as boron, aluminum or gallium to an intrinsic semiconductor creates p-type semiconductor with the deficiencies of valence electrons, which are called "holes" (Figure 2-2a). In p-type semiconductors, holes are the majority carriers and electrons are the minority carriers. When the intrinsic semiconductor is doped with electron donor impurities such as antimony, arsenic or phosphorous, which contribute free electrons and greatly increase the conductivity, an n-type semiconductor is formed (Figure 2-2b). In this type of semiconductors, the majority carriers are electrons and holes are the minority carriers [15].

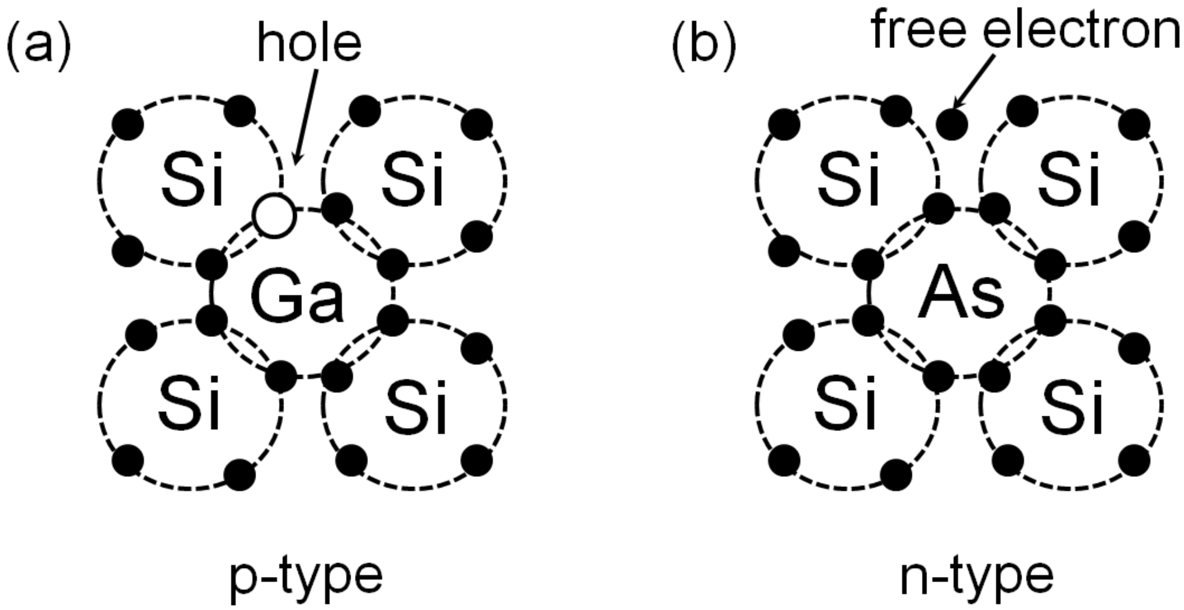

Figure 2-2 Schematic picture for (a) p-type silicon semiconductor with gallium as doping; (b) n-type silicon semiconductor with arsenic as doping

Due to the concentration gradient of charge carriers at the junction, different charge carriers diffuse across the junction between p-type and n-type region until an equilibrium is reached where the electric field is created to prevent further diffusion of charge carriers [16]. This internal electric field acts as a charge separation barrier to efficiently force electrons generated by light in p-region migrate into n-region and force holes generated in n-region migrate into p-region before the recombination of electrons and holes (Figure 2-3). In this way, the light energy is converted into electricity and can be fed into an external load.

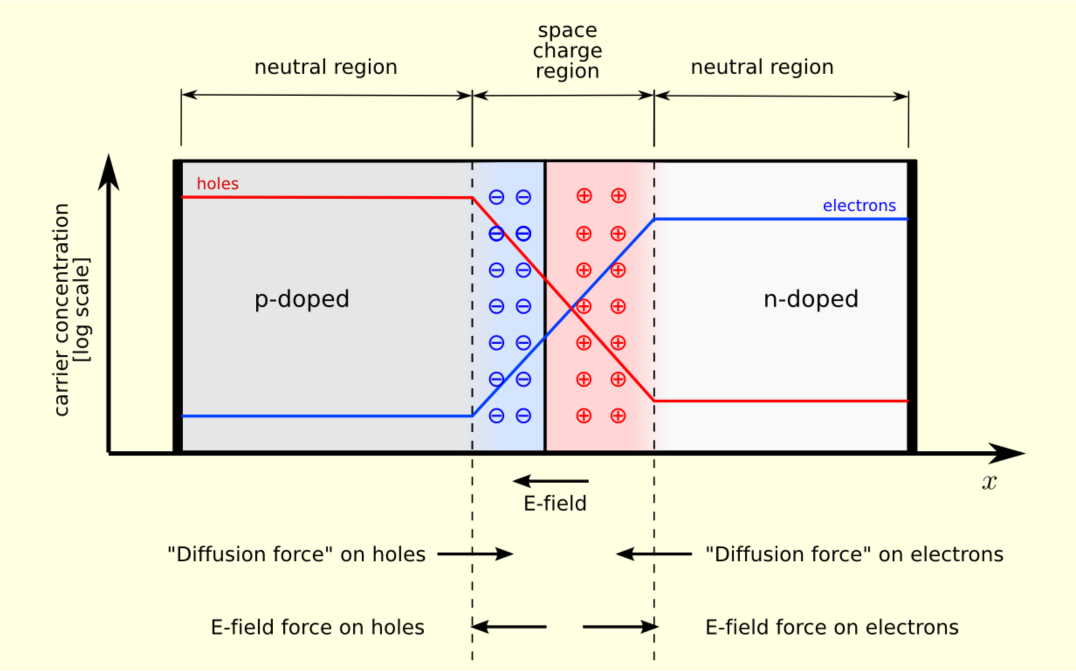

Figure 2-3 Scheme of a p–n junction in thermal equilibrium with zero-bias voltage applied. Electron and hole concentration are reported with blue and red lines, respectively. The electric field is shown on the bottom, the electrostatic force on electrons and holes and the direction in which the diffusion tends to move electrons and holes. Reproduced from en.wikipedia

The ideal I-V curve of a solar cell can be obtained by the equation below (Equation 2-1):

$$\mathbf{I = I_0\ [exp\ (qV/k_BT - 1)] - I_{sc}} \qquad (2\text{-}1)$$

where I and V are the external current and voltage; q is the electronic charge; k_B is the Boltzmann constant; I_{sc} is the short circuit current; I_0 is the reverse saturation current of the diode

[17]. When the resistance of the circuit is zero, the external current achieves the maximum value I_{sc}. When the resistance of the circuit rises, a voltage is generated across the solar cell and keeps increasing until the resistance close to infinite and the current falls to zero, where we call it open circuit voltage, V_{oc}. A typical I-V curve of a properly working solar cell based on this equation is shown in Figure 2-4. The maximum power point is the point on the curve where the square area above the curve (shown as shadow in the figure) reaches the maximum. The power conversion efficiency can then be calculated by the equation 2-2:

$$\boldsymbol{\eta = \frac{P_{max}}{P_{input}} = \frac{FF \times I_{sc} \times V_{oc}}{P_{input}}} \tag{2-2}$$

where P_{max} is the maximum power output, P_{input} is the input power, FF is the fill factor (defined as the ratio of the actual maximum power to the product of the short circuit current and open circuit voltage), $\mathbf{I_{sc}}$ is the short circuit current, V_{oc} is the open circuit voltage [18].

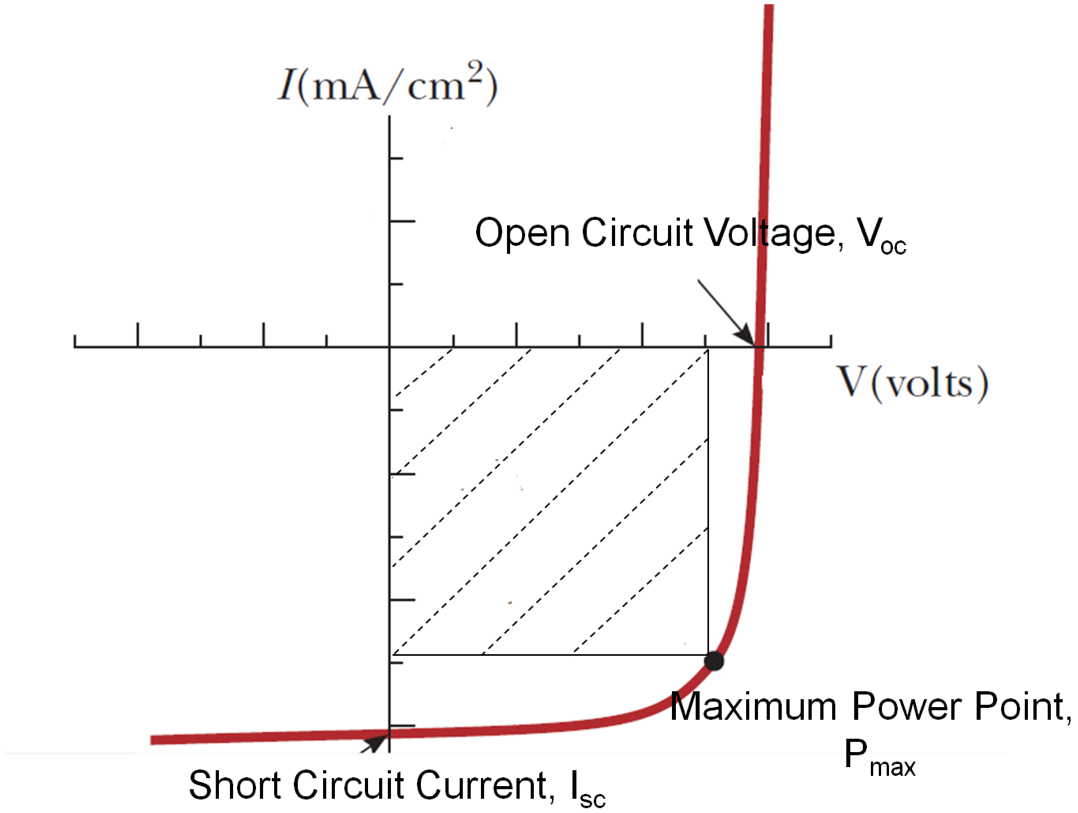

Figure 2-4 A typical I-V curve for a properly working solar cell under solar illumination

2.3 Types of solar cells

Solar cell technology has been developed for more than 100 years since the first solid state photovoltaic cell was built, and there are a lot of different types of solar cells designed within this period. This part will generally introduce the major members of this big family.

2.3.1 Silicon solar cells

Currently, the most popular material in solar cell manufacture is silicon since it has low band gap (1.11eV at 300K) [19] and is very stable. Silicon solar cells are divided into three types based on the crystallinity of the silicon material: monocrystalline, polycrystalline and amorphous silicon solar cells. Monocrystalline silicon has homogenous crystalline framework and the crystal lattice of the entire silicon is continuous with no grain boundaries, which makes the monocrystalline solar cell possess the highest power conversion efficiency (up to 24%) [21] among these three silicon solar cells. However, due to the high price of monocrystalline silicon and complicated manufacture process, the cost of monocrystalline solar cell is very high and difficult to be cut down regarding the current technology.

Polycrystalline silicon consists of a lot of small silicon crystals. To save the silicon materials and reduce the cost, thin films of polycrystalline silicon are deposited onto cheap substrate by chemical vapor deposition technologies, such as low pressure chemical vapor deposition (LPCVD) and plasma-enhanced chemical vapor deposition (PECVD) [22]. The size of the silicon crystals deposited onto the substrate has to be large in order to achieve high power conversion efficiency. With the development of processing technology, the efficiency of such solar cell can reach 19% [23].

Amorphous silicon is the non-crystalline allotropic form of silicon and can be deposited onto different substrates at low temperature. Its manufacture cost is much lower than crystalline silicon and very promising for large scale production. However, the efficiency of amorphous silicon solar cell is limited by its low absorption to long wavelength sunlight irradiation due to its 1.7eV band gap [24]. Furthermore, its efficiency decays with the increasing time under light, which is called light-induced degradation effect. To solve these problems, several thin-films of amorphous silicon are stacked on top of each other and each layer is tuned to absorb a specific frequency of light. Through this way, the efficiency of amorphous silicon solar cell rises to 13% [25], which makes it very cost effective for large scale production and application.

2.3.2 Non-silicon inorganic thin film solar cells

In order to find alternatives for silicon solar cell, many non-silicon thin film solar cells have been developed, including cadmium telluride (CdTe) solar cell, copper indium gallium selenide (CIGS) solar cell and gallium arsenide (GaAs) solar cell [26].

CdTe solar cell possesses high power conversion efficiency since its band gap (about 1.5eV) [27] is perfectly matched to the distribution of photons in the solar spectrum in terms of optimal conversion to electricity. In a typical CdTe solar cell, CdTe is usually used as p-type layer in contact with n-type cadmium sulfide (CdS) layer. After adding top and bottom contacts, a CdTe solar cell is ready for use. When CdTe solar cell is scaled-up to make large area products called modules, higher current is desired. By inserting an additional layer, which is known as transparent conductive oxide (TCO), the movement of charge carriers across the top of the cell is facilitated and thus makes it qualified for large scale application [28]. The structure of CdTe solar cell is shown in Figure 2-5. Currently, the record efficiency for a laboratory CdTe solar cell is 18.7% and the commercial CdTe modules have efficiencies between 10% and 15.8% [29]. Since the manufacture of CdTe solar cell is much lower than crystalline silicon and the efficiency of it is acceptable, CdTe solar cells become the second most abundant technology in the world marketplace after crystalline silicon, representing 6% of the 2011 world market [30]. However, since the cadmium is extremely toxic, its recycling and negative impacts on environment remain as big concerns during production, which significantly limits its further application [31].

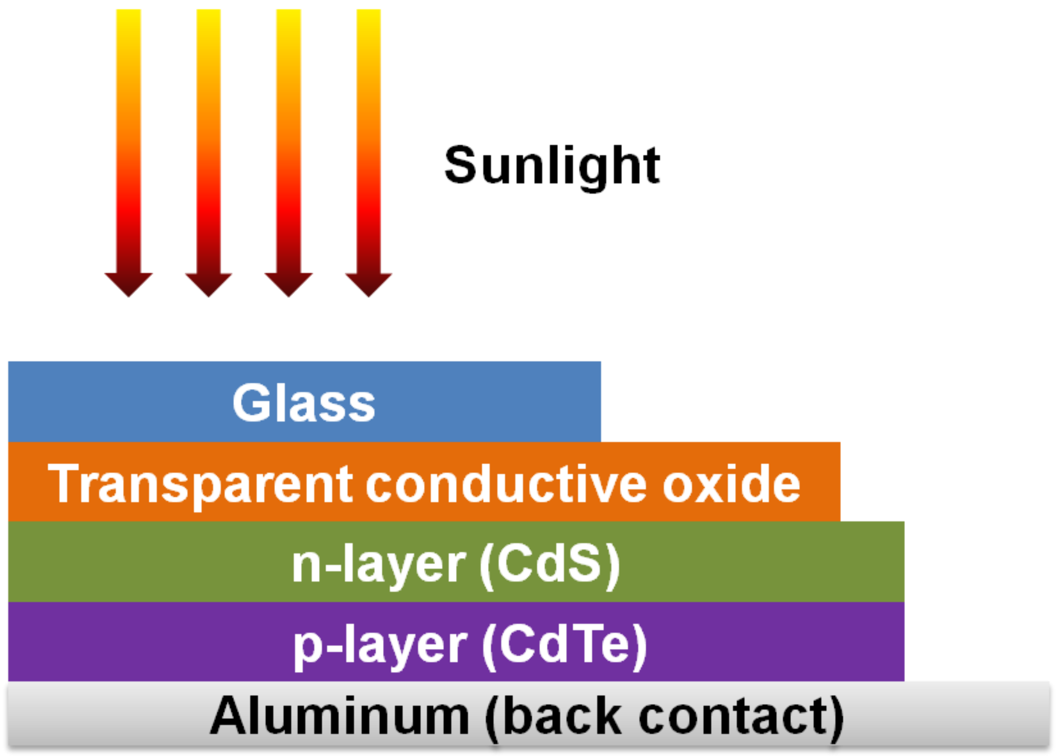

Figure 2-5 Cross-section structure of CdTe solar cell

CIGS solar cell utilizes copper indium gallium selenide (common components: $CuIn_{1-x}Ga_xSe_2$) as semiconductor material deposited on a glass or plastic substrates. Because CIGS has a high absorption coefficient (more than 10^5/cm) for photons with 1.5eV or higher energy [32], the semiconductor layer can be made very thin compared to other materials, thus saving a lot of materials and reducing the cost. CIGS films are usually deposited via co-evaporating copper, gallium and indium onto a substrate at room temperature or a heated substrate. The deposited films are then annealed with a selenide vapor to form the final CIGS layer. The record efficiency for CIGS solar cell is around 20%, which is the highest among all thin film solar cells [33].

GaAs solar cell utilizes a series of III-V compounds, including gallium, arsenide, Indium and Germanium as semiconductor thin film deposited onto the substrates. Several p-n junctions can be created with different combination between those elements and each junction is adjusted to absorb a different wavelength of light, which greatly enhances the absorption range and thus significantly increases the efficiency [34]. One example of multijunction GaAs solar cell is shown in Figure 2-6. Due to its specific multijunction structure, the absorption of sunlight almost covers the whole range and makes it to reach 30% efficiency in the lab [35][36].

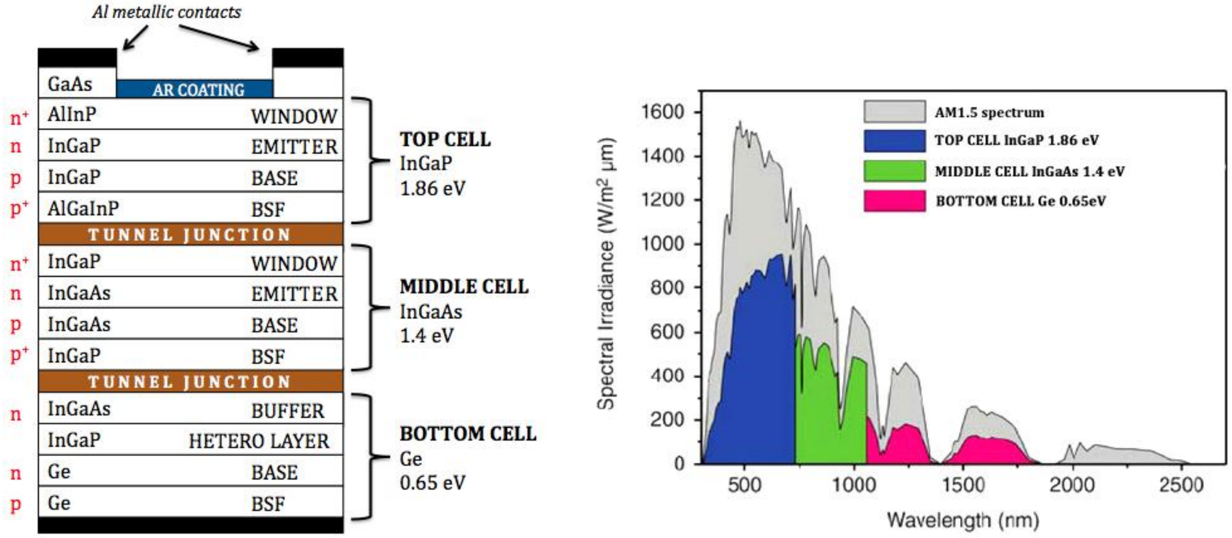

(a) (b)

Figure 2-6 (a) structure of a multijunction GaAs solar cell. There are six important types of layers: pn junctions, back surface field (BSF) layers, window layers, tunnel junctions, anti-reflective coating and metallic contacts; (b) spectral irradiance vs wavelength over the AM 1.5 spectrum and absorption range for each layer of multijunction GaAs solar cell. Reproduced from Ref [36].

2.3.3 Dye sensitized solar cell

The dye sensitized solar cell (DSSC) consists of a mechanical support coated with a transparent conducting oxide (TCO) electrode, on which dye-sensitized nanocrystalline titanium dioxide (TiO_2) are deposited to form a mesoporous network in contact with the an electrolyte containing iodide (I^-)/tri-iodide (I_3^-) redox couple between TCO and a platinum (Pt) counter electrode [37]. When sunlight is absorbed by dye molecules adsorbed on the TiO_2, the excited dye molecules inject electrons into the conduction band of the TiO_2. The injected electrons then flow towards the transparent electrode where they are collected for powering a load and are reintroduced into the cell via the counter electrode on the back, flowing into the electrolyte. The dye molecules recover to neutral state by grabbing electrons from I^-, which is then oxidized to I_3^-. I^- is then reproduced by the reduction of I_3^- with electrons re-enter the cell from counter electrode [38].

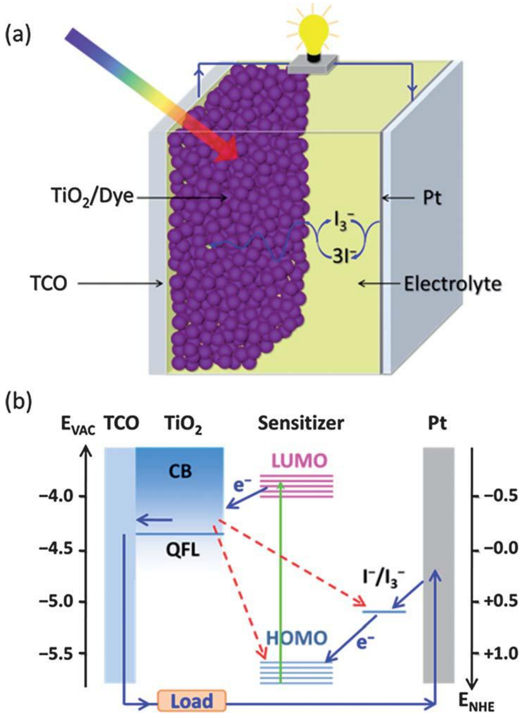

Figure 2-7 (a) Schematic structure and (b) main processes in dye-sensitized solar cells. Reproduced from Ref [37].

DSSC attracts great interests due to its low manufacture cost, ease of processing and long stability. Its efficiency is usually above 10% and the cost is only 1/5-1/10 of silicon solar cells [39]. However, the research in this area is relatively new and more work has to be done to scale up the production and replace the Pt counter electrode with cheaper alternatives without significantly sacrificing efficiency.

2.3.4 Organic solar cell

An organic solar cell is a type of solar cell that utilizes conductive organic polymers or small organic molecules for sunlight harvest and charge transportation to produce electricity by the photovoltaic effect. The materials that used for organic photovoltaics commonly possess large conjugated systems. Their molecular structure consistently presents a backbone along which the carbon atoms are sp^2-hybridized (carbon atoms covalently bond with alternating single and double bonds) and thus form a delocalized bonding π orbital with a π^* antibonding orbital. The delocalized π orbital represents the highest occupied molecular orbital (HOMO), while the π^* orbital represents the lowest unoccupied molecular orbital (LUMO). The difference of energy level between HOMO and LUMO is the band gap of organic electronic materials, which is usually in the range of 1-4 eV [40][41][42].

The organic solar cell consists of a transparent electrode, typically a conducting oxide such as indium-tin oxide (ITO), organic light-absorbing layer, and a second electrode (i.e. Al, Mg, Ca). The organic layer usually contains two different organic semiconductors, one is used as electron-donor (D) and the other is used as electron-acceptor (A). Electron-donor semiconductor material exhibits a high-lying HOMO energy, while electron-acceptor material possesses a low-lying LUMO energy. The process of photocurrent is shown in Figure 2-8. Here the electron-donor material is poly (3-hexylthiophene-2,5-diyl) (P3HT) and the electron-acceptor is [6,6]-Phenyl C_{61} butyric acid methyl ester (PCBM). When the organic layer absorbs photon from sunlight, the electron-hole pair (exciton) is formed and diffuses towards the donor-acceptor interface, where the electron-hole pair separates into free charge carriers: electron and hole. These carriers then transport towards different electrodes for collection. The two semiconductor materials have differences in HOMO and LUMO, which set up electrostatic forces at the interface. When chosen properly, the differences can generate stronger electric fields that may break up the electron-hole pair more efficiently. The difference of energy level between HOMO of electron donor and LUMO of electron acceptor is defined as open circuit voltage (V_{oc}) for organic solar cell.

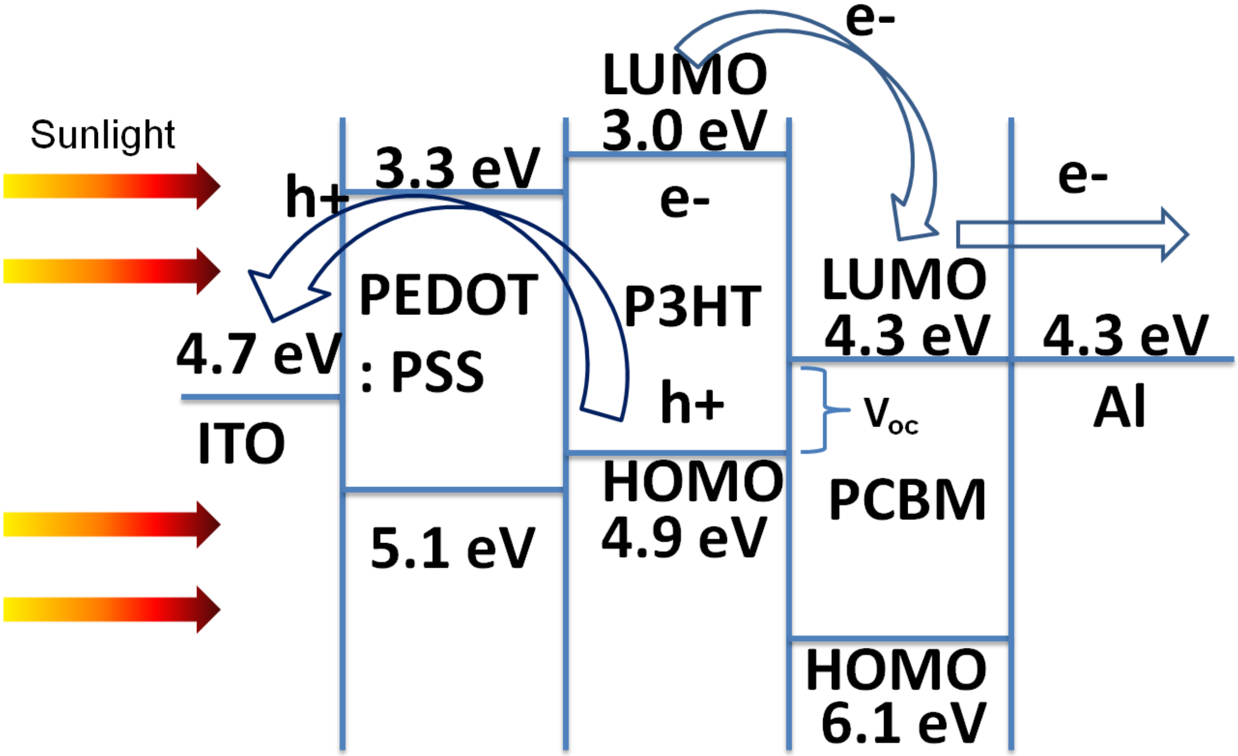

Figure 2-8 Schematic of process of photocurrent generation in organic solar cell with energy level diagram for each component.

The key advantages of organic solar cell are identified as:

(1) Flexibility and light weight of the PV modules;

(2) Convenient integration into other products, e.g. windows, backpack, military uniform;

(3) Significantly lower manufacture costs compared to conventional inorganic technologies

(4) Ease of processing by using state of the art printing tools

(5) Short energy payback times and low environmental impact during manufacture and operations [43]

In organic semiconductors, the interaction between organic molecules is much weaker compared to silicon semiconductors. It is difficult to form continuous conduction and valence band in the bulk via combination of HOMO and LUMO of different molecules. The transportation of charge carriers relies on charges' hopping from molecule to molecule. As a result, the charge carrier mobility strongly depend on the morphology and can vary over several orders of magnitude when going from highly disordered amorphous films (typically, 10^{-6} to 10^{-3} $cm^2\ V^{-1}\ s^{-1}$) to highly ordered crystalline materials (>1 $cm^2\ V^{-1}\ s^{-1}$) [41]. Moreover, the dissociation of exciton is crucial to the efficiency of the organic solar cell. As mentioned above, the generated excitons must diffuse to the interface of electron donor and electron acceptor to realize separation of electron and hole. The diffusion length for excition is usually around 10 nm [44]. Therefore, if the generated exciton is too far away from the interface, electron and hole will recombine and release the energy it absorbs, which has no contribution to the photocurrent.

2.4 Development of organic solar cell

The first generation of organic solar cell is single layer organic solar cell. Only one organic electronic layer is placed between two electrodes with different work function, typically a layer of indium tin oxide (ITO) with high work function and a layer of low work function metal (i.e. Al, Mg, Ca). The difference of work function between two electrodes constitutes an electric filed and forces the separation of hole and electron when the organic layer absorbs light and form excitons. However, the electric field formed by two electrodes cannot efficiently break up excitons and thus the efficiency of this type of organic solar cell is very low (<0.1%) [45].

The second generation of organic solar cell is bilayer organic solar cell. This type of organic solar is first reported by Deng in 1986. By introducing two layers of organic semiconductors, one is electron-donor (regarded as p-type) and the other one is electron-acceptor (regarded as n-type), the efficiency of the solar cell is significantly enhanced. Due to the differences in HOMO and LUMO energy level between two organic semiconductors, the electrostatic forces are generated at the interface between two layers. If chosen properly, the electrostatic force will be strong enough to break up the excitions more efficiently than the single layer organic solar cell, leading to more than 1% efficiency [45]. This discovery is a breakthrough in the history of organic solar cell's development. All types of organic solar cells that designed afterwards are based on this idea. The problem with this type of solar cell is: only the excitons that are generated near the interface between two layers can be efficiency separated since the thickness of organic solar cell is usually around 100 nm, which is much higher than the diffusion length of excitons (10nm). A large fraction of excitons recombine before they arrive the interface and therefore is difficult to achieve high efficiency.

In order to conquer the problems addressed above, bulk heterojunction organic solar cell is developed by the researchers. In this type of organic solar cell, the electron donor and acceptor are mixed together to form a polymer blend (Figure 2-9), which is inserted between two electrodes. A layer of hole conductive material is usually placed under the polymer blend thin film for better hole conductivity. Much larger interface area between electron donor and acceptor is created due to the interpenetrating network inside the polymer blend, and thus significantly increase the dissociation efficiency of excitons, leading to higher power conversion efficiency than the previous two types of organic solar cells. However, due to the disorder structure inside the active layer, considerable fraction of donor and acceptor are isolated or far away from electrodes. This nanomorphology may lead to the trap of charge carriers within the separated materials or a long conduction path which causes possible recombination of the electron and hole, unavoidably affecting the efficiency of the cell. Therefore, the internal morphology control is the key to enhance the efficiency of bulk heterojunction organic solar cell [46].

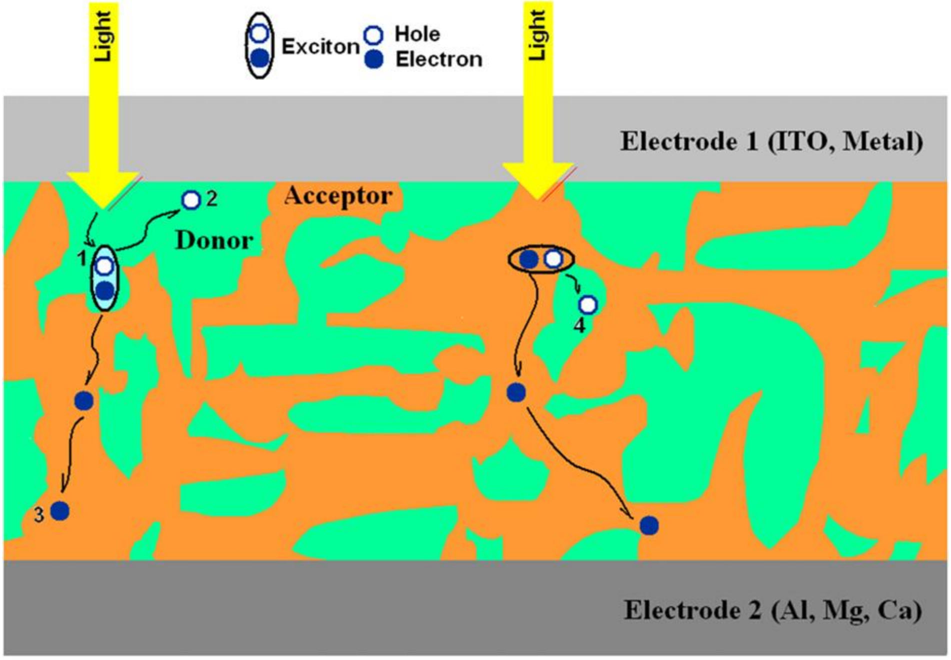

Figure 2-9 The structure of a bulk heterojunction organic solar cell. As depicted in the diagram, (1) exciton created by incident light diffusing towards a D–A interface; (2) hole drifting towards electrode; (3) electron moving towards electrode; (4) hole trapped in an isolated island of organic molecule. Charge carriers can sometimes be trapped within the randomly separated materials and fail to reach the electrodes. Reproduced from Ref [46]

2.5 Recent research on morphology control for BHJ solar cell

As mentioned in 2.3.4 and 2.4, morphology control of BHJ solar cell is quite important for the efficiency of the BHJ solar cell. Earlier studies have attempted to optimize the morphology of the active layer in BHJ solar cell by thermal annealing, components ratio adjustment and solvent effect.

Thermal annealing of as-cast organic thin film can make the surface of the film become rougher. Yang Yang's research indicates that higher roughness of the film surface will give higher efficiency device due to the increased contact area between the polymer film and the metal cathode, which may result in a more efficient charge collection at the interface [47]. The increased surface roughness may also enhance internal reflection and improve light harvest to increase the device efficiency. In fact, the increased interface area is quite limited due to the change of roughness. It is also argued that thermal annealing may increase the light absorption and carrier mobility because of the ordered structure and enhanced crystallinity after annealing.

Component ratio adjustment between electron donor material and acceptor material has direct impact on the domain size of separated phase. If the electron donor and acceptor are not perfectly miscible, phase separation occurs in the thin film that is spun cast on the substrate after thermal annealing. There are electron donor-rich phase and electron acceptor-rich phase inside the thin film. Since the diffusion length of exciton is around 10nm, the domain size of phase separation should not be bigger than this value. Otherwise, certain fraction of excitons will recombine and cannot contribute to the photocurrent [48].

Since organic electronic materials possess different solubility in different solvents, the crystallinity of these materials in the as cast thin film may depend on the solvent chosen to dissolve them. The higher crystallinity can lead to faster carrier mobility and thus increase the efficiency of the solar cell.

Although three methods mentioned above are easy to operate, they can only create minor change to the morphology of the BHJ solar cell and the resulted enhancement of the efficiency is quite limited. The ideal morphology for BHJ solar cell is shown in Figure 2-10. Donor and acceptor materials are phase separated with highly ordered column structure and interpenetrate network is required to achieve large interface area. The distance between two columns is twice of diffusion length of exciton, around 20nm [49], to make sure the generated excitons can efficiently diffuse into the interface between donor and acceptor. Besides, all donor material are interconnected and have direct contact to the ITO electrode, which is the hole collector, while all acceptor material should have interconnection and direct contact to the Al electrode, which is the electron collector. This ideal structure is estimated to possess 1.5 times higher quantum efficiency than the disordered morphology [50].

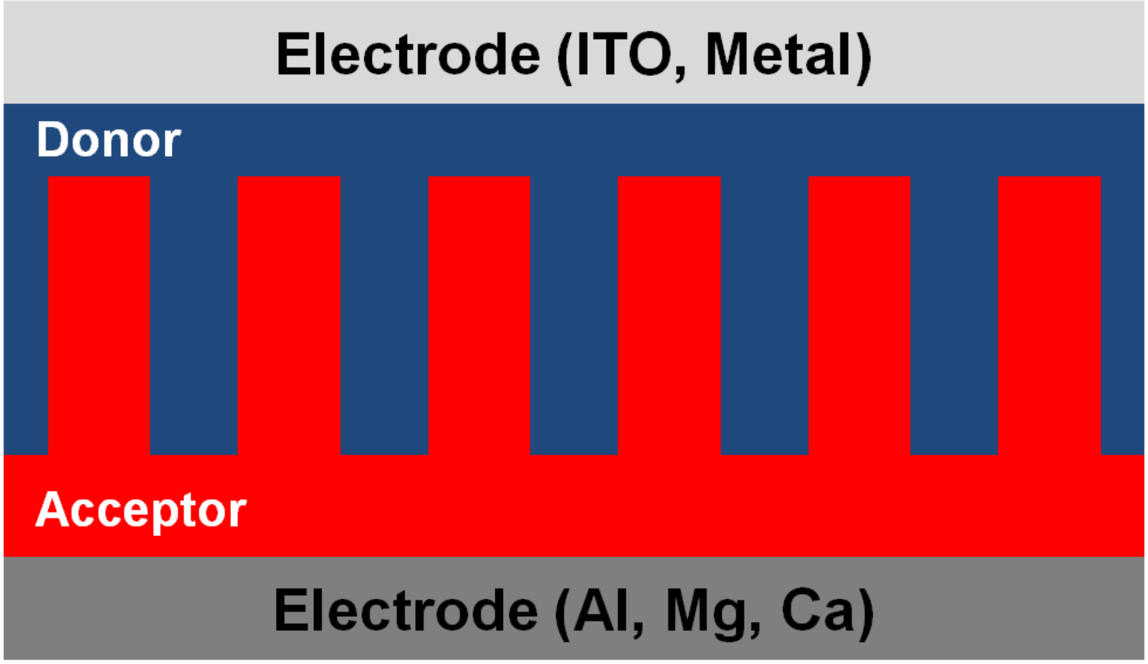

Figure 2-10 Ideal morphology for bulk heterojunction organic solar cell

In order to achieve this structure, researchers are trying to build up the structure similar to the ideal morphology. McGehee et al. first reported that the hole mobility in regioregular P3HT can be enhanced by a factor of 20 by infiltrating it into straight nanopores (20 nm in diameter) of anodic alumina [51]. However, when the pore size shrinks to 10 nm, the hole mobility of P3HT decreases which may because of the cut of polymer chain at this small scale. C.T. Black later demonstrated that his group successfully confined blended P3HT and PCBM within nanometer-scale cylindrical pores via the alumina template [52]. It is found that the supported short-circuit photocurrent density was nearly doubled compared to equivalent unconfined volumes of the same blend and increases the P3HT hole mobility in the blend by around 500 times. Since the alumina is insulator, the current density is only 80% of the short circuit current density of unconfined P3HT/PCBM device. Black's group then replace alumina wall with TiO_2, a semiconductor, as radial contacts in order to improve the electron mobility of such construction [53]. In this way, the short circuit current reaches 14.6 mA/cm^2, generating almost 80% of the maximum possible photocurrent for a 1.85eV band-gap light absorber and thus increasing the efficiency of the device by 70% compared to the confined device without TiO_2 contacts.

The template method is a very promising way to achieve the ideal morphology inside the active layer of BHJ solar cell. However, direct contact for electron acceptor with electrode cannot be created via this way. Moreover, the use of template significantly increases the cost of the solar cell manufacture and it may be not suitable for the scale-up production.

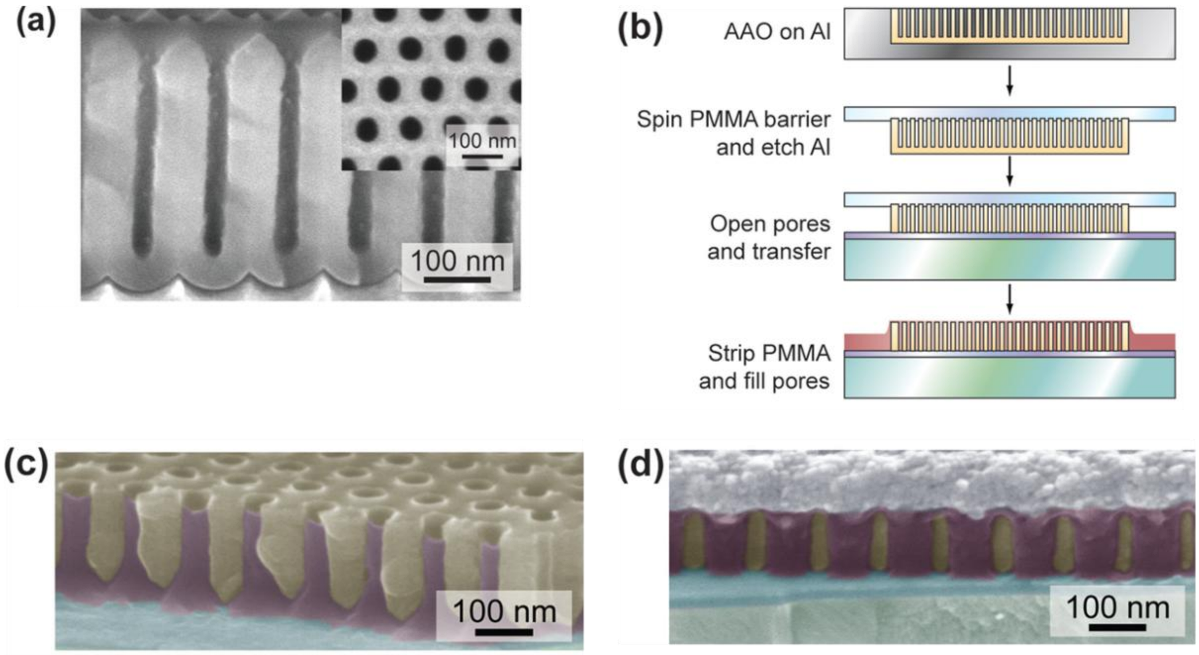

Figure 2-11 (Color) Fabrication of templated bulk heterojunction solar cells. (a) Cross sectional view of a 300nm tall nanoporous alumina template. Inset: top view. (b) Schematic template transfer procedure. (c) SEM image of nanoporous alumina template (beige) filled with an organic semiconductor (purple) on V2O5 (blue)/ITO (green). (d) SEM image of completed template bulk heterojunction solar cell. Reproduced from Ref [52].

References

[1] Kazmerski, Lawrence L. "Photovoltaics: A review of cell and module technologies." *Renewable and sustainable energy reviews* 1, no. 1 (1997): 71-170.

[2] U.S. Energy Information Administration (EIA)'s report "*Levelized Cost of New Generation Resources in the Annual Energy Outlook 2013*", 2013.

[3] Paez, D. J., E. Huante-Ceron, and A. P. Knights. "A Vertical PN Junction Utilizing the Impurity Photovoltaic Effect for the Enhancement of Ultra-thin Film Silicon Solar Cells." In *MRS Proceedings*, vol. 1536, pp. mrss13-1536. Cambridge University Press, 2013.

[4] Lee, Young In, Mina Kim, Yoon Ho Huh, J. S. Lim, Sung Cheol Yoon, and Byoungchoo Park. "Improved photovoltaic effect of polymer solar cells with nanoscale interfacial layers." *Solar Energy Materials and Solar Cells* 94, no. 6 (2010): 1152-1156.

[5] Green, Martin A. "Solar cells: operating principles, technology, and system applications." *Englewood Cliffs, NJ, Prentice-Hall, Inc., 1982. 288 p.* 1 (1982).

[6] Wenham, S. R., and M. A. Green. "Silicon solar cells." *Progress in Photovoltaics: Research and Applications* 4, no. 1 (1996): 3-33.

[7] Chopra, Kasturi L., and Suhit Ranjan Das. *Thin film solar cells*. Springer, 1983.

[8] Wöhrle, Dieter, and Dieter Meissner. "Organic solar cells." *Advanced Materials*3, no. 3 (1991): 129-138.

[9] Günes, Serap, Helmut Neugebauer, and Niyazi Serdar Sariciftci. "Conjugated polymer-based organic solar cells." *Chemical reviews* 107, no. 4 (2007): 1324-1338.

[10] GŁOWACKI, ERIC DANIEL, NIYAZI SERDAR SARICIFTCI, and CHING W. TANG. "Organic Solar Cells." (2013).

[11] Goetzberger, Adolf, Joachim Knobloch, and Bernhard Voss. *Crystalline silicon solar cells*. Chichester: Wiley, 1998.

[12] Fahrenbruch, A., and Richard H. Bube. "Fundamentals of solar cells." (1983).

[13] Rothwarf, A. L. L. E. N., JOHN D. Meakin, and ALLEN M. Barnett. "Thin-film photovoltaic devices." *Polycrystalline and Amorphous Thin Films and Devices, Academic Press, New York* (1980): 229-255.

[14] Kazmerski, Lawrence, ed. *Polycrystalline and amorphous thin films and devices*. Academic Press, 1980.

[15] Nelson, Jenny, and Mark Ratner. "The physics of solar cells." *Physics Today*57, no. 12 (2004): 71-71.

[16] Neville, Richard C. "Solar energy conversion: The solar cell." In *Amsterdam, Elsevier Scientific Publishing Co.(Studies in Electrical and Electronic Engineering. Volume 1), 1978. 307 p.*, vol. 1. 1978.

[17] Fonash, Stephen. *Solar cell device physics*. Access Online via Elsevier, 1981.

[18] Hoppe, Harald, and Niyazi Serdar Sariciftci. "Organic solar cells: An overview."*Journal of Materials Research* 19, no. 07 (2004): 1924-1945.

[19] Wenham, Stuart. "Buried‐contact silicon solar cells." *Progress in photovoltaics: research and applications* 1, no. 1 (1993): 3-10.

[20] Green, Martin A., Stuart R. Wenham, and Jianhua Zhao. "Progress in high efficiency silicon cell and module research." In *Photovoltaic Specialists Conference, 1993., Conference Record of the Twenty Third IEEE*, pp. 8-13. IEEE, 1993.

[21] Zhao, Jianhua, Aihua Wang, Martin A. Green, and Francesca Ferrazza. "19.8% efficient “honeycomb” textured multicrystalline and 24.4% monocrystalline silicon solar cells." *Applied Physics Letters* 73 (1998): 1991.

[22] Gall, S., C. Becker, E. Conrad, P. Dogan, F. Fenske, B. Gorka, K. Y. Lee, B. Rau, F. Ruske, and B. Rech. "Polycrystalline silicon thin-film solar cells on glass." *Solar Energy Materials and Solar Cells* 93, no. 6 (2009): 1004-1008.

[23] Braga, A. F. B., S. P. Moreira, P. R. Zampieri, J. M. G. Bacchin, and P. R. Mei. "New processes for the production of solar-grade polycrystalline silicon: A review." *Solar energy materials and solar cells* 92, no. 4 (2008): 418-424.

[24] De Wild, J., A. Meijerink, J. K. Rath, W. G. J. H. M. Van Sark, and R. E. I. Schropp. "Towards upconversion for amorphous silicon solar cells." *Solar Energy Materials and Solar Cells* 94, no. 11 (2010): 1919-1922.

[25] Green, Martin A., Keith Emery, Yoshihiro Hishikawa, Wilhelm Warta, and Ewan D. Dunlop. "Solar cell efficiency tables (version 39)." *Progress in photovoltaics: research and applications* 20, no. 1 (2011): 12-20.

[26] Aberle, Armin G. "Thin-film solar cells." *Thin Solid Films* 517, no. 17 (2009): 4706-4710.

[27] McEvoy, Augustin Joseph, Luis Castañer, and Tomas Markvart, eds. *Solar Cells: Materials, Manufacture and Operation*. Academic Press, 2012.

[28] Swanson, Drew E., Russell M. Geisthardt, J. Tyler McGoffin, John D. Williams, and James R. Sites. "Improved CdTe Solar-Cell Performance by Plasma Cleaning the TCO Layer." *Photovoltaics, IEEE Journal of* 3, no. 2 (2013): 838-842.

[29] Britt, J., and C. Ferekides. "Thin-film CdS/CdTe solar cell with 15.8% efficiency." *Applied Physics Letters* 62 (1993): 2851.

[30] Fthenakis, Vasilis. "Sustainability of photovoltaics: The case for thin-film solar cells." *Renewable and Sustainable Energy Reviews* 13, no. 9 (2009): 2746-2750.

[31] Miles, R. W., K. M. Hynes, and I. Forbes. "Photovoltaic solar cells: An overview of state-of-the-art cell development and environmental issues."*Progress in Crystal Growth and Characterization of Materials* 51, no. 1 (2005): 1-42.

[32] Poortmans, Jef, and Vladimir Arkhipov, eds. *Thin film solar cells: fabrication, characterization and applications*. Vol. 5. John Wiley & Sons, 2006.

[33] Repins, Ingrid, Miguel A. Contreras, Brian Egaas, Clay DeHart, John Scharf, Craig L. Perkins, Bobby To, and Rommel Noufi. "19.9% efficient ZnO/CdS/CuInGaSe2 solar cell with 81.2% fill factor." *Progress in Photovoltaics: Research and applications* 16, no. 3 (2008): 235-239.

[34] King, R. R., D. C. Law, K. M. Edmondson, C. M. Fetzer, G. S. Kinsey, H. Yoon, R. A. Sherif, and N. H. Karam. "40% efficient metamorphic GaInP⁄ GaInAs⁄ Ge multijunction solar cells." *Applied physics letters* 90 (2007): 183516.

[35] Bertness, K. A., Sarah R. Kurtz, D. J. Friedman, A. E. Kibbler, C. Kramer, and J. M. Olson. "29.5% ‐ efficient GaInP/GaAs tandem solar cells." *Applied physics letters* 65, no. 8 (1994): 989-991.

[36] Román, José María. "State-of-the-art of III-V Solar Cell Fabrication Technologies, Device Designs and Applications." *Advanced Photovoltaic Cell Design* (2004).

[37] Zhang, Shufang, Xudong Yang, Youhei Numata, and Liyuan Han. "Highly efficient dye-sensitized solar cells: progress and future challenges." *Energy Environ. Sci.* 6, no. 5 (2013): 1443-1464.

[38] Grätzel, Michael. "Dye-sensitized solar cells." *Journal of Photochemistry and Photobiology C: Photochemistry Reviews* 4, no. 2 (2003): 145-153.

[39] Kroon, J. M., N. J. Bakker, H. J. P. Smit, P. Liska, K. R. Thampi, P. Wang, S. M. Zakeeruddin et al. "Nanocrystalline dye‐sensitized solar cells having maximum performance." *Progress in Photovoltaics: Research and Applications* 15, no. 1 (2007): 1-18.

[40] Hoppe, Harald, and Niyazi Serdar Sariciftci. "Organic solar cells: An overview." *Journal of Materials Research* 19, no. 07 (2004): 1924-1945.

[41] Kippelen, Bernard, and Jean-Luc Brédas. "Organic photovoltaics." *Energy & Environmental Science* 2, no. 3 (2009): 251-261.

[42] Sun, Sam-Shajing, and Niyazi Serdar Sariciftci, eds. *Organic photovoltaics: mechanisms, materials, and devices*. CRC press, 2010.

[43] Dennler, Gilles, Markus C. Scharber, and Christoph J. Brabec. "Polymer‐Fullerene Bulk‐Heterojunction Solar Cells." *Advanced Materials* 21, no. 13 (2009): 1323-1338.

[44] Markov, Denis E., Emiel Amsterdam, Paul WM Blom, Alexander B. Sieval, and Jan C. Hummelen. "Accurate measurement of the exciton diffusion length in a conjugated polymer using a heterostructure with a side-chain cross-linked fullerene layer." *The Journal of Physical Chemistry A* 109, no. 24 (2005): 5266-5274.

[45] Tang, Ching W. "Two-layer organic photovoltaic cell." *Applied Physics Letters* 48 (1986): 183.

[46] Yeh, Naichia, and Pulin Yeh. "Organic solar cells: Their developments and potentials." *Renewable and Sustainable Energy Reviews* 21 (2013): 421-431.

[47] Li, Gang, Vishal Shrotriya, Yan Yao, and Yang Yang. "Investigation of annealing effects and film thickness dependence of polymer solar cells based on poly (3-hexylthiophene)." *Journal of Applied Physics* 98, no. 4 (2005): 043704-043704.

[48] Li, Gang, Rui Zhu, and Yang Yang. "Polymer solar cells." *Nature Photonics* 6, no. 3 (2012): 153-161.

[49] Moule, Adam J., and Klaus Meerholz. "Morphology Control in Solution‐Processed Bulk‐Heterojunction Solar Cell Mixtures." *Advanced Functional Materials* 19, no. 19 (2009): 3028-3036.

[50] Liang, Yongye, Zheng Xu, Jiangbin Xia, Szu‐Ting Tsai, Yue Wu, Gang Li, Claire Ray, and Luping Yu. "For the bright future—bulk heterojunction polymer solar cells with power conversion efficiency of 7.4%." *Advanced Materials* 22, no. 20 (2010): E135-E138.

[51] Coakley, Kevin M., Bhavani S. Srinivasan, Jonathan M. Ziebarth, Chiatzun Goh, Yuxiang Liu, and Michael D. McGehee. "Enhanced hole mobility in regioregular polythiophene infiltrated in straight nanopores." *Advanced Functional Materials* 15, no. 12 (2005): 1927-1932.

[52] Allen, Jonathan E., Kevin G. Yager, Htay Hlaing, Chang-Yong Nam, Benjamin M. Ocko, and Charles T. Black. "Enhanced charge collection in confined bulk heterojunction organic solar cells." *Applied Physics Letters* 99 (2011): 163301.

[53] Allen, Jonathan E., and Charles T. Black. "Improved power conversion efficiency in bulk heterojunction organic solar cells with radial electron contacts." *ACS nano* 5, no. 10 (2011): 7986-7991.

Chapter 3

Self Assembly Columnar Structure via Phase Separation in Polymer Blends

3.1 Introduction

As discussed in Chapter 2, there is an ideal morphology for BHJ organic solar cell to achieve excellent charge carrier transportation and high power conversion efficiency. However, the current methods for morphology control either create only minor changes to the morphology or need intensive efforts. Finding a simpler way that can significantly modify the morphology to ideal condition in the active layer of BHJ organic solar cell remains a challenge for the researchers.

Considering the active layer of BHJ solar cell is a system consists of polymer (P3HT) and nanoparticle (PCBM), which is also known as “nanocomposites” , it is important to understand the specific properties of nanocomposites. The key to discussion of nanoparticle-polymer composites is a consideration of enthalpic and entropic interactions when functionalized nanoparticles are introduced into the polymer system [1]. Recent investigations of nanoparticles in immiscible mixtures show that nanoparticles can be used to stabilize evolving morphologies and/or arrest domain coarsening [2]. More specifically, the nanoparticles formed a monolayer around the interface between two immiscible components. Rafailovich and co-workers observed a significant reduction in the domain size in phase separated binary blends using clays modified with organic ligands as a result of the localization of the clay sheets at the interface between the immiscible components [3]. Nanoparticles have also been shown to have effects on the phase-separation kinetics in polymer mixtures. Tanaka *et al.*showed that nanoparticles are able to significantly change the coarsening dynamics of mixtures [4]. Theoretical studies of nanoparticle-filled mixtures indicate the existence of different pattern formation at early stages of phase separation and a subsequent slowing of domain growth afterwards [5] [6]. Further studies have shown that when nanoparticles are present in an immiscible polymer blend, they preferentially segregate to the interfaces, allowing the interface to produce a template for the particle segregation [7]. Therefore it is postulated that if one or both of the phases were photoactive polymers, then if carrier particles were added, a structure for heterojunction solar cells could be formed where a direct pathway to the electrodes could be templated for the carrier particles (Figure 3-1).

The advantages of this structure are:

(1) Interface area between electron donor (P3HT) and electron acceptor (PCBM) is much larger than that of the conventional BHJ solar cell and ensure the high efficiency of excitons dissociation;

(2) Continuous phase of P3HT promises the efficient transportation of holes and the direct contact to the ITO electrode ensure the hole collection;

(3) Segregation of PCBM along the interface promises the efficient transportation of electrons and the connection to the Al contact is good for electron collection

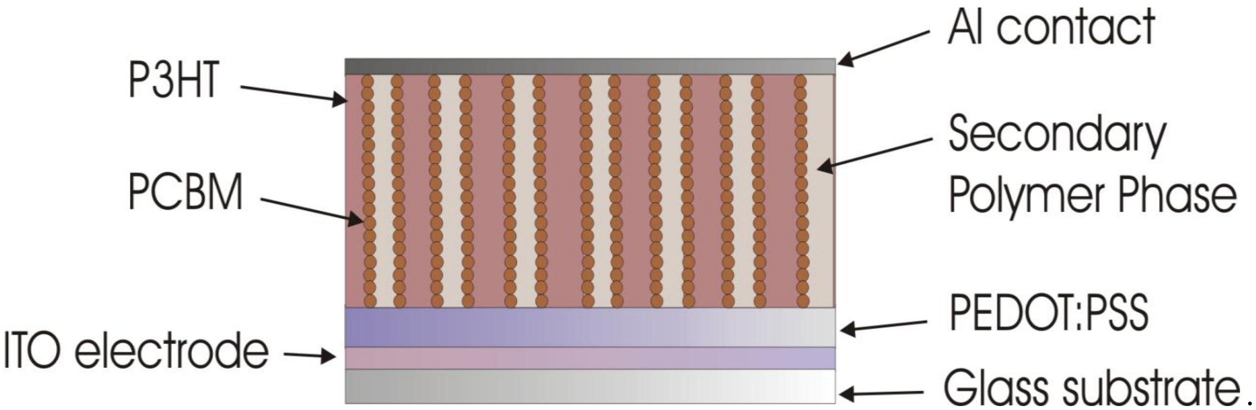

Figure 3-1 Proposed morphology of active layer by introducing a secondary polymer into the nanocomposites to build up columns of P3HT while the PCBM nanoparticles segregate at the interface between two immiscible polymers. Pink columns represent P3HT, white columns represent secondary polymer phase and red spheres represent PCBM.

3.2 Molecular dynamics (MD) simulation

To test our hypothesis, that the introduction of an additional polymer would create the morphology that we desire, we initiated a series of MD simulations. MD simulation is a computer based simulation of physical movements of atoms and molecules in the context of N-body simulation. Considering the interaction between atoms and molecules, the motion of the atoms/molecules is given based on the theoretical physical principle. In most cases, the movement of atoms and molecules are determined by numerically solving the Newton's equations of motion for a system of interacting particles, where forces between the particles and potential energy are defined by molecular mechanics force fields.

In our simulations, the two polymers, and the nanoparticle were confined to a thin film bounded by two hard surfaces. Our systems consist of linear polymer chains, with $N = 32$ segments, which corresponds to chains below the entanglement length found in literature [8]. We use the Kremer and Grest model [9] for polymers where the monomers of the polymer chain interact through a Lennard-Jones potential $V(\mathrm{r})$, of the form:

$$V(\mathrm{r}) = 4\varepsilon[(\sigma/\mathrm{r})^{12} - \delta(\sigma/\mathrm{r})^{6}] \tag{3-1}$$

where σ and ε are the Lennard-Jones parameters and the separating distance r, is governed by $\mathrm{r} < \mathrm{r}^{c} = 2.5\sigma$. The potential is zero for $\mathrm{r} > \mathrm{r}^{c}$. δ is a parameter that is used to control the incompatibility of the two polymers, when $\delta < 1$ the repulsive term in the LJ potential dominates and the two polymers will phase separate [10]. In the rest of this paper, will we use σ, ε and $\tau = (\mathrm{m}\sigma^{2}/\varepsilon)^{1/2}$ in order to set length, energy, and time scales, respectively (where m is the mass of an atom). Adjacent monomers along the chain are coupled by an additional FENE potential which prevents chain breaking and yields realistic dynamics for the polymer [9]. The FENE (Finite Extendable Non-linear Elastically) takes on the form:

$$V_{CH}(r) = -0.5KR_0^2 \ln(1-(r/R_0)^2) \tag{3-2}$$

where $K = 30\varepsilon$ and $R_0 = 1.5\sigma$ [11][12]. A modified form of the Lennard-Jones potential was used to model the nano-filler particles [13][14]:

$$V(r) = 4\varepsilon_{fp}[(\sigma/(r-s))^{12} - \delta(\sigma/(r-s))^6] \tag{3-3}$$

where s controls the size of the nano-filler; $s = (\sigma_f - \sigma)/2$, σ_f and σ are the size of the nano-filler and polymer, respectively, and ε_{fp} is the interaction energy between the polymer and the nano-fillers. Here the δ term is used to increase the repulsion between the nanofiller and the polymer. Modifying the parameter, s increased the nano-filler sizes (In all our simulations, σ_f was kept fixed at 2.0σ). Increasing values of ε_{fp} implies an increase in the attraction between the nano-filler and the polymer chains, this interaction was held at $\varepsilon_{fp} = 2.0$, in order to prevent cluster formation of the nano-fillers (nano-filler to nano-filler coupling) in the systems [15]. We note that we have used this model to study homopolymer nanocomposites systems [14][16][17] and in this paper we have extended it to study polymer blends.

For all the systems shown in this paper we used a system of size 32 x 32 x 16 σ in the x, y and z directions respectively. The simulation box was chosen such that the thickness was roughly 7 times the radius of the polymer (as was used in the experiments). We used periodic boundary conditions in the x and y directions, while the z direction was bounded by walls, consisting of two layers of 111 fcc atoms. The interaction parameter, ε, between the wall atoms and the polymers and the nanofillers was fixed at $\varepsilon = 4.0$. We used a fifth order predictor corrector algorithm with a time interval of $t= 0.005\tau$. Constant temperature was maintained at $T = 1.1(K_b/\varepsilon)$ by using a Langevin thermostat.

For the first set of simulations, we used volume fraction of filler ranging from Φ=0.0%, 3.13%, and 12.52%. We introduced a slight repulsion between the two polymers by setting δ = 0.75. We kept the polymer-surface interactions to be the same for both polymers, (at ε=4.0) and for the nanoparticle, we kept the interaction between the nanoparticle and the two polymers to be identical (at ε_{fp}=2.0). In all these simulations we started from a completely mixed state (δ = 1.0) and then equilibrated the system (in the NPT ensemble) for at least 4 x 10^4 τ. Once our system was equilibrated, and we determined this by monitoring the radius of gyration of the chains (Rg), and the diffusion of the center of mass of the polymer (on the order of several Rg's), we then reduced the value of δ to 0.75 and re-equilibrated for another 4 x 10^4 τ, under NVT conditions. Snapshots of our system at different timesteps are shown in Figure 3-2 . As can be seen from the figure, an initially mixed state evolves into two columnar phases, which ultimately merge to form a single columnar structure. What should also be noted from the figure is that most of the nanoparticles tend to segregate to the interface between the two phases. For most of the simulations that we have run (typically starting from 3-5 random initial states), we see the system starting off with multiple columns and then merging into one, as would be expected during phase separation. However we see instances in systems with Φ=12.52%, that the two columns do not merge. We think this is a result that is also expected, as a larger number of fillers (segregated to the interface) can lower the local interfacial tension and possibly stabilize multiple columns. We note that this is something that is typically observed when copolymer compatibilizers are used in polymer blends, where the domain sizes decrease. If even higher concentration of filler at Φ=25.04% (all other parameters remaining the same) were used we see this phenomena again (as expected). In Figure 3-3, the two columns persist even after twice the normal equilibration time (to 8 x 10^4 τ). We recognize that this is a function of the initial starting point, and so is not an equilibrium structure, as even at these higher concentrations we see cases that merge into a single column. However, we anticipate that in the experimental results, since the chains are longer and kinetic effects are more pronounced, we will always see multiple columns. It is important to recognize, that in all cases, these columns span the complete thickness of the film, and the nanoparticles segregate to the interface between the polymers.

For the next set of simulations, we examined the effect of changing the interaction between the nanoparticle and the polymer phases. We chose an interaction that made the nanoparticle slightly repulsive to one phase (the non-photoactive polymer), by introducing a parameter δ_f, which reduces the attractive portion of the L-J potential. Any value of $\delta_f < 1$ denotes a repulsive interaction between the nanoparticle and the non-photoactive phase. We performed our usual equilibration procedure using a filler volume fraction Φ=12.52% (and $\delta = \delta_f = 1$) Once the system has been equilibrated we then reduce the values of δ to 0.75 and δ_f to 0.9. As can be seen from the snapshots after $4 \times 10^4\ \tau$ (Figure 3-4), far more nanoparticles are localized at the interface between the two phases with $\delta_f = 0.9$. To quantify the localization of the nanoparticles we constructed a simulation geometry in which we have a system with polymer A on top, and polymer B at the bottom (inset in Figure 3-5). We divided the simulation box into 16 partitions along the z direction and plotted the filler fractions in each partition (Figure 3-5). As we decrease the value of δ_f, we notice that almost all the nanoparticles are now present in the photoactive polymer. However, at lower values of delta, the amount of nanofiller at the interface decreases, implying that there is an optimum value of interactions that can be tailored by choosing the non-photoactive polymer appropriately.

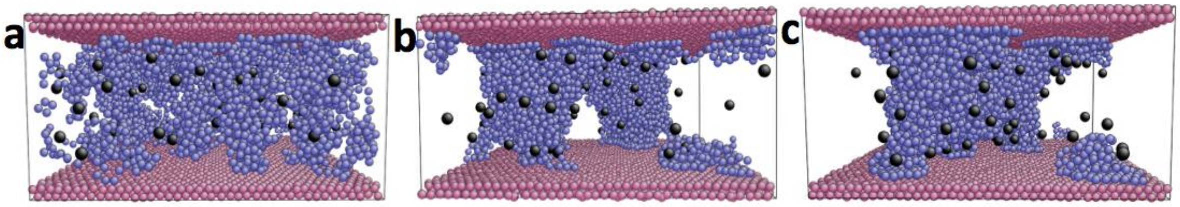

Figure 3-2 Morphologies obtained by MD simulations. In both (a) and (b) and (c) the blue represents the photoactive polymer, and the larger spheres (black) represent the nanofiller particles. The other polymer (non-photoactive) is not shown for clarity. In all these simulations the volume fraction of filler was Φ=3.13%. (a) Initial state before phase separation. (b) Snapshot at 2 x 10^4 τ. (c) Snapshot at 4 x 10^4 τ, note how the two columns have merged.

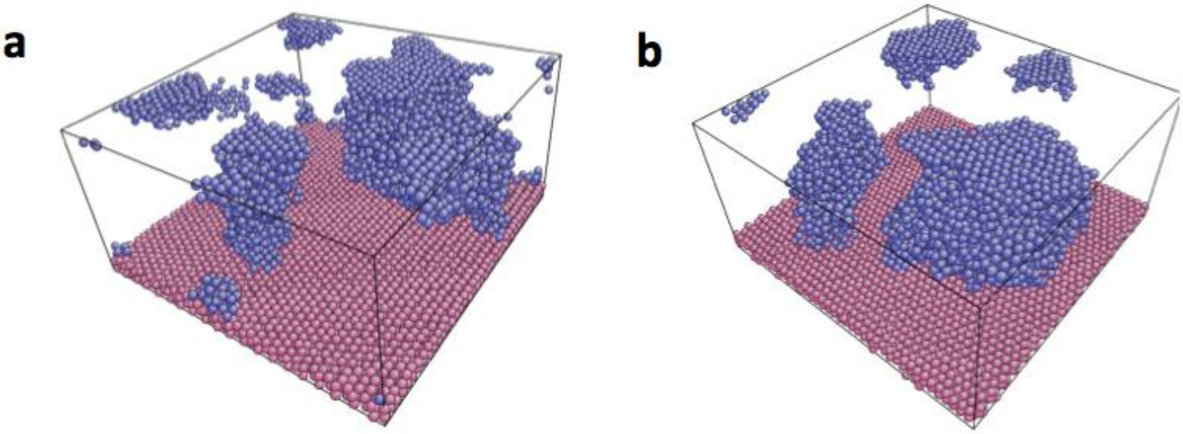

Figure 3-3 Morphologies obtained by MD simulations at higher filler concentrations Φ=25.04% (In these snapshots, the top wall is not shown and only the photoactive polymers (blue) were shown for clarity. (a) Snapshot at 4 x 10^4τ. (b) Snapshot at 8 x 10^4 τ. Note that we do not see any merging of the columns at these filler concentrations.

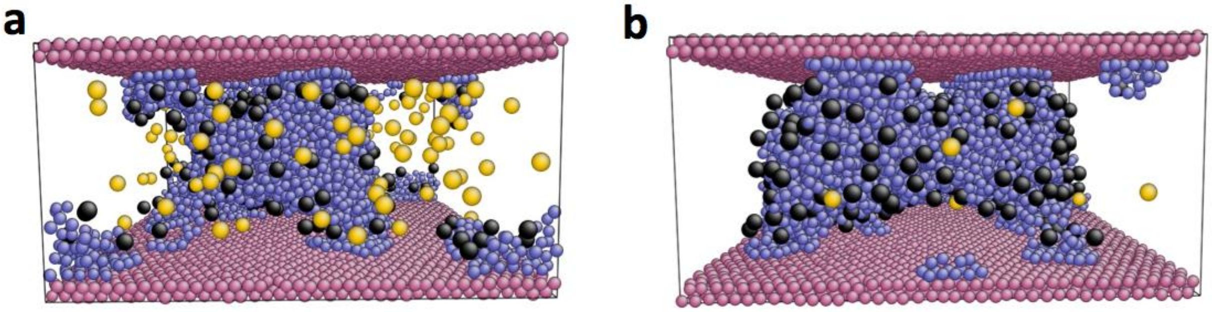

Figure 3-4 Snapshot of simulation systems. In both (a) and (b) we fixed the volume fraction of fillers at Φ=12.52%, δ=0.75 (between the polymers) and ran the simulation for 4 x $10^4\tau$. To distinguish between nanofillers at the interface and the ones in the non-photoactive polymer, fillers at A-B interfaces are black, while those distributed in the non-photoactive phase are yellow. (a) Simulation system with δ_f =1.0. (b) Simulation systems with δ_f =0.9.

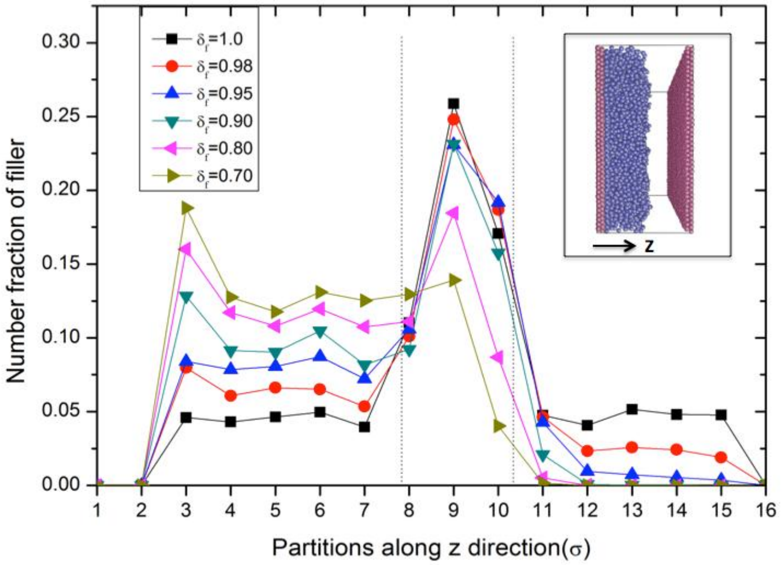

Figure 3-5 Number fraction of fillers in each partition along z direction for different degrees of repulsion with the non-photoactive phase. δ was 0.75 between polymer A and B, volume fraction of filler Φ=12.52%. The inset shows the geometry of polymer A and B that were used in this test.

3.3 Neutron scattering and analysis

To test these simulations, we first wanted to confirm that the interface does indeed template nanoparticle segregation, and that this effect is generic for a pair of incompatible polymers. We started with a simple bilayer geometry, where a 40nm thick layer of P3HT was first spun cast on an HF etched silicon wafer and covered with another layer of deuterated PS (Mw=50K) floated from the surface of a distilled water bath. The scheme of procedures is shown in Figure 3-6.

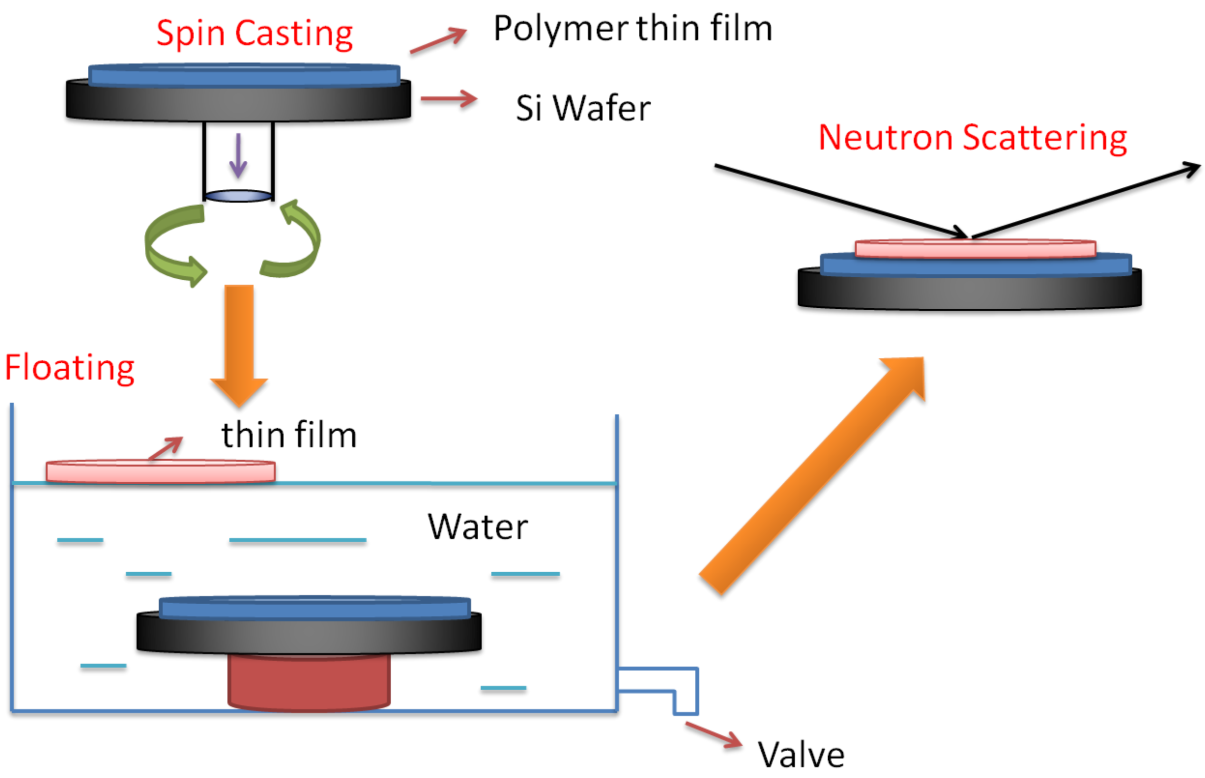

Figure 3-6 Scheme of procedures for preparation of bilayer thin film for neutron scattering

Three types of samples were formed; one in which the PCBM was added to the dPS layer, another where the PCBM was added to the P3HT layer, and a bilayer without PCBM. All samples were annealed above the glass transition temperature of PS for at least 90 minutes. The neutron reflectivity data are shown in Figure 3-7, together with the electron density (Figure 3-8) and concentration profiles which provided the best fits to the data. The scattering length density profiles, used to generate the concentration profiles are given in the supplementary materials. The parameters obtained from the neutron reflectivity data are summarized in Table 3-1. From the figure we can see that in the absence of PCBM a stable interfacial width of 1.5nm between the two polymers is reached within 90 minutes. Upon addition of PCBM in the dPS layer we obtain the PCBM distribution shown in Figure 3-7e. From the figure we see that after 90 minutes of annealing, a 16 nm thick layer of PCBM is observed at the polymer/polymer interface, and another PCBM rich layer is observed to segregate at the Si interface, as previously reported by Karim et al. for a single PS/C_{60} layer where the favorable interactions between nanoparticles and the Si surface were found to stabilize the film against dewetting [18]. The bimodal distribution of the nanoparticles indicates that they are mobile in the PS phase, and diffuse towards the P3HT phase, where a layer becomes pinned at the interface, while the particles in the bulk become depleted by the favorable interaction with the Si surface. In Figure 3-7c we show the reflectivity spectra of the bilayer sample, when the PCBM is in the P3HT phase. Here we find no diffusion of the PCBM into the dPS phase, confirming that the nanoparticles prefer the P3HT phase. From the Figure 3-7f we can see that in this case as well, two layers approximately 2-4 nm thick have formed, at the polymer/polymer interface and the Si interface. We believe that the thicker layer formed at the polymer/polymer interface when PCBM is placed in the dPS phase is a result of a diffusion hindered process. However, regardless of the polymer phase where the PCBM is placed initially, a layer will be formed at the phase interface to reduce the overall energy of the system, in agreement with the predictions of the model shown in Figure 3-6. Furthermore, the data from the experiments indicate that the distribution of filler particles are similar to those suggested by Figure 3-6, where there is a slight repulsion between the nanoparticles and the PS phase, resulting in almost no nanoparticles diffusing to that phase when they are started out in the P3HT phase.

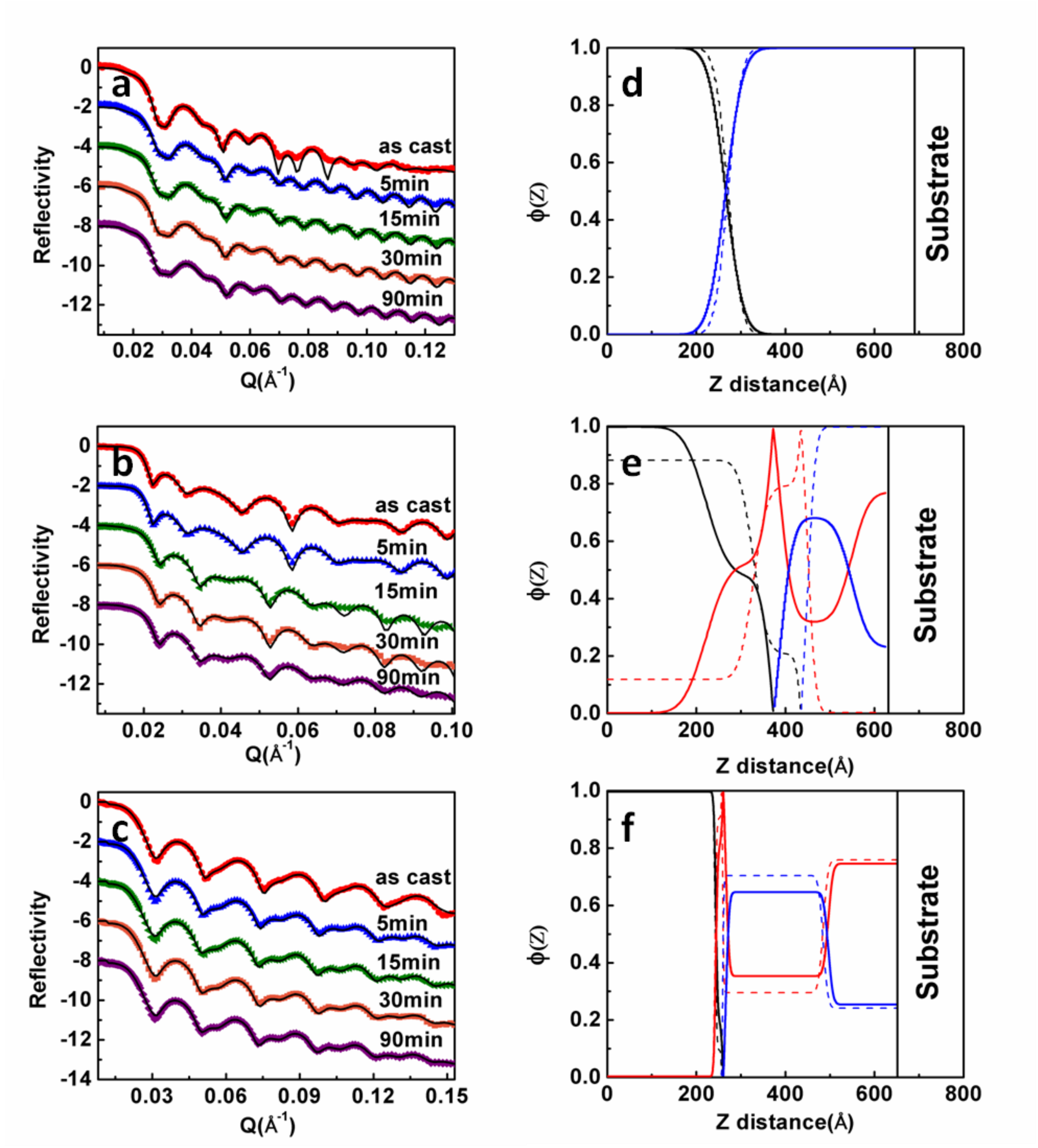

Figure 3-7 Neutron reflectivity profiles (left) and the corresponding volume fraction profiles (right) which provided the best fits for the data for bilayer samples: (a) The dPS layer is floated on top of the P3HT layer which is spun cast on HF etched Si. (b) A layer containing dPS and PCBM in a 1:1 weight ratio blend floated onto a P3HT layer spun cast onto an HF etched Si wafer. (c) A dPS layer is floated onto a P3HT layer containing 50% w/v PCBM, spin cast onto an HF etched Si wafer. Samples labled “as cast” (red) were dried in vacuum below Tg of all components, at T= 50 ℃. The other samples were annealed in a vacuum of 10^{-7} Torr at 150 ℃

for 5min (blue), 15min (olive), 30min (orange) and 90min (purple) and labeled accordingly. The volume fraction of dPS is shown in black, P3HT in blue and PCBM in red. As cast samples are shown as dash lines and samples annealed for 90 minutes are shown as solid lines.

As to the sampled-PS/PCBM (top layer)/P3HT (bottom layer), volume fraction in accordance to the depth of Z direction is calculated by:

$$top\ layer \begin{cases} \phi(dPS) = \dfrac{\rho_Z - \rho_{PCBM}}{\rho_{dPS} - \rho_{PCBM}} \\ \phi(PCBM) = \dfrac{\rho_{dPS} - \rho_Z}{\rho_{dPS} - \rho_{PCBM}} \end{cases}$$

$$bottom\ layer \begin{cases} \phi(PCBM) = \dfrac{\rho_{P3HT} - \rho_Z}{\rho_{P3HT} - \rho_{PCBM}} \\ \phi(P3HT) = \dfrac{\rho_Z - \rho_{PCBM}}{\rho_{P3HT} - \rho_{PCBM}} \end{cases}$$

where ϕ is the volume fraction for each component, $\rho_{\mathrm{dPS,}}$ $\rho_{\mathrm{PCBM,}}$ ρ_{P3HT} is the standard scattering length density for dPS, PCBM and P3HT, ρ_{Z} is the real scattering length density at certain depth of Z direction

Table 3-1. Neutron Scattering Parameters. T1 is the thickness of PCBM layer at the interface between dPS and P3HT; T2 is the thickness of PCBM layer at the bottom; Interfacial width is the width between two polymer layers

sample	**T1 (nm)**	**T2 (nm)**	**interfacial width (nm)**
dPS on P3HT	0	0	1.5
dPS/PCBM on P3HT	16.1	7.7	4.4
dPS on P3HT/PCBM	2.2	4.2	0.4

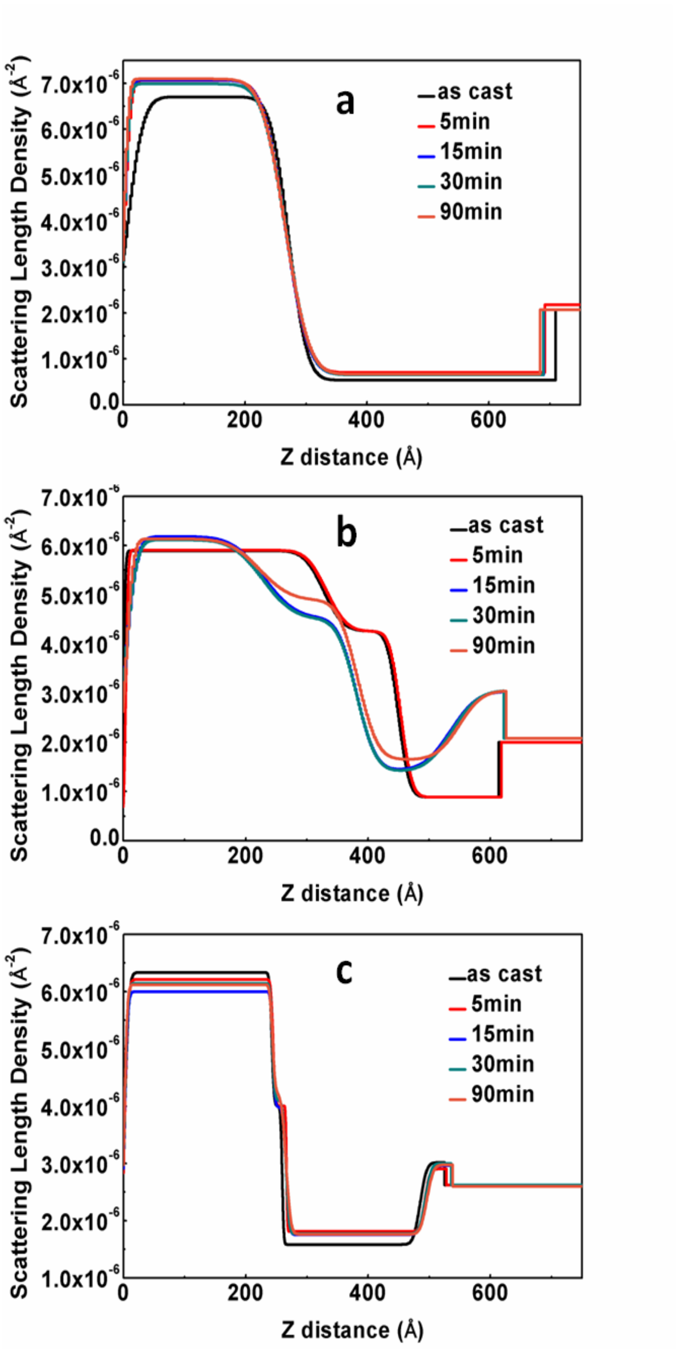

Figure 3-8 Electron density functions which provided the best fits to the neutron scattering data shown in Figure 2, plotted versus the distance from the sample surface. (a) The dPS layer is floated on top of the P3HT layer which is spun cast on HF etched Si. (b) A layer containing dPS and PCBM in a 1:1 weight ratio blend floated onto a P3HT layer spun cast onto an HF etched Si wafer. (c) A dPS layer is floated onto a P3HT layer containing 50% w/v PCBM, spin cast onto an HF etched Si wafer. Samples labled "as cast" were dried in vacuum below Tg of all components, at T= 50 ℃. The other samples were annealed in a vacuum of 10^{-7} Torr at 150 ℃ for 5min, 15min, 30min and 90min and labeled accordingly.

3.4 AFM characterization and analysis

Having determined that our experimental parameters are in the same phase space as the model parameters, we next proceeded to test whether we would also observe the columnar structures predicted by the model. We spun cast 1:1 weight ration mixtures of P3HT and PCBM, 1:1 weight ratio mixtures of the polymers or 1:1:1 weight ratio mixtures of the polymers and PCBM onto HF etched Si wafers and annealed them in UHV (ultra high vacuum) for one hour at 150 ℃. The morphology of the samples was first checked with atomic force microscopy (AFM). We first compare the difference of surface morphology between the sample without secondary polymer-polystyrene and with polystyrene. The AFM images are shown in the Figure 3-9. It is found that the surface of P3HT/PCBM thin film is very flat after thermal annealing. No significant topographical difference can be observed for this sample. However, after introducing a secondary polymer which is immiscible with P3HT, obvious phase separation can be detected by AFM. The AFM images for polymer blends (P3HT and PS) samples without and with PCBM nanoparticels are shown in Figure 3-10. From the figure we can see that the polymers have phase segregated in topographically high and low domains. In figure 3-10c and 3-10d we show cross sectional scans of magnified sections of the images, from where we can see that the boundaries between phases are different between the samples without and with PCBM. In the absence of PCBM we find that the segregation occurs with a raised rim surrounding the discontinuous phase followed by slight depression between the spherical segregated regions. When PCBM is present we find a pronounced depression around the discontinuous phase followed by a slight peak in the continuous phase. If we assume that the continuous phase is PS and the spherical domains are mostly P3HT, then based on the results of the simulation and the neutron reflectivity data, we would expect that the interfacial regions be enriched in PCBM. From the NR data we find that PCBM is incompatible with PS, hence the morphology is then consistent with PS forming a rim as it dewets the P3HT regions, but when PCBM is present, forming a depression, as the PS is excluded from the PCBM. But since these images just reflect topography contrast, they cannot be used to determine the location of the PCBM, or confirm the chemical differences between the domains.

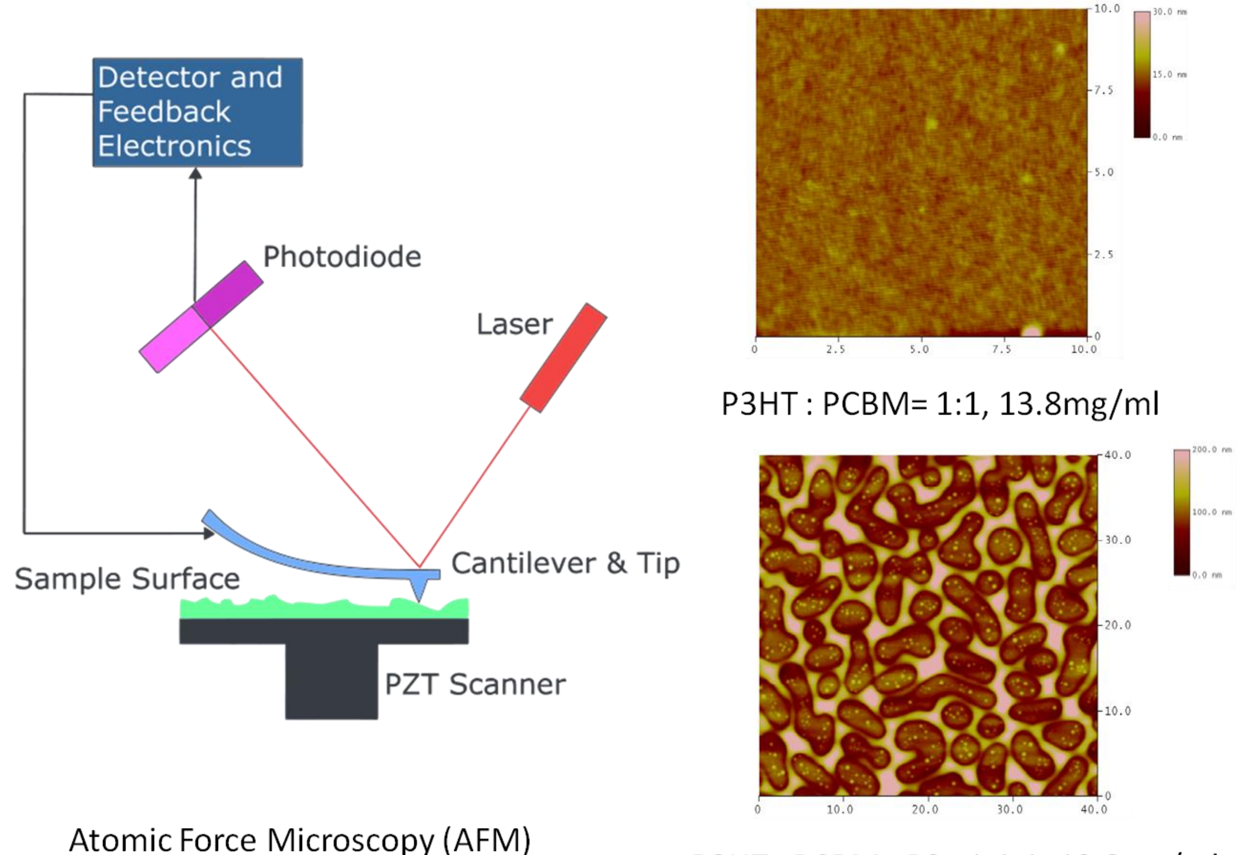

Atomic Force Microscopy (AFM)

P3HT : PCBM= 1:1, 13.8mg/ml

P3HT : PCBM : PS= 1:1:1, 13.8mg/ml

Figure 3-9 Scheme of atomic force microscopy and comparison of surface morphology between P3HT:PCBM=1:1 (weight ratio) sample and P3HT:PCBM:PS =1:1:1 sample.

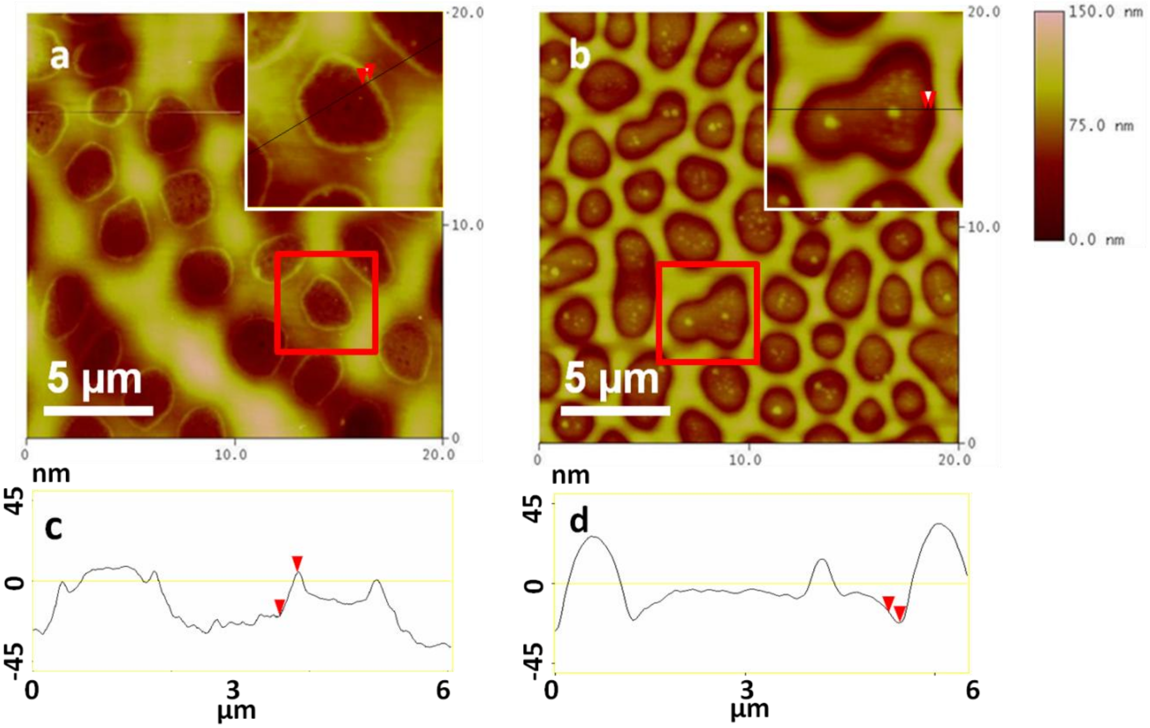

Figure 3-10 AFM topography images for films spun cast on HF etched Si wafers at 700rpm (a) PS/ P3HT blend thin film with 1:1 weight percent and (b) PS, P3HT and PCBM blend film blended in a 1:1:1 weight percent ratio. Inset is the magnified image of the area where we obtain the cross sectional information (c) and (d) corresponding to samples (a) and (b). The area at the edge of one of the domains is marked by red arrows, which correspond to the region marked in the same manner on the cross sectional scan.

3.5 TEM characterization and analysis

In order to confirm the location of the PCBM transmission elector microscopy (TEM) was performed on both thin films and cross sectional areas. In Figure 3-11, the TEM images of P3HT: PS=1:1 (weight ratio) and P3HT: PS: PCBM=1:1:1 (weight ration) are presented. Significant difference at the boundary of the domain can be observed. In Figure 3-12 we show TEM images of the same sample with the presence of PCBM, which were floated and annealed on the TEM grids. In Figure 3-12a we show low magnification images, where the denser P3HT phase appears darker than the PS phase, due to the mass-absorption scattering mechanism, providing contrast without additional staining. Addition of PCBM introduces additional contrast throughout the P3HT phase, and a clear ring is observed at the interface between PS and P3HT. It should be noted that the ring is present even when small amount of PS are trapped inside the P3HT domains. The clear interface ring is approximately 16 nm thick composed of PCBM is clearly visible. In this image we can also see clusters of PCBM throughout the P3HT phase, and occasional clusters still trapped in the PS phase. A region with increased PCBM concentration is also seen in the vicinity of the interface, whose thickness and PCBM content is similar to the layer observed with neutron reflectivity in Figure 5b. When the films are formed by spin casting, all phases are miscible in the toluene solvent and hence PCBM is found in both phases in the as cast films. Annealing produces a situation similar to the one observed with neutron scattering, where a layer of PCBM is trapped at the interfaces, hindering the diffusion of the PCBM from the PS phase in the P3HT phase.

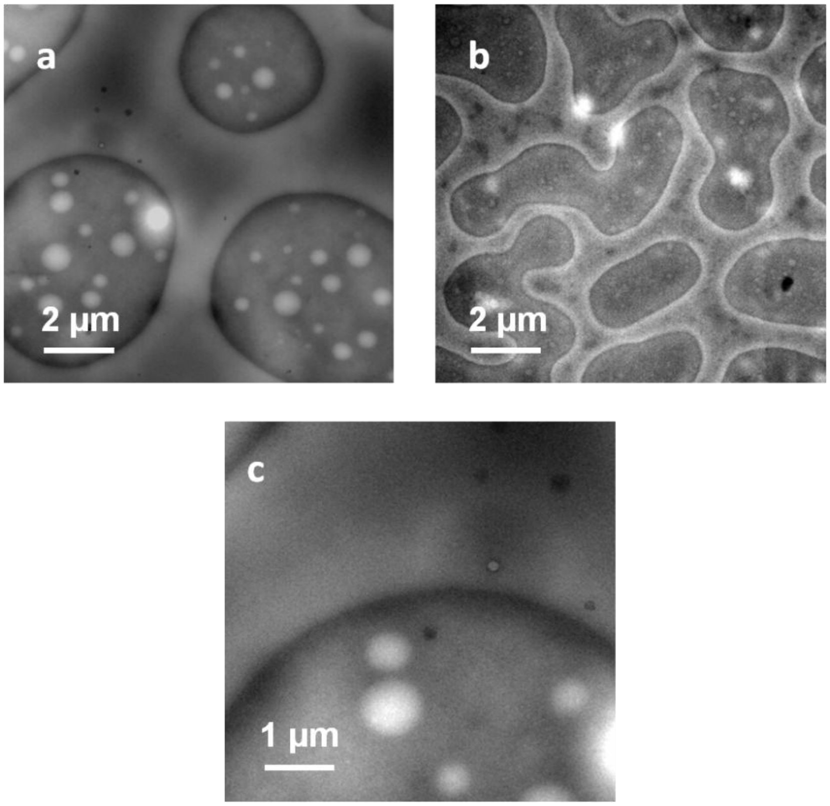

Figure 3-11 Transmission Electron Microscopy (TEM) images of spun cast films floated and annealed on TEM grids : (a) Symmetric binary blend film of PS and P3HT blend thin film with 1:1 weight/volume ratio; (b) Tertiary blend film of PS, PCBM and P3HT mixed in a 1:1:1 ratio; (c) Higher magnification for PS:P3HT=1:1 sample;

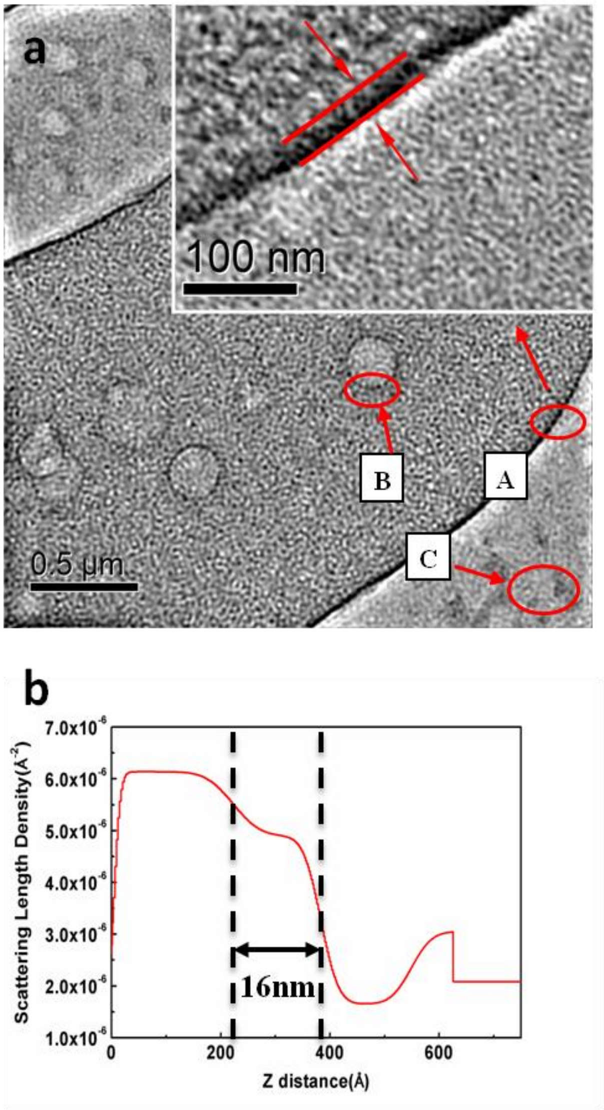

Figure 3-12 (a) Transmission Electron Microscopy (TEM) images of spun cast films floated and annealed on TEM grids of tertiary blend film of PS, PCBM and P3HT mixed in a 1:1:1 weight ratio. Note the dark edge present at the interface of two phases in the large (A) and small (B) phase segregated regions indicating larger concentrations of PCBM, which is more electron dense than either polymer matrix. Note PCBM is mostly segregated in the P3HT phase, with smaller regions still in the PS phase (C). Insert: High magnification image of area A showing the width of the PCBM interfacial region. (b) Electron scattering density which provides the best fit to the neutron scattering spectra obtained from the shown in Figure 2b. The width of the polymer/polymer interface corresponding to the PCBM rich region is marked.

In order to obtain side views of the samples, focused ion beam (FIB) cross-section samples are prepared by spinning cast P3HT and PCBM with 1:1 weight ratio onto the clean silicon wafer, followed by Ga ion beam mill and lift out technique [19] utilizing FEI Helios focused ion beam system (as shown in Figure 3-13). The samples are then observed under transmission electron microscopy JEOL 1400 and shown in Figure 3-14. From the figures we can clearly see that regardless of the presence of PCBM, the phase segregated structures are cylindrical, spanning both interfaces, and higher magnification images of the features where PCBM is present show particles segregated at both the Si and polymer interfaces.

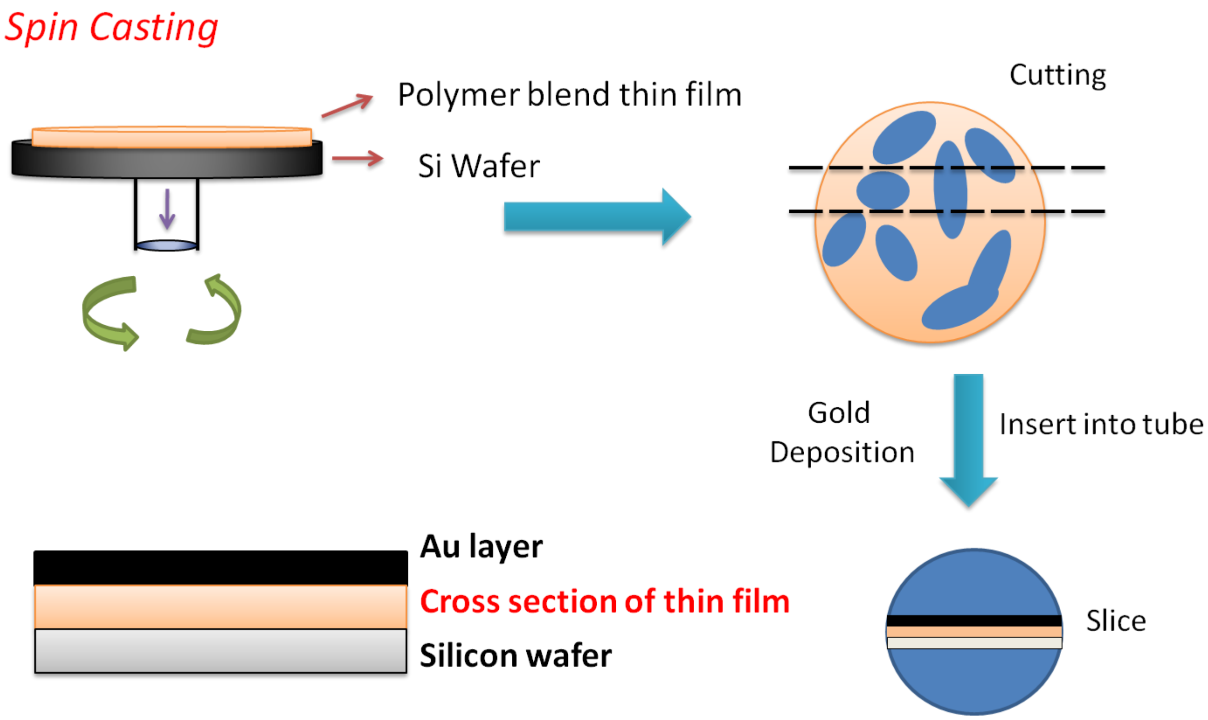

Figure 3-13 Scheme of procedures for preparation of cross-section sample for TEM

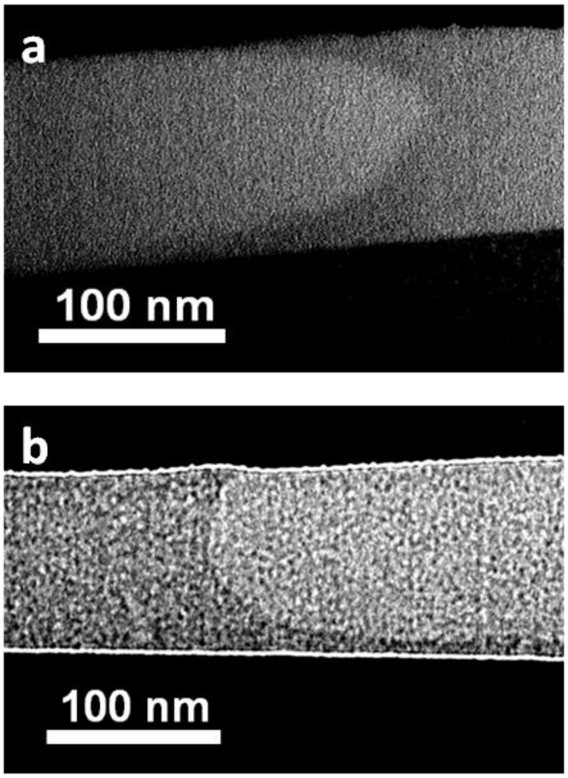

Figure 3-14 TEM images of focused ion beam cross sections obtained from films spun cast on HF etched Si wafers at 700rpm; (a) The 1:1 weight ratio PS / P3HT binary blend film and (b)the 1:1:1 weight ratio PS, P3HT and PCBM tertiary blend film.

3.6 Conclusion

In conclusion, by introducing a secondary polymer which is immiscible with neither P3HT nor PCBM, the self assembled columnar structure within the polymer blend thin film is achieved. We first test our idea by molecular dynamics simulation to predict the morphology in according to the different preference to each other and nano fillers. Then polystyrene is chosen since it is immiscible with neither P3HT nor PCBM that most possible to create columnar structure with PCBM segregated along the interface between two polymers. The proposed structure is then confirmed by neutron scattering, AFM and TEM measurement, which opens the door to apply this structure on the real BHJ solar cell device.

References

[1] Balazs, Anna C., Todd Emrick, and Thomas P. Russell. "Nanoparticle polymer composites: where two small worlds meet." *Science* 314, no. 5802 (2006): 1107-1110.

[2] Böker, Alexander, Jinbo He, Todd Emrick, and Thomas P. Russell. "Self-assembly of nanoparticles at interfaces." *Soft Matter* 3, no. 10 (2007): 1231-1248.

[3] Si, Mayu, Tohru Araki, Harald Ade, A. L. D. Kilcoyne, Robert Fisher, Jonathan C. Sokolov, and Miriam H. Rafailovich. "Compatibilizing bulk polymer blends by using organoclays." *Macromolecules* 39, no. 14 (2006): 4793-4801.

[4] Tanaka, Hajime, Andew J. Lovinger, and Don D. Davis. "Pattern evolution caused by dynamic coupling between wetting and phase separation in binary liquid mixture containing glass particles." *Physical review letters* 72, no. 16 (1994): 2581.

[5] Balazs, Anna C., Todd Emrick, and Thomas P. Russell. "Nanoparticle polymer composites: where two small worlds meet." *Science* 314, no. 5802 (2006): 1107-1110.

[6] Karim, Alamgir, Jack F. Douglas, Giovanni Nisato, Da-Wei Liu, and Eric J. Amis. "Transient target patterns in phase separating filled polymer blends."*Macromolecules* 32, no. 18 (1999): 5917-5924.

[7] Lee, Jong-Young, Qingling Zhang, Todd Emrick, and Alfred J. Crosby. "Nanoparticle alignment and repulsion during failure of glassy polymer nanocomposites." *Macromolecules* 39, no. 21 (2006): 7392-7396.

[8] Pütz, Mathias, Kurt Kremer, and Gary S. Grest. "What is the entanglement length in a polymer melt?." *EPL (Europhysics Letters)* 49, no. 6 (2000): 735.

[9] Kremer, Kurt, and Gary S. Grest. "Dynamics of entangled linear polymer melts: A molecular‐dynamics simulation." *The Journal of Chemical Physics* 92 (1990): 5057.

[10] Praprotnik, Matej, Luigi Delle Site, and Kurt Kremer. "Adaptive resolution molecular-dynamics simulation: Changing the degrees of freedom on the fly."*The Journal of chemical physics* 123 (2005): 224106.

[11] Grest, Gary S., and Kurt Kremer. "Molecular dynamics simulation for polymers in the presence of a heat bath." *Physical Review A* 33, no. 5 (1986): 3628.

[12] Liu, Hong, and Amitabha Chakrabarti. "Shear effects on phase separating polymer solutions: A molecular dynamics study." *The Journal of Chemical Physics* 112 (2000): 10582.

[13] Bresme, Fernando, and Nicholas Quirke. "Nanoparticulates at liquid/liquid interfaces." *Physical Chemistry Chemical Physics* 1, no. 9 (1999): 2149-2155.

[14] Gersappe, Dilip. "Molecular mechanisms of failure in polymer nanocomposites." *Physical review letters* 89, no. 5 (2002): 058301-058301.

[15] Balazs, Anna C. "Theory and simulation of polymers at interfaces." *MRS Bulletin* 22, no. 01 (1997): 13-15.

[16] Luo, Haobin, and Dilip Gersappe. "Dewetting dynamics of nanofilled polymer thin films." *Macromolecules* 37, no. 15 (2004): 5792-5799.

[17] Jaber, Eihab, Haobin Luo, Wentao Li, and Dilip Gersappe. "Network formation in polymer nanocomposites under shear." *Soft Matter* 7, no. 8 (2011): 3852-3860.

[18] Bandyopadhyay, Diya, Jack F. Douglas, and Alamgir Karim. "Influence of C60 Nanoparticles on the Stability and Morphology of Miscible Polymer Blend Films." *Macromolecules* 44, no. 20 (2011): 8136-8142.

[19] Tham, Douglas, CY. Nam, and John E. Fischer. "Microstructure and Composition of Focused‐Ion‐Beam‐Deposited Pt Contacts to GaN Nanowires."*Advanced Materials* 18, no. 3 (2006): 290-294.

Chapter 4

Enhancing the Efficiency of Bulk Heterojunction Solar Cell via Templated Self Assembly

4.1 Introduction

As we successfully confirm the construction of columnar structure by mixing P3HT, PCBM with PS, our next step naturally comes to the application of this promising structure on the real BHJ solar cell device. The procedures of sample preparation and performance test are described, as well as the analysis of the results. If this specific structure indeed enhance the power conversion efficiency, possible mechanisms should be discussed which is beneficial for further optimization.

4.2 Experiment

For device fabrication, indium tin oxide (ITO) coated glass slide is polished in UV O-zone for 10 minutes. A 50nm-thick poly(3,4-ethylenedioxythiophene) : poly(styrenesulphonate) (PEDOT:PSS) layer is spun cast onto the ITO glass at 5000 rpm for 45 seconds and was baked at 140 ℃ for 10 minutes on the hot plate exposed to the air. 13.8mg/mL P3HT and PCBM of 1:1 weight ratio and 13.8mg/mL polystyrene, P3HT and PCBM with 1:1:1 weight ratio (dissolved in chlorobenzene) are spun cast onto PEDOT:PSS layer separately at 700 rpm for 45 seconds. Both of them are spun cast in the air. Aluminum electrode with 100 nm thickness is then deposited onto the sample at 1 Å/s speed in PVD at pressure lower than 3×10^{-7} Pa. The whole device is then annealed in vacuum oven at 150 ℃ for 1 hour, followed by erasing one side edge and painting the conductive silver paste. The picture of as-prepared sample is shown in Figure 4-1. The performance of solar cell device was tested by a 150W solar simulator (Oriel) with an AM 1.5G filter for solar illumination. The light intensity was calibrated to 100 mW cm^{-2} by a calibrated thermopile detector (Oriel).

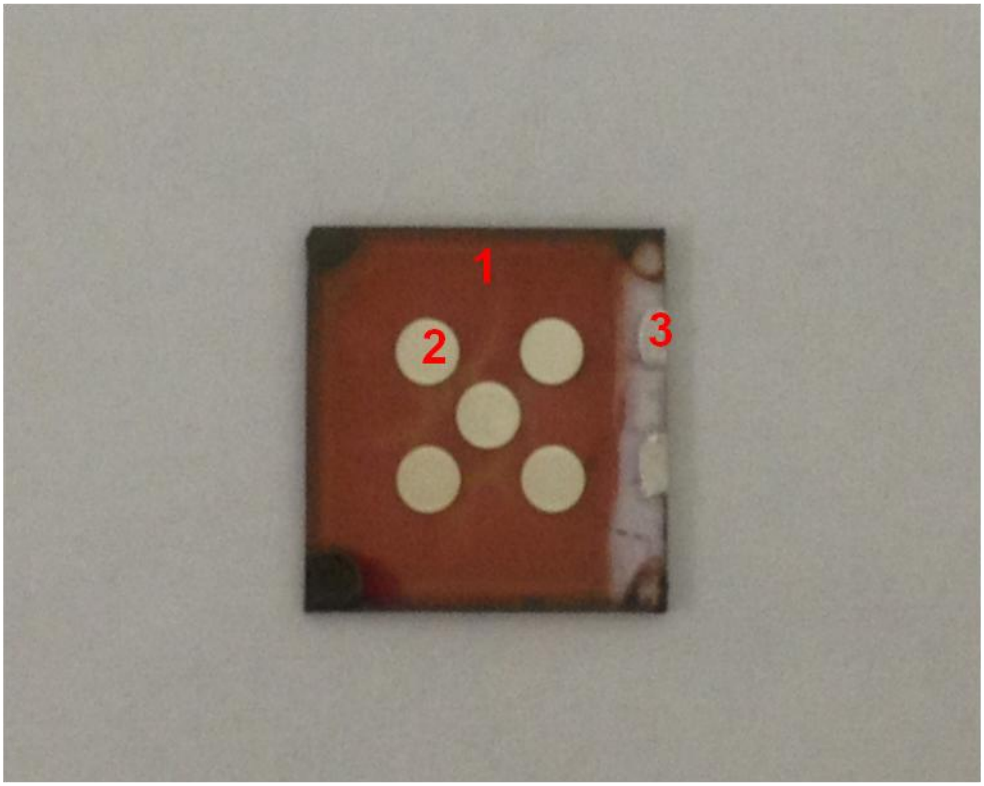

Figure 4-1 Picture of a real BHJ solar cell device that is ready for test, where 1 represents the active layer thin film, 2 represents the Al electrode contact, 3 represents the silver paste for good conductivity.

4.3 Results and discussion

Films of P3HT/PCBM/PS compositions were spun cast on the standard PEDOT/PSS substrates in preparation for the production of BHJ solar cells. Since the sample morphology may differ on different substrates we imaged these samples again with scanning force microscopy. In Figure 4-2 we show the topographical images, which appear very similar to those observed on the Si substrates, including the raised/depressed rim phenomenon for samples without and with PCBM, confirming the presence of PCBM at the interfaces. In Figure 4-2c and 4-2d we also show the lateral force images where the harder sections correspond to the continuous phase, while the softer, darker regions correspond to the discontinuous spherical domains. Since the glass transition temperature of PS, Tg~100 ℃, while Tg of P3HT in blend film is Tg~50 ℃ [20], the PS is expected to be the harder phase.

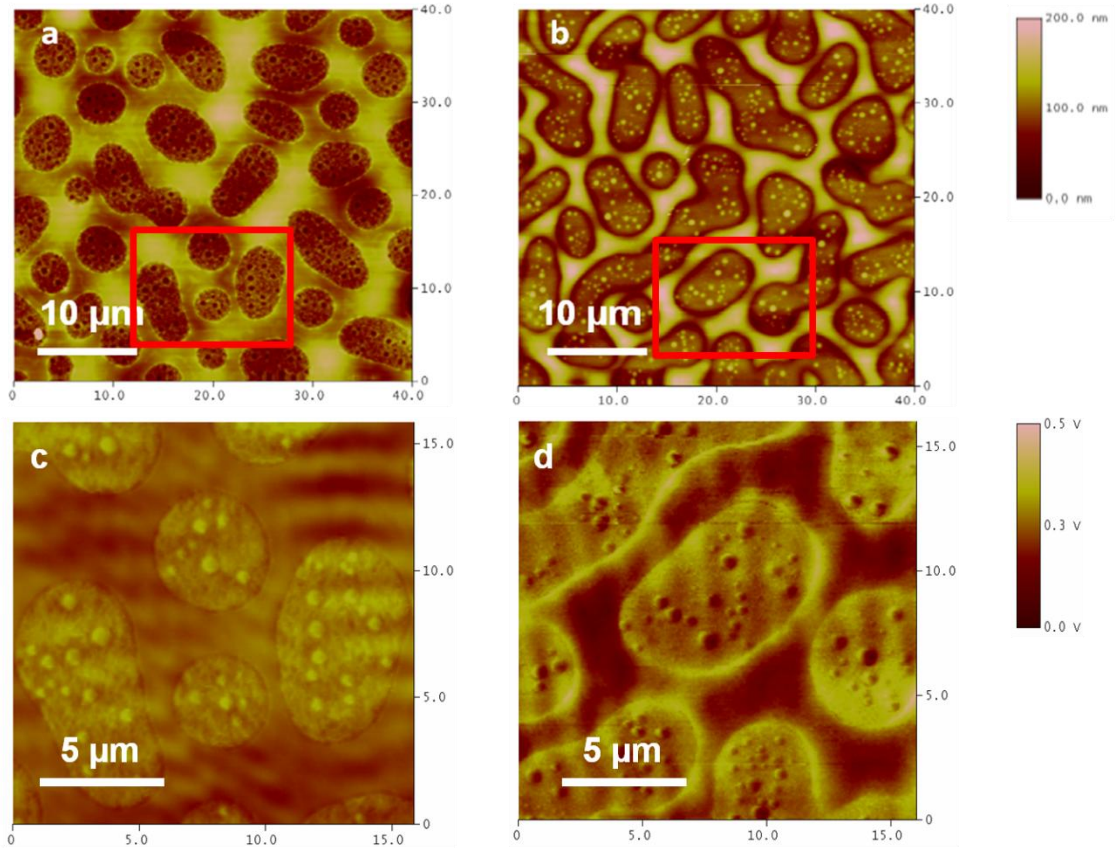

Figure 4-2 AFM topography images for films spun cast on PEDOT/PSS coated ITO glass at 700rpm (a) PS/P3HT blend thin film with 1:1 weight and (b) PS, P3HT and PCBM blend film blended in a 1:1:1 weight ratio with lateral force images. Lateral force images corresponding to zoomed in region delineated by the red squares ; (c) for the sample shown in (a) and (d) for the sample shown in (b).

Figure 4-3 shows the comparison of the performance between the average output of five devices manufactured the in the standard manner without PS and five devices manufactured with PS and having films with the columnar structure within the active layer, where we find an average enhancement of 32.0% ± 6.5% in the conversion efficiency. The increase of short circuit current J_{sc} and fill factor FF% is mainly attributed to the enhancement of the charge-carrier transport and reduced recombination kinetics after building up the columnar structure in active layer. It is notable that the open circuit V_{oc} is enhanced as well, which reflects an improvement in the materials properties**.** The relatively low values for the control are typical for those previously reported for devices where the spin coating and electrical measurements are done in air [21]. Furthermore, the film thickness of the control sample was 50nm determined by ellipsometry compared to optimal thickness around 100nm from other literature values [22][23], because for the polymer blend samples, the amount of active P3HT polymer and PCBM was 30% less (13.8mg/ml compared to 20mg/ml). The highest efficiency of our control device is 1.1%, which is very comparable to 1.2% reported by van Bavel et al [24]. with the same thickness of active layer while the other parameters remain almost the same.

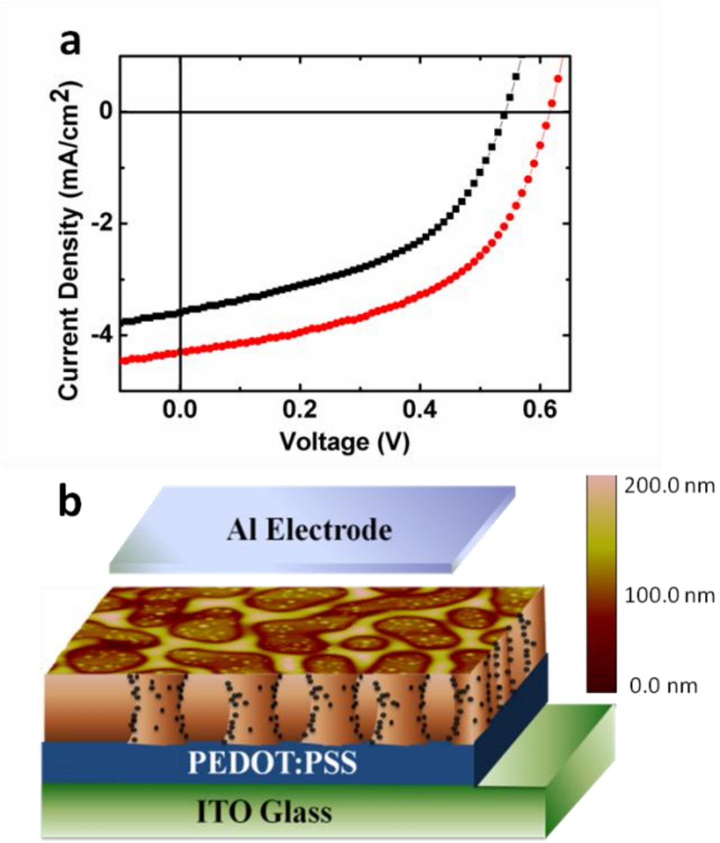

Figure 4-3 (a) Current density versus voltage to characterize the performance of a control P3HT/PCBM 1:1 weight by volume binary blend device (black trace) and the 1:1:1 P3HT/PS/PCBM tertiary blend film device (red trace) modified device. (b) Schematic showing the structure of the modified BHJ solar cell. The surface image was obtained from the two dimensional AFM scan of the film coated onto the PEDOT:PSS layer.

Table 4-1. Device performance comparison between different samples. V_{OC} is open circuit voltage, J_{SC} is short circuit current, FF is fill factor and PCE is power conversion efficiency which is calculated based on Equation 2-2

	V_{OC} (V)	**J_{SC} (mA/cm^{-2})**	**FF (%)**	**PCE (%)**
control	0.538±0.005	4.083±0.222	47.2±0.8	1.035±0.052
with PS	0.603±0.005	4.455±0.168	50.5±1.9	1.355±0.031

This result seems at first counter-intuitive, as we have added an insulated component into the active layer which could result in a worse performance for photovoltaics [25]. However, in our case the inert polymer results in a percolated columnar structure which improves the properties.

We note that similar effects have been seen when inert polymers are used to fabricate low-percolation threshold field-effect transistor (FET) [26]. Other literature suggests that adding insulated polymers into the conjugated polymers could provide efficient charge transport [27]. In our case, we believe that the columnar structure of P3HT with abundant PCBM particles at the interface provides the high interfacial area which enhances the ability of exciton dissociation and charge separation [28]. Furthermore, this columnar structure has good contact with collection electrodes and we do not compromise the efficient charge transportation for both holes and electrons. In this way, better performance can be predicted even with the addition of an insulated polymer to the active layer of BHJ solar cell.

4.4 Conclusion

In conclusion, a columnar structure within the active layer is achieved by phase separation between polystyrene and P3HT with the PCBM mostly aggregated at the interface between two phases, which is established by AFM, TEM cross-section and neutron reflectivity. This structure provides the large interfacial area between electron donor and acceptor, which enhances the exciton dissociation efficiency and carrier transportation. The as-prepared solar cell device exhibits the better J_{sc} and fill factor, leading to the higher efficiency. Since most of the PCBM stays at the interface even after long time annealing, this system potentially possesses thermal stability under operating conditions.

References

[1] Pearson, Andrew J., Tao Wang, Richard AL Jones, David G. Lidzey, Paul A. Staniec, Paul E. Hopkinson, and Athene M. Donald. "Rationalizing phase transitions with thermal annealing temperatures for P3HT: PCBM organic photovoltaic devices." *Macromolecules* 45, no. 3 (2012): 1499-1508.

[2] Nam, Chang‐Yong, Dong Su, and Charles T. Black. "High‐Performance Air‐Processed Polymer–Fullerene Bulk Heterojunction Solar Cells." *Advanced Functional Materials* 19, no. 22 (2009): 3552-3559.

[3] Li, Gang, Vishal Shrotriya, Yan Yao, and Yang Yang. "Investigation of annealing effects and film thickness dependence of polymer solar cells based on poly (3-hexylthiophene)." *Journal of Applied Physics* 98, no. 4 (2005): 043704-043704.

[4] Shaheen, Sean E., Christoph J. Brabec, N. Serdar Sariciftci, Franz Padinger, Thomas Fromherz, and Jan C. Hummelen. "2.5% efficient organic plastic solar cells." *Applied Physics Letters* 78 (2001): 841.

[5] van Bavel, Svetlana, Erwan Sourty, Gijsbertus de With, Kai Frolic, and Joachim Loos. "Relation between photoactive layer thickness, 3D morphology, and device performance in P3HT/PCBM bulk-heterojunction solar cells."*Macromolecules* 42, no. 19 (2009): 7396-7403.

[6] Babel, Amit, and Samson A. Jenekhe. "Morphology and field-effect mobility of charge carriers in binary blends of poly (3-hexylthiophene) with poly [2-methoxy-5-(2-ethylhexoxy)-1, 4-phenylenevinylene] and polystyrene."*Macromolecules* 37, no. 26 (2004): 9835-9840.

[7] Goffri, Shalom, Christian Müller, Natalie Stingelin-Stutzmann, Dag W. Breiby, Christopher P. Radano, Jens W. Andreasen, Richard Thompson et al. "Multicomponent semiconducting

polymer systems with low crystallization-induced percolation threshold." *Nature materials* 5, no. 12 (2006): 950-956.

[8] Kumar, Avinesh, Mohammed A. Baklar, Ken Scott, Theo Kreouzis, and Natalie Stingelin‐Stutzmann. "Efficient, Stable Bulk Charge Transport in Crystalline/Crystalline Semiconductor–Insulator Blends." *Advanced Materials*21, no. 44 (2009): 4447-4451.

[9] Ferenczi, Toby AM, Christian Müller, Donal DC Bradley, Paul Smith, Jenny Nelson, and Natalie Stingelin. "Organic Semiconductor: Insulator Polymer Ternary Blends for Photovoltaics." *Advanced Materials* 23, no. 35 (2011): 4093-4097.

Chapter 5

Hydrogen Fuel Cell Basics

5.1 Introduction

Hydrogen fuel cell is a device which can directly convert chemical energy in hydrogen to electrical energy under low temperature with the presence of catalysts. A polymer membrane, usually Nafion membrane, is utilized to separate ions and electrons, while two electrodes with certain loading of carbon black and platinum (Pt) catalyst are placed at both sides of the membrane to collect electrons (Figure 5-1). Therefore, hydrogen fuel cell is also called as "polymer electrolyte membrane fuel cell" or "proton exchange membrane fuel cell" with "PEMFC" as the abbreviation in both situations. The use of hydrogen fuel cell can greatly reduce the carbon dioxide release since the only emission from it is only pure water and heat. Moreover, it can be operated under low temperature and is very suitable to be applied on portable device. According to the DOE report, hydrogen fuel cell possesses 60% efficiency for transportation application and 35% efficiency for stationary, and is widely used in backup power, transportation vehicles and distributed generation [1]. However, the application of fuel cell is limited by its high cost mainly due to the use of expensive catalyst, and the sensitivity to the impurities (such as carbon monoxide and carbon dioxide) [2]. This chapter will discuss the working mechanism of hydrogen fuel cell, challenges for hydrogen fuel cell and current research on improving the performance of hydrogen fuel cell.

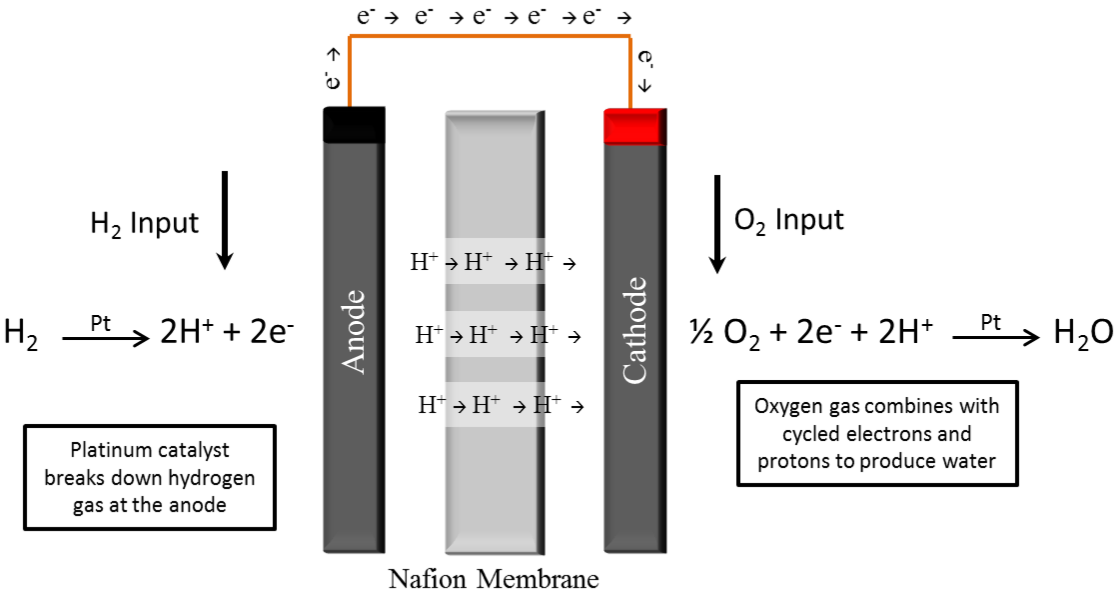

Figure 5-1 Scheme of hydrogen fuel cell’s structure

5.2 Mechanism of hydrogen fuel cell

5.2.1 Reactions at anode and cathode of hydrogen fuel cell

Generally, the reactions of hydrogen fuel cell contain: hydrogen oxidation reaction occurs at the anode and oxygen reduction reaction occurs at the cathode (E^{Θ} is the standard electrode potential):

$$\text{Anode: } H_2 - 2e^- \longrightarrow 2H^+ \quad E^{\Theta} = 0\ V \qquad (5\text{-}1)$$

$$\text{Cathode: } 1/2O_2 + 2H^+ + 2e^- \longrightarrow H_2O \quad E^{\Theta} = 1.229\ V \qquad (5\text{-}2)$$

$$\text{Total reaction: } H_2 + 1/2\ O_2 \xrightarrow{\textbf{Catalyst}} H_2O \quad E^{\Theta} = 1.229\ V\ [3] \qquad (5\text{-}3)$$

Hydrogen oxidation occurs readily on platinum-based catalysts. The kinetics of this reaction are very fast (rate constant about 10^{-5} $molsec^{-1}cm^{-2}$) [3] [4] and, in a fuel cell, hydrogen oxidation is usually controlled by mass transfer limitations [5]. Hydrogen oxidation also involves the adsorption of the gas on the catalyst surface followed by dissociation of the molecule and an electrochemical reaction to form two protons as shown below [6]:

$$2Pt_{(s)} + H_2 \longrightarrow 2Pt\text{-}H_{ads} \qquad (5\text{-}4)$$

$$Pt\text{-}H_{ads} \longrightarrow H^+ + e^- + Pt_{(s)} \qquad (5\text{-}5)$$

where $Pt_{(s)}$ is the free surface site on platinum and $Pt\text{-}H_{ads}$ is an absorbed hydrogen atom on the Pt active site.

The oxygen reduction reaction actually can proceed by two pathways in aqueous electrolytes, one is shown in Equation 5-2 which is called "four-electron pathway", and the other one is shown below known as peroxide pathway [7]:

$$O_2 + 2H^+ + 2e^- \longrightarrow HOOH \qquad E^{\Theta} = 0.670\ V \qquad (5\text{-}6)$$

$$HOOH + 2H^+ + 2e^- \longrightarrow 2H_2O \quad E^{\Theta} = 1.77\ V \qquad (5\text{-}7)$$

$$\text{or} \quad 2HOOH \longrightarrow 2H_2O + O_2 \qquad (5\text{-}8)$$

The rate constant of oxygen reduction reaction is very low and it is the rate determine step for hydrogen fuel cell reaction. In order to speed up the oxygen reduction reaction kinetics to reach a practically usable level for a fuel cell, a cathode catalyst is needed since the adsorption of an oxygen species to the surface of the catalyst is essential for electron transfer [8]. At the current stage, platinum based materials are proven to be the most efficient catalysts.

5.2.2 Mechanism of separation of ions and electrons

As mentioned above, a polymer membrane is used to separate ions and electrons in hydrogen fuel cell, which is usually referred as Nafion membrane, first discovered by Walther Grot of DuPont Company in late 1960s [9]. Nafion is a sulfonated tetrafluoroethylene based fluoropolymer-copolymer (Figure 5-2). A tetrafluoroethylene (Teflon) backbone gives Nafion its mechanical strength while the sulfonate groups as termination onto a tetrafluoroethylene (Teflon) backbone make Nafion possess ion conductivity [10].

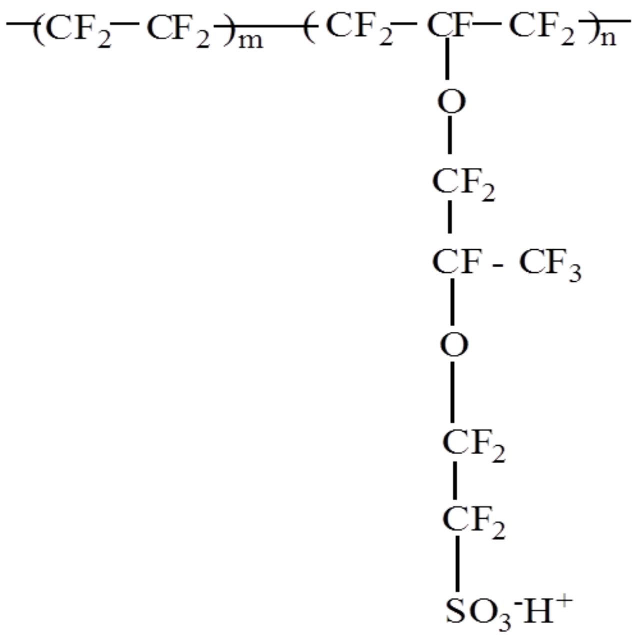

Figure 5-2 Chemical structure of Nafion membrane

Nafion membrane allows positive ions, typically protons, to go through while the electrons are not permitted as a result of 4nm diameter clusters of sulfonate-ended perfluoroalkyl ether groups organized as inverted micelles arranged on a lattice as shown in Figure 5-3 [11]. These micelles are connected by pores or channels of about 1nm in size. These channels with $–SO^{-3}$ groups invoke inter cluster ion-hopping of positively charged species. Studies have shown that proton transport in Nafion depends on water content of the membrane. Proton conductivity in the membrane increases by nearly 6 orders of magnitude from dry to fully hydrated, which is mainly due to the fact that water will bind with the –H in sulfonate group via hydrogen bonding, leaving behind $–SO_3^-$ group. More water means more $–SO_3^-$ groups in the tunnels and thus can enhance the ion conductivity [12]. Improvements in the membrane structure and conductivity are made by producing composite membranes. This can be done by reinforcing the perfluorosulfonic membrane with PTFE components or impregnating a membrane with a solution or a solid powder to decrease the permeability of the reactant gases [13]. Another way is to dissolve the membrane into an appropriate solvent and to mix it with another substance. After recasting the composite membrane can be used in a fuel cell [14].

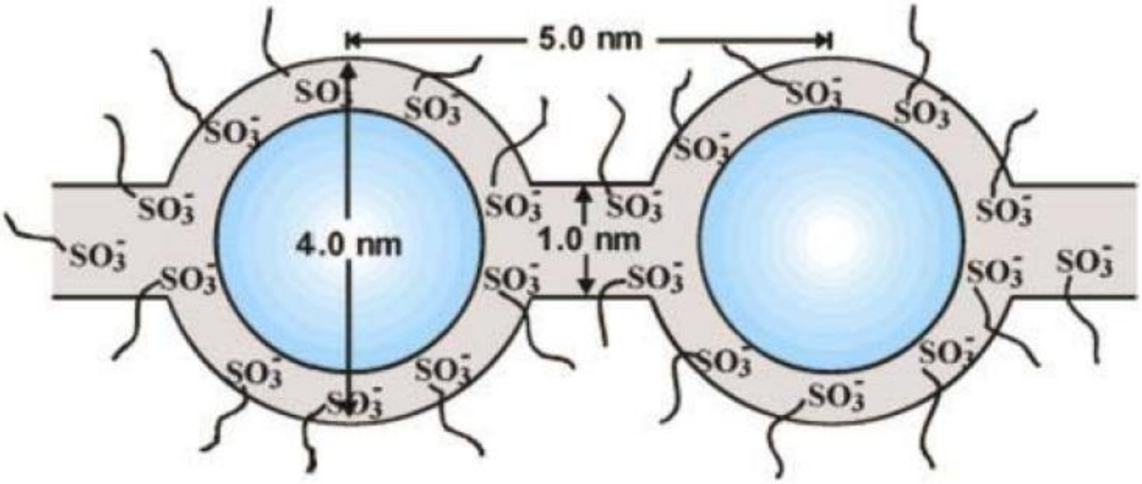

Figure 5-3 Cluster network model inside Nafion membrane. Reproduced from Ref [11].

5.3 Impure gas effect on hydrogen fuel cell

Although the hydrogen oxidation process is a fast electrochemical reaction, some problems may arise in a fuel cell when impure hydrogen is used. Operating a fuel cell with pure hydrogen exhibits the best power output but pure hydrogen is very expensive and difficult to store. Alternatives to pure hydrogen usually come from reformed hydrogen gas from natural gas, propane, or alcohols. Even though the reformed gas is purified, some contaminants, such as carbon monoxide (CO) and carbon dioxide (CO_2) species can persist in the gas feed. Carbon monoxide can poison the catalyst by blocking active sites on the catalyst's surface [15][16]. Consequently, sites are no longer available for hydrogen adsorption and subsequent oxidation. It is known that when CO content is larger than 25 ppm, it has severe effects on Pt catalyst (Figure 5-4) [16].

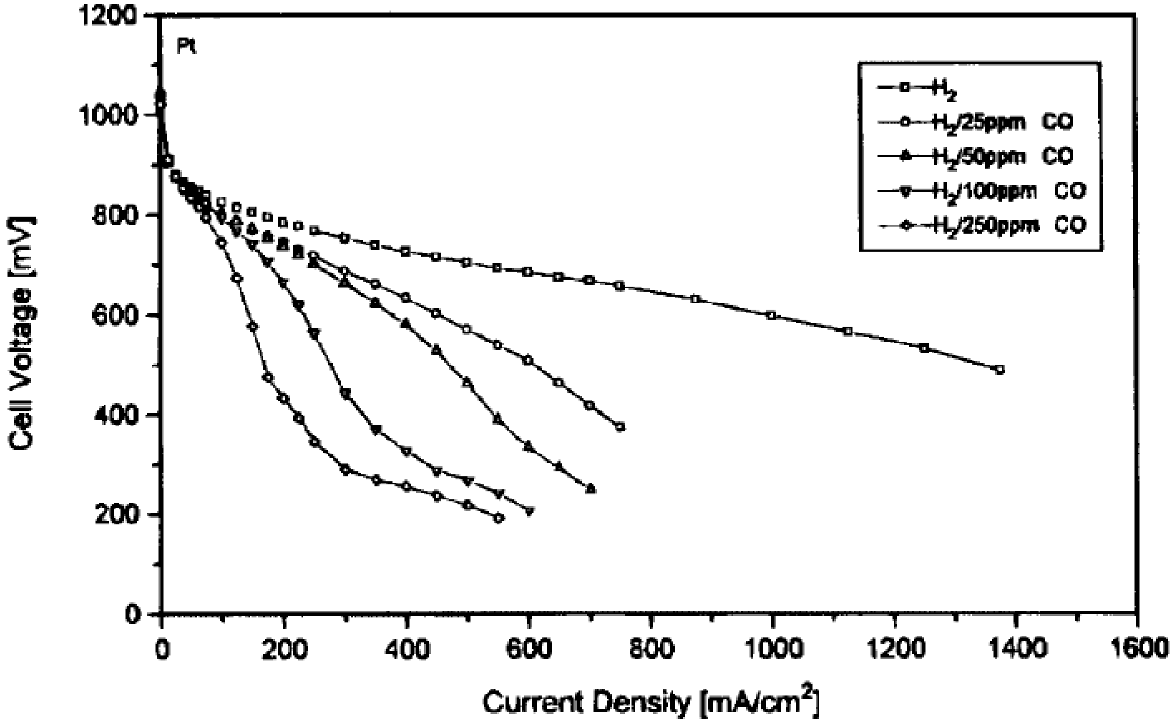

Figure 5-4 Illustration of the effect of CO on a proton exchange membrane fuel cell. Reproduced from Ref [16]

With the presence of carbon dioxide, a reverse water gas shift reaction occurs:

$$CO_2 + H_2 \longleftrightarrow CO + H_2O \qquad (5\text{-}9)$$

The CO content in equilibrium in according to the CO_2 percentage in H_2 is shown in Figure 5-5 [17]. It shows that when the CO_2 content reaches 25%, the concentration of CO is more than 50 ppm. Therefore, both CO and CO_2 can significantly affect the performance of fuel cell. CO and CO_2 resistance system is desired to conquer the negative effects and thus increase the commercial potential of hydrogen fuel cell.

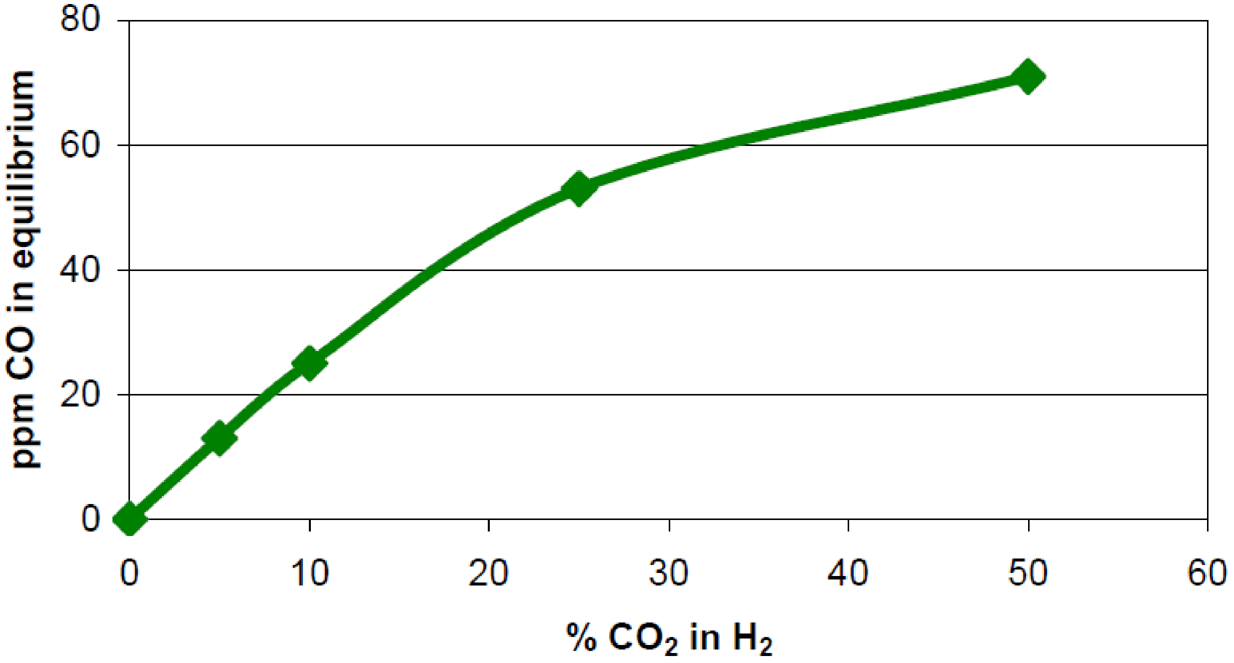

Figure 5-5 CO content in equilibrium in according to CO2 percentage in H2 under 1 bar, 80 ℃ with water saturated. Reproduced from Ref [17].

References

[1] Marcinkoski, Jason, John P. Kopasz, and Thomas G. Benjamin. "Progress in the US DOE fuel cell subprogram efforts in polymer electrolyte fuel cells."*International Journal of Hydrogen Energy* 33, no. 14 (2008): 3894-3902.

[2] Borup, Rod, Jeremy Meyers, Bryan Pivovar, Yu Seung Kim, Rangachary Mukundan, Nancy Garland, Deborah Myers et al. "Scientific aspects of polymer electrolyte fuel cell durability and degradation." *Chemical reviews* 107, no. 10 (2007): 3904-3951.

[3] Carrette, Linda, K. Andreas Friedrich, and Ulrich Stimming. "Fuel cells: principles, types, fuels, and applications." *ChemPhysChem* 1, no. 4 (2000): 162-193.

[4] Barendrecht, Embrecht. *Electrochemistry of fuel cells*. Plenum Press, New York, 1993.

[5] Cha, Suk-Won, Whitney Colella, and Fritz B. Prinz. *Fuel cell fundamentals*. New York: John Wiley & Sons, 2006.

[6] Li, Xianguo. "Principles of fuel cells." *Platinum Metals Rev* 50, no. 4 (2006): 200-1.

[7] Kinoshita, Kim. *Electrochemical oxygen technology, the electrochemical society series*. Wiley, New York, 1992.

[8] Song, Chaojie, and Jiujun Zhang. "Electrocatalytic oxygen reduction reaction." In *PEM fuel cell electrocatalysts and catalyst layers*, pp. 89-134. Springer London, 2008.

[9] Mauritz, Kenneth A., and Robert B. Moore. "State of understanding of Nafion."*Chemical reviews* 104, no. 10 (2004): 4535-4586.

[10] Zawodzinski, Thomas A., Charles Derouin, Susan Radzinski, Ruth J. Sherman, Van T. Smith, Thomas E. Springer, and Shimshon Gottesfeld. "Water uptake by and transport through Nafion® 117 membranes." *Journal of the Electrochemical Society* 140, no. 4 (1993): 1041-1047.

[11] Sahu, A. K., S. Pitchumani, P. Sridhar, and A. K. Shukla. "Nafion and modified-Nafion membranes for polymer electrolyte fuel cells: An overview."*Bulletin of Materials Science* 32, no. 3 (2009): 285-294.

[12] Zaidi, SM Javaid, and Takeshi Matsuura, eds. *Polymer membranes for fuel cells*. Springer, 2009.

[13] Peighambardoust, S. J., S. Rowshanzamir, and M. Amjadi. "Review of the proton exchange membranes for fuel cell applications." *International Journal of Hydrogen Energy* 35, no. 17 (2010): 9349-9384.

[14] Sundmacher, Kai. "Fuel cell engineering: toward the design of efficient electrochemical power plants." *Industrial & Engineering Chemistry Research*49, no. 21 (2010): 10159-10182.

[15] Oh, Se H., and ROBERT M. Sinkevitch. "Carbon monoxide removal from hydrogen-rich fuel cell feedstreams by selective catalytic oxidation." *Journal of Catalysis* 142, no. 1 (1993): 254-262.

[16] Baschuk, J. J., and Xianguo Li. "Carbon monoxide poisoning of proton exchange membrane fuel cells." *International Journal of Energy Research* 25, no. 8 (2001): 695-713.

[17] Janssen, G. J. M., and N. P. Lebedeva. "Carbon dioxide poisoning on proton-exchange-membrane fuel cell anodes." In *Presented at the Conference: Fuel Cells Science and Technology,* vol. 2004, pp. 6-7. 2004.

Chapter 6

Synthesis of Gold Nanoparticles and Nano-sized Gold Platelets

6.1 Introduction

Bulk gold has been studied for decades and it is always considered as inert metal for chemical activity. However, due to the development of nano technology in recent years, it is surprising to find that when the size of gold nanoparticles shrinks to nanometer scale and placed on specific substrate, gold nanoparticles exhibit extraordinary catalytic properties, especially the selective oxidation of carbon monoxide (Figure 6-1). It is clear that the activity is strongly dependent on the size of the Au nanoparticles, and that only catalysts with Au particles below 5 nm show catalytic activity [1]. Furthermore, it can also be seen that the activity varies depending on the support.

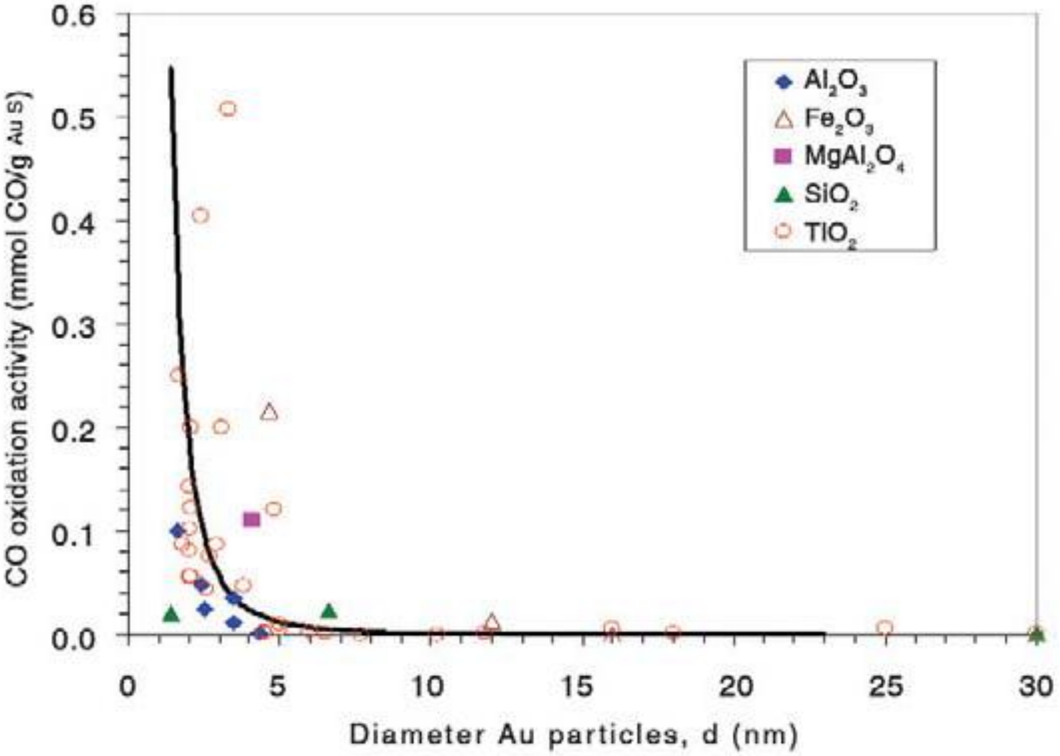

Figure 6-1 Reported catalytic activities (in mmol/gAu s, left axis) for CO oxidation at 273 K as a function of Au particle size (d, in nanometers) for different support materials. The supports are indicated by the symbol shape: open symbols correspond to reducible supports, closed symbols to irreducible supports. The solid curve shows the calculated fraction of atoms located at the

corners of nanoparticles as a function of particle diameter for uniform particles shaped as the top half of a regular cuboctahedron. Reproduced from Ref [1].

Studies have shown that Small particles have a relatively large number of low-coordinated Au atoms, which are located at the edges and, in particular, at the corners of particles [1][2]. The density functional theory (DFT) simulation analysis indicates that these Au atoms are able to bind CO and oxygen, which is a prerequisite for a catalytic reaction [3][4]. It is therefore conceivable that at these sites the CO oxidation reaction is possible at room temperature – the barriers are small and, importantly, the intermediates and CO_2 that are formed are only weakly bound, so it is not necessary to have a high temperature to keep parts of the surface free [5][6][7]. This hypothesis is then confirmed by the investigation of fraction of gold atoms at corner, edges, and crystal faces in according to the size of the gold nanoparticles (Figure 6-2). It is found that only the increasing trend of corner atoms in according to the particle diameter can perfectly match the catalytic activity change due to the change of particle size shown above, which means the fraction of corner atoms with low coordination number plays the crucial role in determining the catalytic activity of the gold nanopariticles for CO oxidation [8][9].

Therefore, in order to make gold nanoparticles active for CO oxidation, it is necessary to limit the size of particles below 5 nm and maximize the fraction of corner atoms with low coordination number. Platelet shape gold nanoparticles can be the promising candidates to achieve the best activity [10][11][12]. In our experiment, thiol-stablized gold nanoparticles are first prepared via classic Burst method, followed by spread onto the water-air interface to construct platelet shaped gold particles. Multiple characterizations have been conducted to prove the formation of such desired gold platelets.

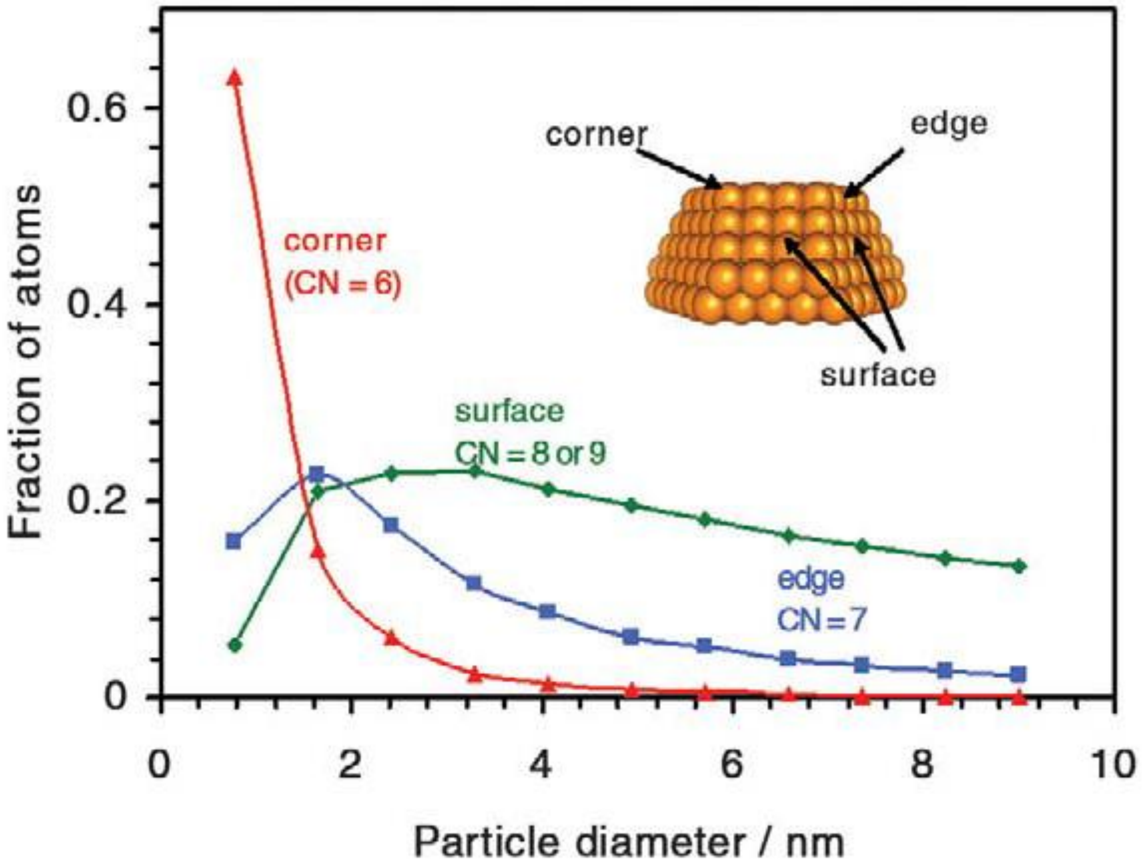

Figure 6-2 Calculated fractions of Au atoms at corners (red), edges (blue), and crystal faces (green) in uniform nanoparticles consisting of the top half of a truncated octahedron as a function of Au particle diameter. The insert shows a truncated octahedron and the position of representative corner, edge, and surface atoms. Reproduced from Ref [2].

6.2 Synthesis of gold nanoparticles via two phase method

The thiol-functionalized gold nanoparticles are synthesized through the two-phase method developed by Brust *et al* [13]. In the two-phase method, an aqueous solution of $H[AuCl_4]\cdot 3H_2O$ (1.1 mmol in 36 mL of H_2O) was mixed with a solution of tetraoctylammonium bromide (TOABr) in toluene (4.8 mmol in 96 mL of toluene). The two-phase mixture was vigorously stirred until all the tetrachloroaurate was transferred into the organic layer. Then 2.0 mmol decanethiol was added into the mixture. A newly prepared aqueous solution of sodium borohydride (12 mmol in 30mL of water) was added at a rate of 2mL/min under vigorous stirring;

the organic phase at the top layer changed color from orange to deep brown within a few minutes. The chemical reaction equations are shown in Equation 6-1 and 6-2. After stirring for 3h, the organic phase was separated and evaporated to 5mL in a rotary evaporator. Then the 5mL concentrated solution was mixed with 200mL ethanol to remove excess thiol and dark brown precipitate was formed at the bottom. The precipitate was got by centrifuging and washed with ethanol four times. It was then dried in a vacuum desiccator over night.

$$AuCl_4^-(aq) + N(C_8H_{17})_4 + (C_6H_5Me) \rightarrow N(C_8H_{17})_4 + AuCl_4^-(C_6H_5Me) \quad (6\text{-}1)$$

$$mAuCl_4^-(C_6H_5Me) + nC_{12}H_{25}SH(C_6H_5Me) + 3me^- \rightarrow 4mCl^-(aq) + (Au_m)(C_{12}H_{25}SH)_n(C_6H_5Me) \quad (6\text{-}2)$$

Figure 6-3 Picture of two phase solution after stirring for 3 hours. The dark phase is toluene phase which contains gold nanoparticles. The transparent phase is water.

6.3 Characterization of gold nanoparticles

6.3.1 TEM sample preparation and characterization

Dried thiol-stabilized gold nanoparticles was dissolved and diluted by toluene. One drop of gold nanoparticles solution was released on 3.05mm copper mesh grid and then dried in the air. Transmission electron microscopy (TEM) measurement was performed on FEI BioTwinG^2 Transmission Electron Microscope. Figure 6-4 shows that uniform size of gold nanoparticles were synthesized by two-phase method. Further calculation by using Image J software gives the core size distribution (Figure 6-4 (b)). The calculated average size of as-prepared nanoparticles is 2.85 ± 0.53 nm. HRTEM image and electron diffraction pattern that shown in Figure 6-5 indicate high crystallinity (fcc) for as prepared gold nanoparticles, with the cell parameter of 4.07 Å, which is almost the same as the standard reference for crystalline gold (4.0786 Å from X-ray diffraction).

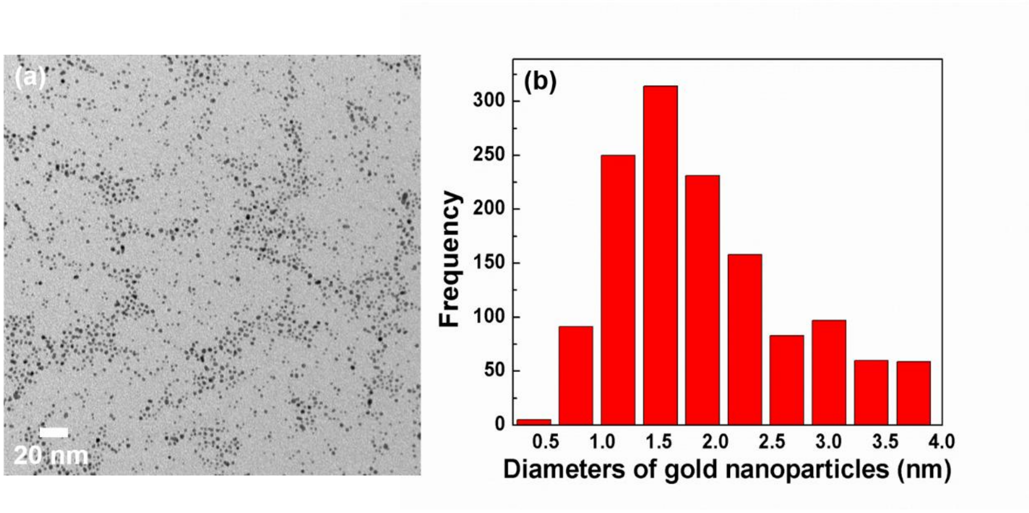

Figure 6-4 (a)TEM images and (b)core size distribution histogram of gold nanoparticles. The average core size is 2.85 ± 0.53nm.

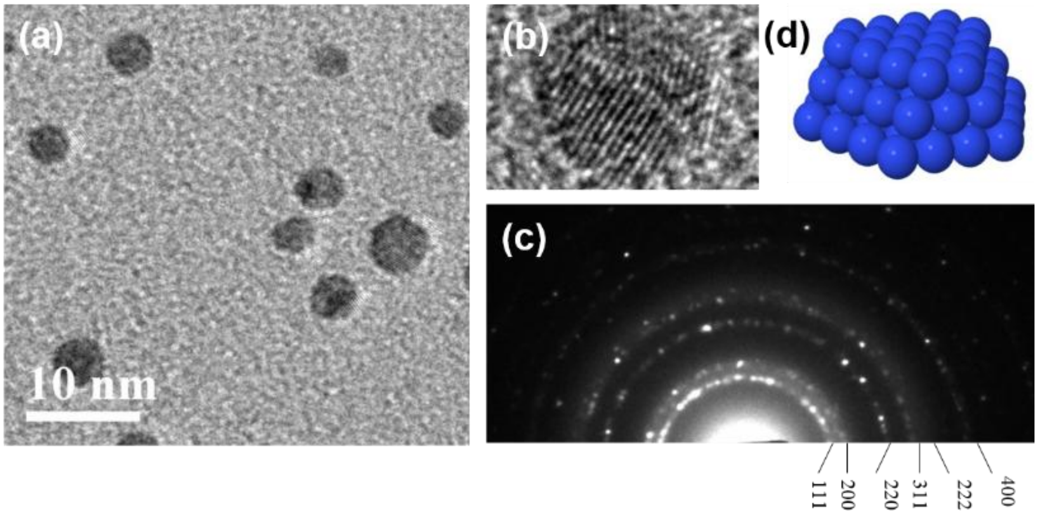

Figure 6-5 (a) HRTEM image of thiol-stabilized gold nanoparticles (b) magnified image of one nanoparticle (c) electron diffraction of the particle.

6.3.2 Langmuir-Blodgett trough

Sun *et al.* have shown that when thiol-protected palladium nanoparticles are dispersed at the interface of water and air, they change shape from sphere to platelet with three layers of palladium atoms [14]. This method may be applicable for gold since its property is similar to palladium. In order to create water-air interface for dispersion of gold nanoparticles, a tool called “Langmuir-Blodgett trough” is utilized. LB trough can be used to build up monolayer of molecules on the surface of water and detect surface pressure behavior due to the compression. It can also be used to deposit single or multiple monolayers onto a solid substrate [15]. The picture of LB trough we used is shown in Figure 6-6. It usually consists of a trough made of Teflon, two compression barriers, surface pressure sensor and substrate holder.

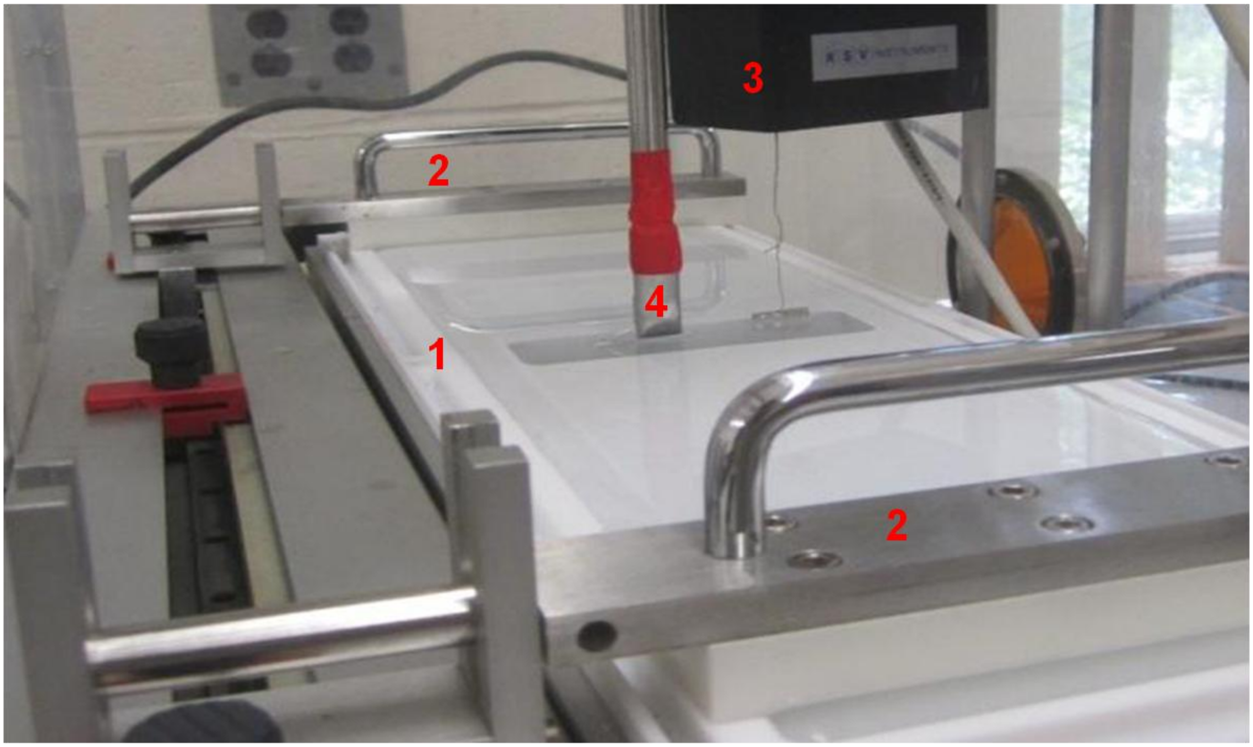

Figure 6-6 Picture of Langmuir-Blodgett trough in the lab, where 1 is Teflon trough, 2 is compression barrier, 3 is surface pressure sensor, 4 is the substrate holder.

The relationship between surface pressure and area for the thiol-stabilized gold nanoparticles was determined by using a KSV 5000 LB trough under room temperature. A 1 mg/ml gold nanoparticles/toluene solution was prepared and 200 μL was spread onto the surface of water by glass syringe. The surface pressure versus area ($\boldsymbol{\pi} - \mathbf{A}$) isotherms of gold nanoparticles is shown in Figure 6-7, where we can see that the surface pressure remains stable at the beginning (gas phase) and goes up sharply later since the molecules are getting close enough to interact with each other (liquid phase) and form a monolayer on the surface. If the barrier continues to compress, the monolayer collapses and part of the layer may go over the other part of the layer and slow down the increasing speed of surface pressure (solid phase). For gold nanoparticles, monolayer starts forming at surface pressure of 1.09 mN/m and collapses at surface pressure of 15.80 mN/m.

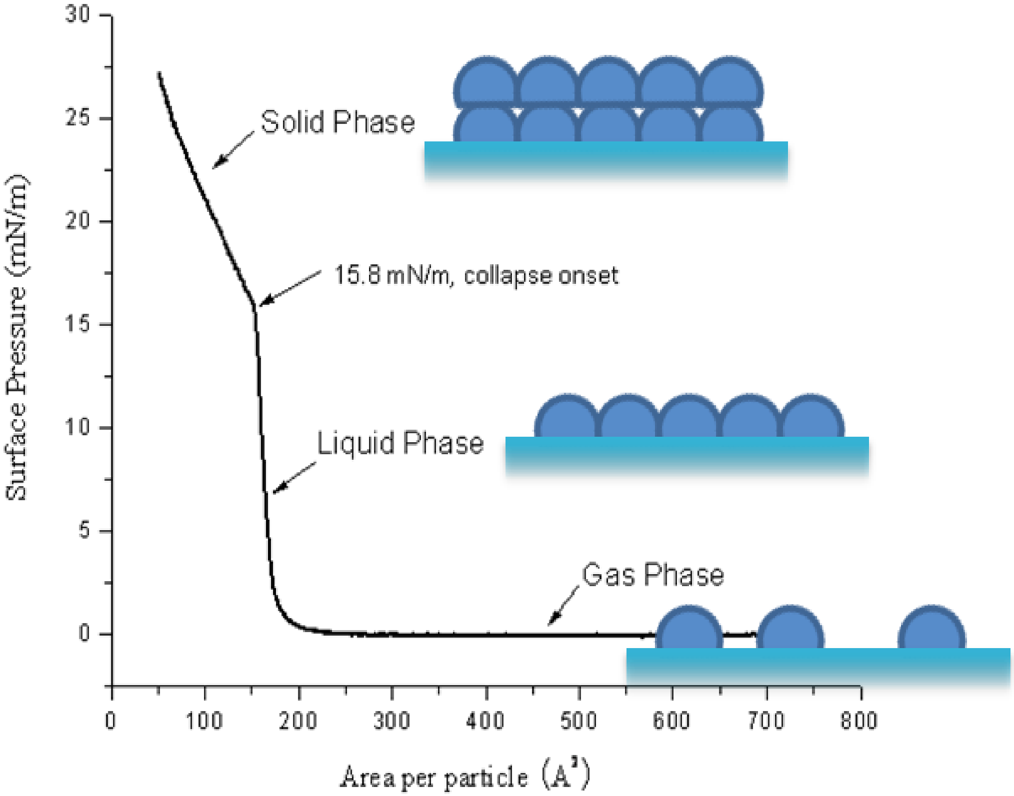

Figure 6-7 Isotherm curve for thiol-stabilized gold nanoparticles. The scheme of different particle distribution on the surface of water is also presented

6.4 Determination of nano-sized gold platelets formation by X-ray reflectivity and TEM

In order to determine whether the gold nanoparticles with platelet shape are really formed at the interface of water and air, the particles have to be deposited onto some substrate and examined in depth profile. Therefore, Si wafers were used as substrate and the layers were deposited onto the substrate at surface pressures of 2mN/m, 3mN/m and 10mN/m. The depth profiles were then measured using the X-ray reflectivity on Beamline X10B at the BNL-NSLS facility. The data together with the curves fitted to the functions are shown in Figure 6-8 and the fitting parameters are shown in Table 6-1. From the results we can see that that at surface pressures of 2 and 3mN/m a monolayer of particles is formed and at the higher pressures of 10mN/m, two layers of particles separated by a layer of thiols, were found to deposit onto the substrate, indicating collapse of the structure. When a single monolayer is deposited the thickness was found to be 1.85 nm, which is significantly smaller than the particle diameter, 2.85 ±0.53 nm, measured from the TEM images obtained from the particles prior to spreading at the air/water interfaces. This layer was found to have thiols only at the air interface and appeared to have only Au at the SiO_2 interface. At the high pressures, the data was best fit to a two layer model, where the first layer was similar in thickness to the monolayer samples, and a second layer, nearly twice the thickness of the first layer, and separated by a layer of thiols, is seen to form above it. In the table we also list the parameters obtained from lifting a monolayer onto the Nafion membrane of a fuel cell, from which we can see that the parameters of the films are the same as those obtained on the Si wafers. The x-ray reflectivity results were also confirmed using TEM analysis of the films lifted from the LB trough. From Figure 6-9 we can see that at the onset of the plateau (2mN/m) the particles form islands scattered along the water surface, and an incomplete layer is seen, at higher pressures (3mN/m) the islands come together, completing the monolayer with uniform surface coverage. At higher pressures a collapsed multi layer structure is seen, as illustrated in the cartoons below each image

Similar results were previously reported for Pd NPs by Sun et al who also analyzed the LB films using extended X-ray absorption fine structure (EXAFS) [14]. The EXAFS data indicated that the particles were initially spherical after synthesis, but those that had been spread at the air water interface assumed an oblate shape, which was best fit to truncated cuboctahedron with a 2:1 aspect ratio. The thickness of the particles deduced from EXAFS was in good agreement with that measured from reflectivity. Hence the Au particles lifted onto the Nafion membrane by this procedure offer a good approximation to platelet morphology of the particles proposed by Mavrikakis *et al* [17]. From the data we can also see that the Au/water interface is highly unstable and when collapsed, the particles recombine to form a layer with the same thickness as the original particles. Hence these particles also had the potential of being highly reactive, and effective at catalyzing, also in agreement with the predictions of Mavrikakis *et al* [18].

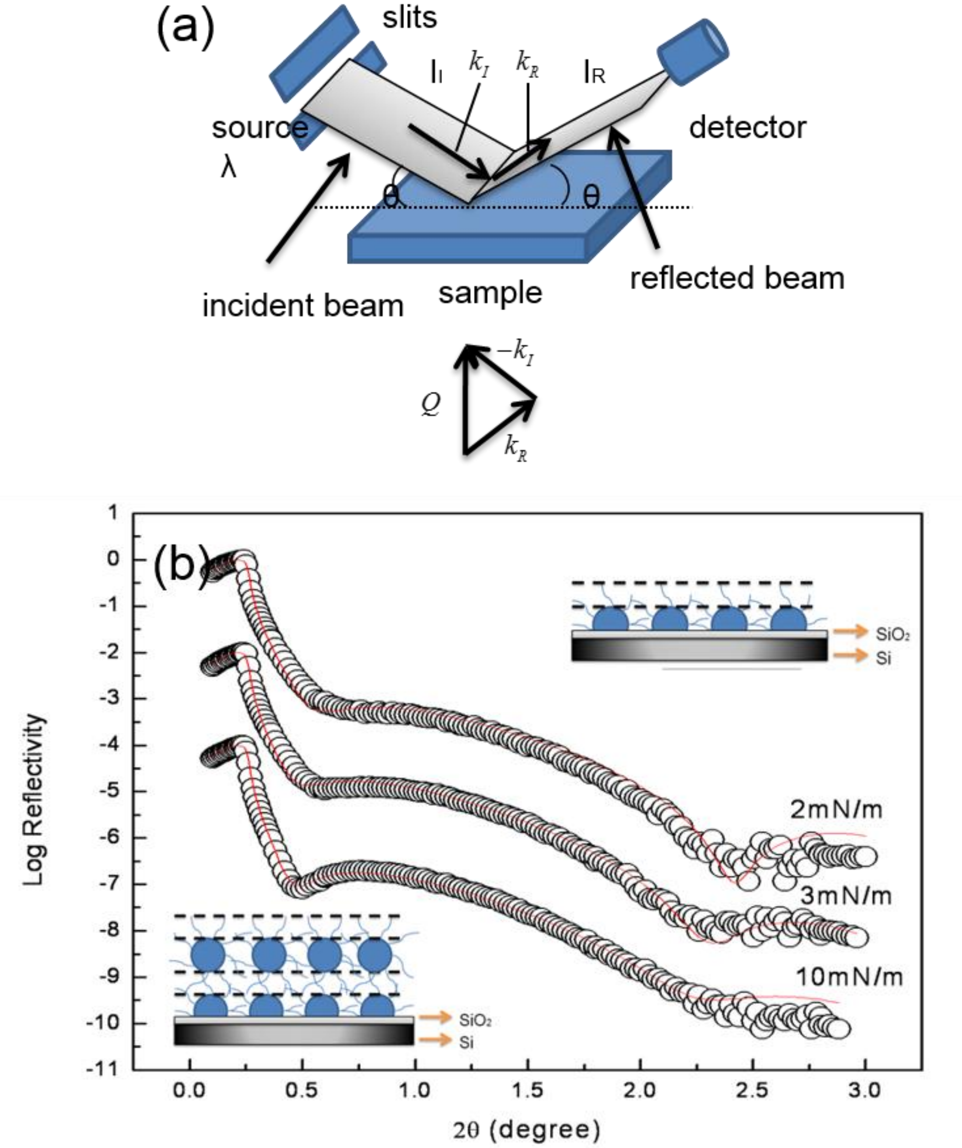

Figure 6-8 (a) Scheme of working principle of X-ray reflectivity; (b) X-ray reflectivity original data (bubble) and fitting curve (red line). The inset is the surface morphology on the substrate.

Table 6-1 X-ray reflectivity fitting parameters for thiol-stabilized gold nanoparitícles, where t is the average thickness of a layer and δ is the dispersion component

	2 mN/m		3 mN/m		10 mN/m	
	t (nm)	δ (×10^6)	t (nm)	δ (×10^6)	t (nm)	δ (×10^6)
Si		2.239		2.239		2.239
SiO_2	1.71	2.31	1.71	2.31	1.71	2.31
Au/thiol	1.58	4.33	1.74	4.33	1.85	4.33
thiol	0.52	0.95	0.62	0.95	0.96	0.95
Au/thiol					3.45	3.03
thiol					0.70	0.85

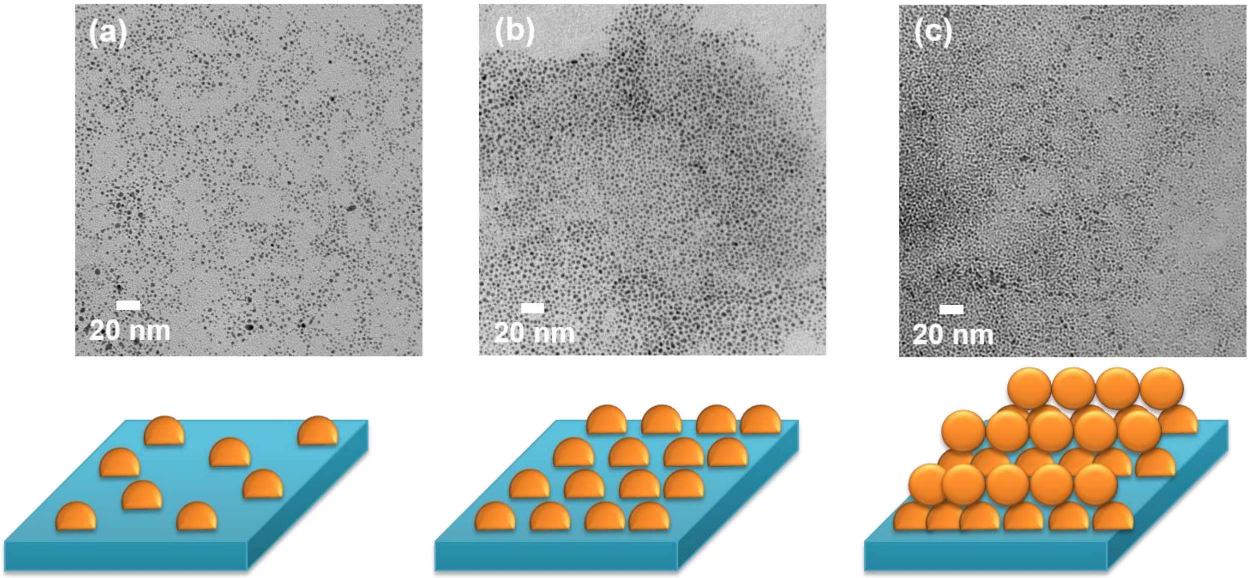

2 mN/m **3 mN/m** **10 mN/m**

Figure 6-9 TEM characterization of LB film lifted up at the surface pressure of (a) 2 mN/m; (b) 3 mN/m; (c) 10 mN/m. The proposed morphologies at different surface pressure are also presented.

References

[1] Hvolbæk, Britt, Ton VW Janssens, Bjerne S. Clausen, Hanne Falsig, Claus H. Christensen, and Jens K. Nørskov. "Catalytic activity of Au nanoparticles."*Nano Today* 2, no. 4 (2007): 14-18.

[2] Janssens, Ton VW, Bjerne S. Clausen, Britt Hvolbæk, Hanne Falsig, Claus H. Christensen, Thomas Bligaard, and Jens K. Nørskov. "Insights into the reactivity of supported Au nanoparticles: combining theory and experiments."*Topics in Catalysis* 44, no. 1-2 (2007): 15-26.

[3] Lopez, Nuria, and Jens K. Nørskov. "Catalytic CO oxidation by a gold nanoparticle: A density functional study." *Journal of the American Chemical Society* 124, no. 38 (2002): 11262-11263.

[4] Barrio, Laura, P. Liu, José A. Rodríguez, Jose Miguel Campos-Martín, and Jose LG Fierro. "A density functional theory study of the dissociation of H on gold clusters: Importance of fluxionality and ensemble effects." *The Journal of chemical physics* 125 (2006): 164715.

[5] Liu, Zhi-Pan, P. Hu, and Ali Alavi. "Catalytic role of gold in gold-based catalysts: A density functional theory study on the CO oxidation on gold."*Journal of the American Chemical Society* 124, no. 49 (2002): 14770-14779.

[6] Remediakis, Ioannis N., Nuria Lopez, and Jens K. Nørskov. "CO oxidation on gold nanoparticles: Theoretical studies." *Applied Catalysis A: General* 291, no. 1 (2005): 13-20.

[7] Cramer, Christopher J., and Donald G. Truhlar. "Density functional theory for transition metals and transition metal chemistry." *Physical Chemistry Chemical Physics* 11, no. 46 (2009): 10757-10816.

[8] Daniel, Marie-Christine, and Didier Astruc. "Gold nanoparticles: assembly, supramolecular chemistry, quantum-size-related properties, and applications toward biology, catalysis, and nanotechnology." *Chemical reviews* 104, no. 1 (2004): 293-346.

[9] Liu, Zhi-Pan, P. Hu, and Ali Alavi. "Catalytic role of gold in gold-based catalysts: A density functional theory study on the CO oxidation on gold."*Journal of the American Chemical Society* 124, no. 49 (2002): 14770-14779.

[10] Haruta, Masatake. "Catalysis of gold nanoparticles deposited on metal oxides." *Cattech* 6, no. 3 (2002): 102-115.

[11] Haruta, Masatake. "When gold is not noble: catalysis by nanoparticles." *The Chemical Record* 3, no. 2 (2003): 75-87.

[12] Cho, Adrian. "Connecting the dots to custom catalysts." *Science* 299, no. 5613 (2003): 1684-1685.

[13] Brust, Mathias, Merryl Walker, Donald Bethell, David J. Schiffrin, and Robin Whyman. "Synthesis of thiol-derivatised gold nanoparticles in a two-phase liquid–liquid system." *J. Chem. Soc., Chem. Commun.* 7 (1994): 801-802.

[14] Sun, Yuan, Anatoly I. Frenkel, Rebecca Isseroff, Cheryl Shonbrun, Michelle Forman, Kwanwoo Shin, Tadanori Koga et al. "Characterization of palladium nanoparticles by using X-ray reflectivity, EXAFS, and electron microscopy."*Langmuir* 22, no. 2 (2006): 807-816.

[15] Ulman, Abraham. "Langmuir-Blodgett Films." *The Handbook of Surface Imiging and Visualization* (1995): 277.

[16] Xu, Ye, and Manos Mavrikakis. "Adsorption and dissociation of O2 on gold surfaces: effect of steps and strain." *The Journal of Physical Chemistry B* 107, no. 35 (2003): 9298-9307.

[17] Mavrikakis, Manos, Per Stoltze, and Jens Kehlet Nørskov. "Making gold less noble." *Catalysis Letters* 64, no. 2-4 (2000): 101-106.

[18] Lopez, Nuria, T. V. W. Janssens, B. S. Clausen, Y. Xu, Manos Mavrikakis, T. Bligaard, and Jens Kehlet Nørskov. "On the origin of the catalytic activity of gold nanoparticles for low-temperature CO oxidation." *Journal of catalysis* 223, no. 1 (2004): 232-235.

Chapter 7

Enhancing the Efficiency of Polymer Electrolyte Membrane Fuel Cell via Application of Gold Platelets

7.1 Introduction

After the preparation method of nano-sized gold platelets is successfully established, the next step is to apply these particles on the PEM fuel cell and test the performance. In order to form a uniform monolayer of gold platelets and possess high catalytic activity, the gold platelets were deposited directly onto the Nafion membrane with flat and hydrophobic surface (Figure 7-1). The membrane was first tested in a fuel cell kit from h-tec with different cathode input gas, followed by test in single stack and three stacks industry use fuel cells. Membranes lift up at different surface pressures were also tested to determine the performance dependence on surface pressure.

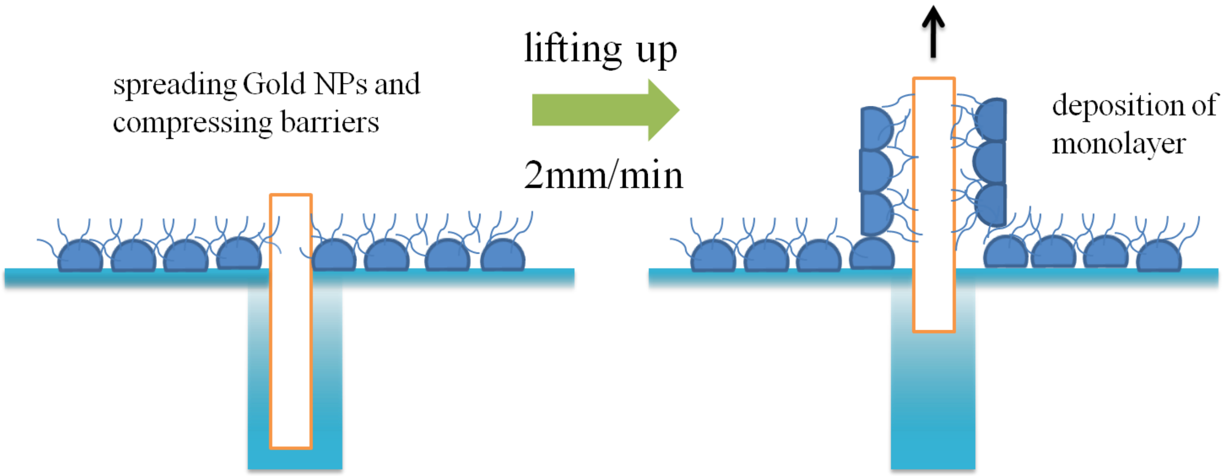

Figure 7-1 Scheme of depositing gold platelets onto the surface of Nafion membrane

7.2 Experiment

A 5cm x 5cm sheet of Nafion 117 was allowed to hydrate for 10 minutes, and then immersed into the Langmuir-Blodgett trough. The solution that contains gold nanoparticels was dispersed all over the surface of water within the trough. After waiting for 10 minutes for the solvent evaporation, the barriers were initiated to compress. Once the coating target pressure had been reached, the dipper was set to pull the Nafion membrane out of the water at a rate of 2mm/min. The coated Nafion membrane was stored in a dry petri dish and sealed until it could be tested in a fuel cell.

The first fuel cells used to test the membranes were demonstration fuel cell kits obtained from h-tec with platinum-coated carbon electrodes. The coated Nafion membrane was secured in the fuel cell and the input hydrogen gas flow rate set to 40ccm at 5 psi pressure. A circuit containing a variable resistance box, ammeter, and voltmeter was connected to the anode and cathode of the fuel cell (Figure 7-2). Air/pure oxygen gas/oxygen-CO_2 mix gas were allowed to enter the cathode respectively. The hydrogen fuel cell was connected and tested at resistances 0Ω, 1Ω, 2Ω, 3Ω, 4Ω, 5Ω, 6Ω, 7Ω, 8Ω, 9Ω, 10Ω, 15Ω, 60Ω, 240Ω, and infinite resistance for the circuit voltage and current. Three data values for current and voltage were collected at each resistance at the point when current and voltage stabilized.

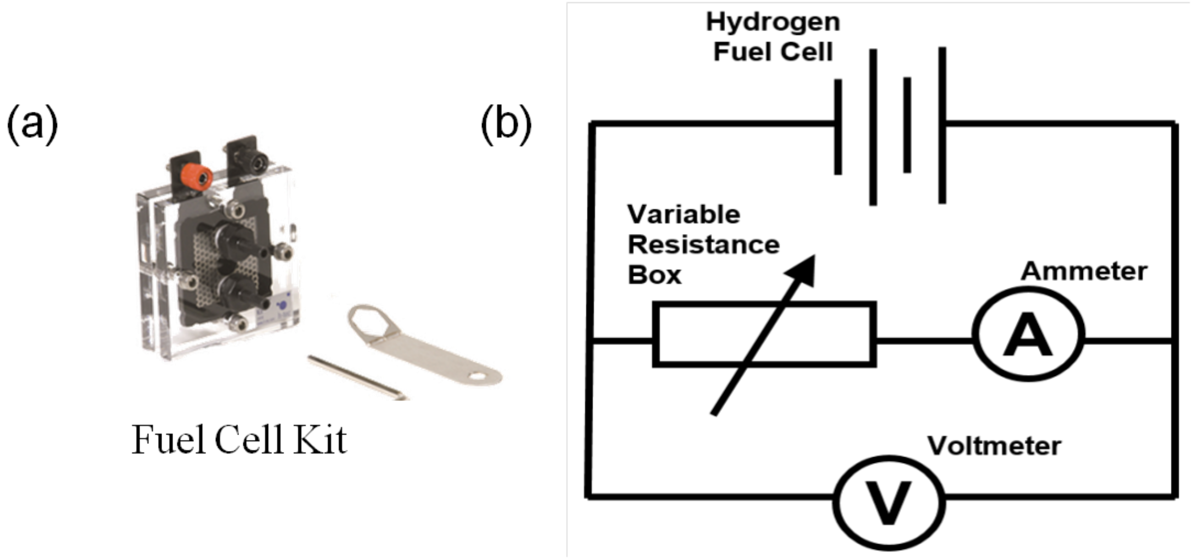

Figure 7-2 (a) Fuel cell kit from h-tec; (b) Electrical circuit for hydrogen fuel cell test station

The coated membranes were then tested in industry use fuel cells, including a single stack fuel cell and three stacks fuel cell with membrane electrode assembly (MEA) and better water management (Figure 7-3).

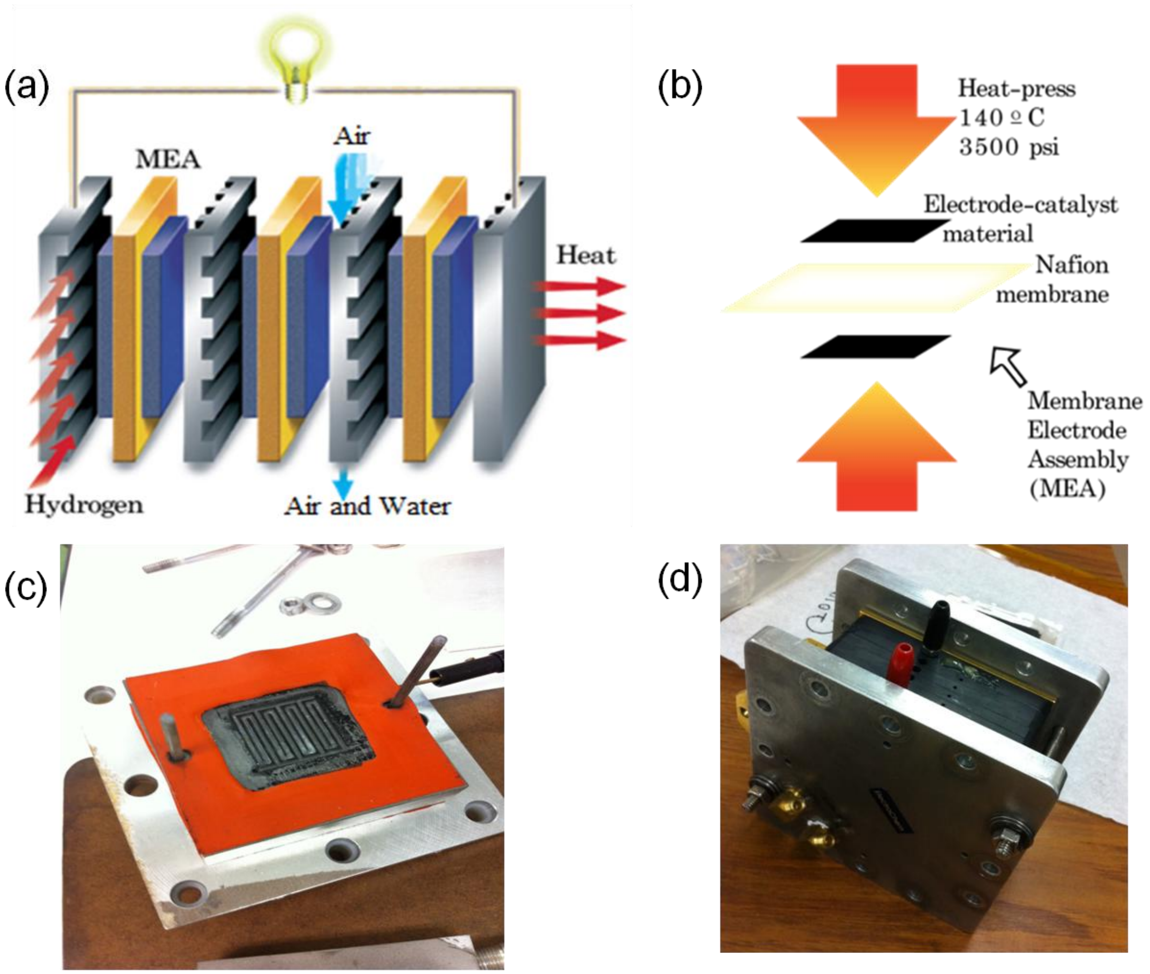

Figure 7-3 (a) Internal structure of industry use fuel cell with water management; (b) Heat press for preparation for membrane electrode assembly (MEA); (c) Single stack fuel cell with 7.8 cm2 active area; (d) Three stacks fuel cell with 50 cm2 active area

7.3 Results and discussion

Membranes with and without Au NPs coatings were then inserted into a single h-tec PEM fuel cell, where the power output could be measured across a variable resistance bridge. The optimum H_2 flow rate, was first determined and found to be 40ccm (cm^3/min) (Figure 7-4). Fast hydrogen flow can accelerate the dry out of Nafion membrane and dramatically reduce the ion conductivity [1] while low flow rate cannot provide enough hydrogen, leading to the worse performance.

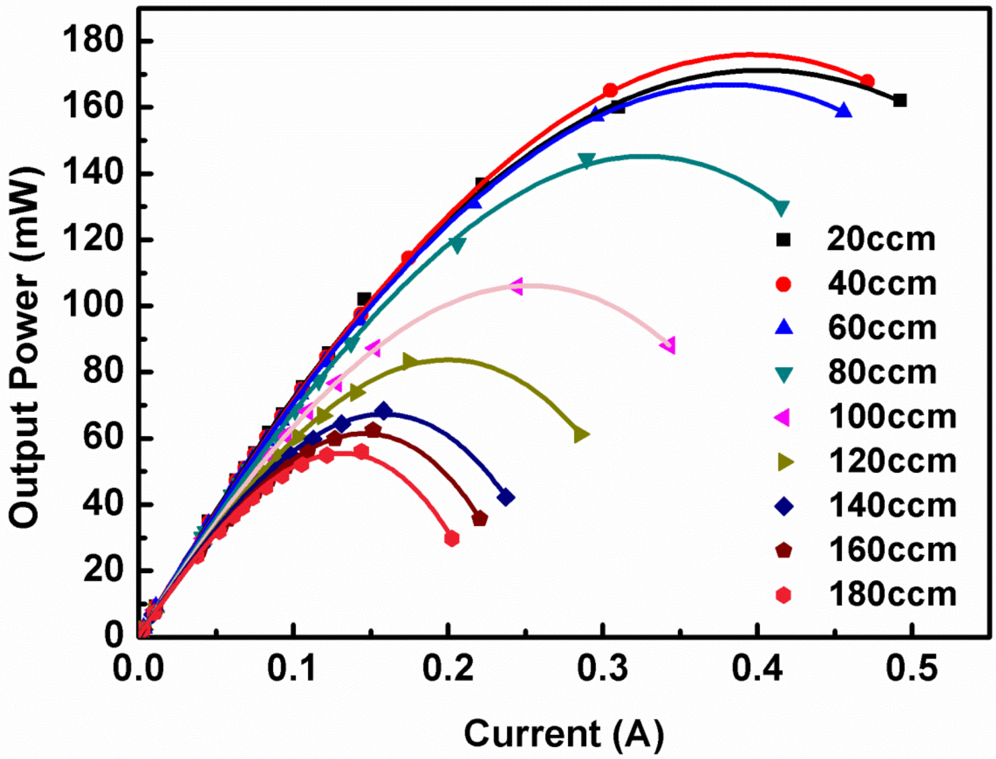

Figure 7-4 Fuel cell performance dependence on flow rates of hydrogen

The fuel cell performance comparison between the fuel cell with pure Nafion membrane and the one with gold coated Nafion membrane is shown in Figure 7-5. The source of cathode gas is the air in the surrounding environment with pressure at atmospheric pressure. The results indicate that with the presence of gold platelet particles, the fuel cell indeed generate about 50% more output power.

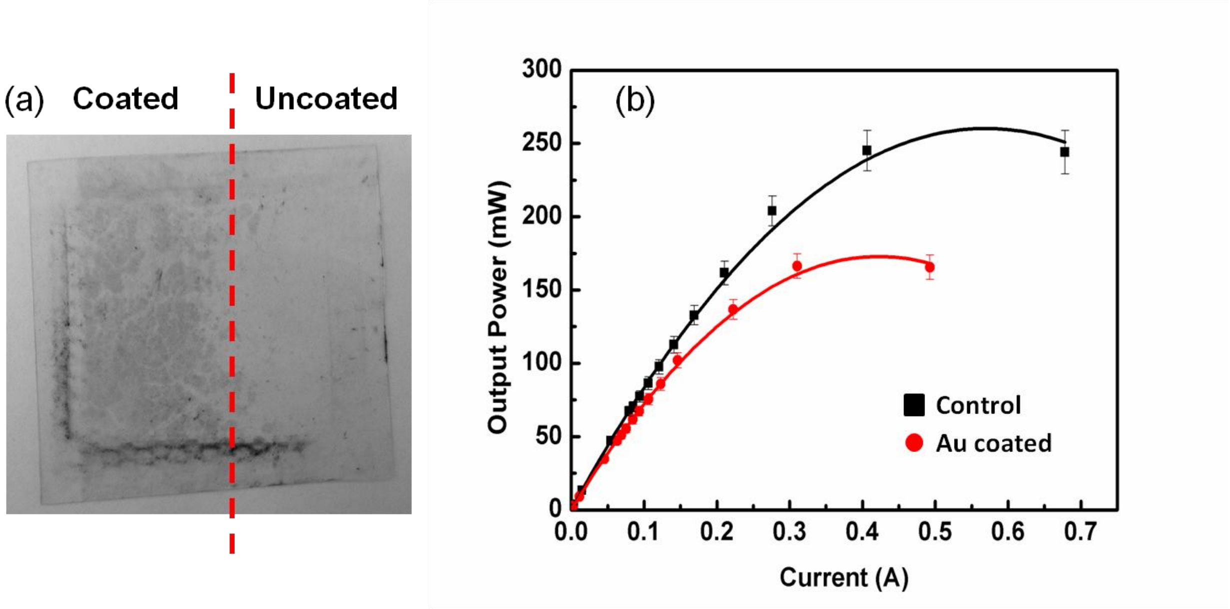

Figure 7-5 (a) Picture of a half coated (left half) Nafion membrane; (b) Fuel cell performance comparison between the fuel cell with pure Nafion membrane and the one with gold coated Nafion membrane.

The gold coated membrane was then heat pressed with electrodes to form MEA and tested in industry use fuel cell. From the Figure 7-6 (a) we can see that single stack cell maximum power output was increased by the presence of NPs from 24 mW/cm^2 to 36 mW/cm^2, while the maximum current was increased from 160 mA/cm^2 to 200 mA/cm^2, or 50% and 25% respectively. In Figure 7-6 (b) we plot the results where the membranes in a 3 stacks cell were coated with particles. Here we see an enhancement of 40% and 55% as well indicating that the stack construct does not interfere with the processes upon which the Au NPs are acting.

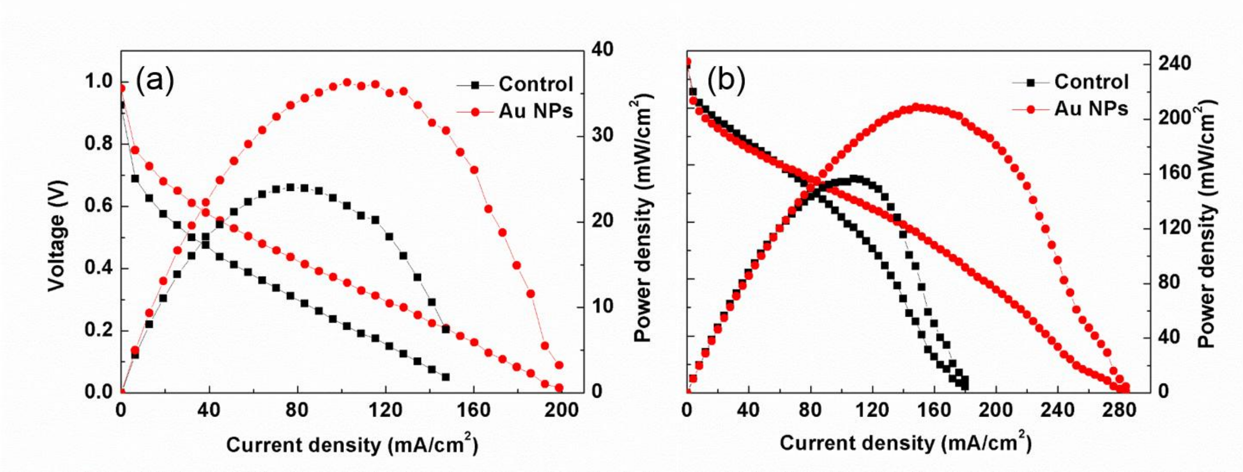

Figure 7-6 Polarization curve and output power density in according to the current density for (a) single stack fuel cell; (b) three stacks fuel cell.

In Figure 7-7 we plot the maximum power output as a function of the pressure with which the Au NPs were lifted from the air/water interface. From the figure we can see that the max power rises monotonically with surface pressure till the pressure corresponding to a complete surface monolayer is reached. Addition pressure, which results in bilayers formation decreases the maximum power, such that when multiple layers have formed the output is reduced to that of the uncoated control, From the X-ray reflectivity results we know that only the first monolayer is in direct contact with membrane. The results show that the power is directly proportional to the surface coverage, as long as a monolayer has not formed. Once the monolayer has formed the output decreases in direct proportion to the formation of the second layer, which seems to block the effect produced by the first layer.

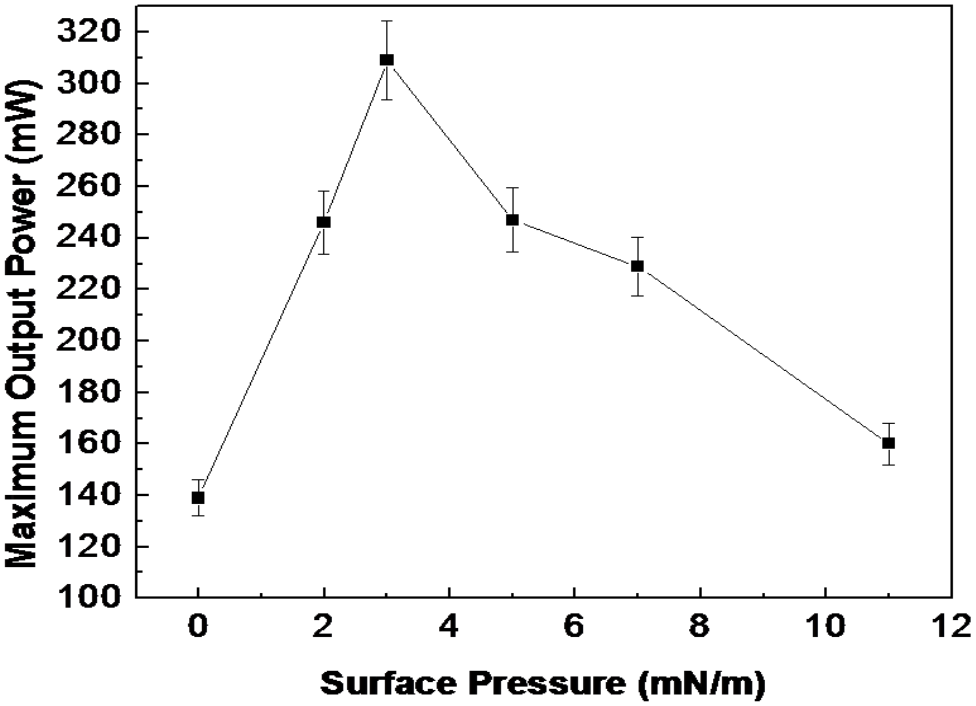

Figure 7-7 Maximum output power dependence on surface pressure chosen to deposit the gold platelets

It is known that the current output of these cells is limited by the buildup of the CO products [2][3][4][5]. It has also been previously established that gold platelets are very effective at catalyzing the CO oxidation reaction. Hence we postulated that the gold nanoparticles on the membrane were effective in catalyzing the reduction of CO back to CO_2, and as predicted by Mavrikakis et al [6][7], only the platelet shaped particles were effective in the catalysis. In order to test this hypothesis, we measured the differential in performance between fuel cells with coated and uncoated Nafion membrane when the cell was operated in pure O_2, air and O_2/CO_2 mixture gas ($O_2 : CO_2 = 6:1$ by volume) at the cathode respectively. The data, plotted in Figure 7-8 shows the relative enhancement, as defined by:

$$\text{Enhancement}= \frac{P_{np}-P_{control}}{P_{control}} \times 100\% \tag{7-1}$$

Where P_{np} is the maximum output power for fuel cell with gold coated Nafion membrane, $P_{control}$ is the maximum output power for fuel cell with pure Nafion membrane. We find that when the content of carbon dioxide in the cathode input gas increases (0% CO_2 content in pure oxygen, more than 300 ppm CO_2 content in air, 14% CO_2 content in the mixture), the gold platelets coating become more effective on enhancing the output power of the fuel cell, which means the function of gold platelets coating here is strongly related to content of carbon dioxide. Considering the catalytic activity of gold platelets on CO oxidation, the possible mechanism is proposed as: the unutilized sites of Pt catalyst may catalyze the reduction of carbon dioxide at cathode side when it accumulates [5][8][9], which leads to the formation of carbon monoxide and blockage of active sites on Pt surface [10][11]. It prevents the adsorption of oxygen and thus reduces the performance of fuel cells. However, with the presence of gold platelets which is proven to be highly selective for carbon monoxide oxidation, this poisoning effect will be minimized and increases the performance of fuel cells. The enhancement that observed for pure oxygen is probably due to the tunneling effect of monolayer of gold that can increase the charge transfer between membrane and electrode as reported in the reference.

$$CO_2 + 2H^+ + 2e^- \xrightarrow{Pt} CO + H_2O \qquad (7\text{-}2)$$

$$CO_{ad} + H_2O \xrightarrow{Au} CO_2 + 2H^+ + 2e \qquad (7\text{-}3)$$

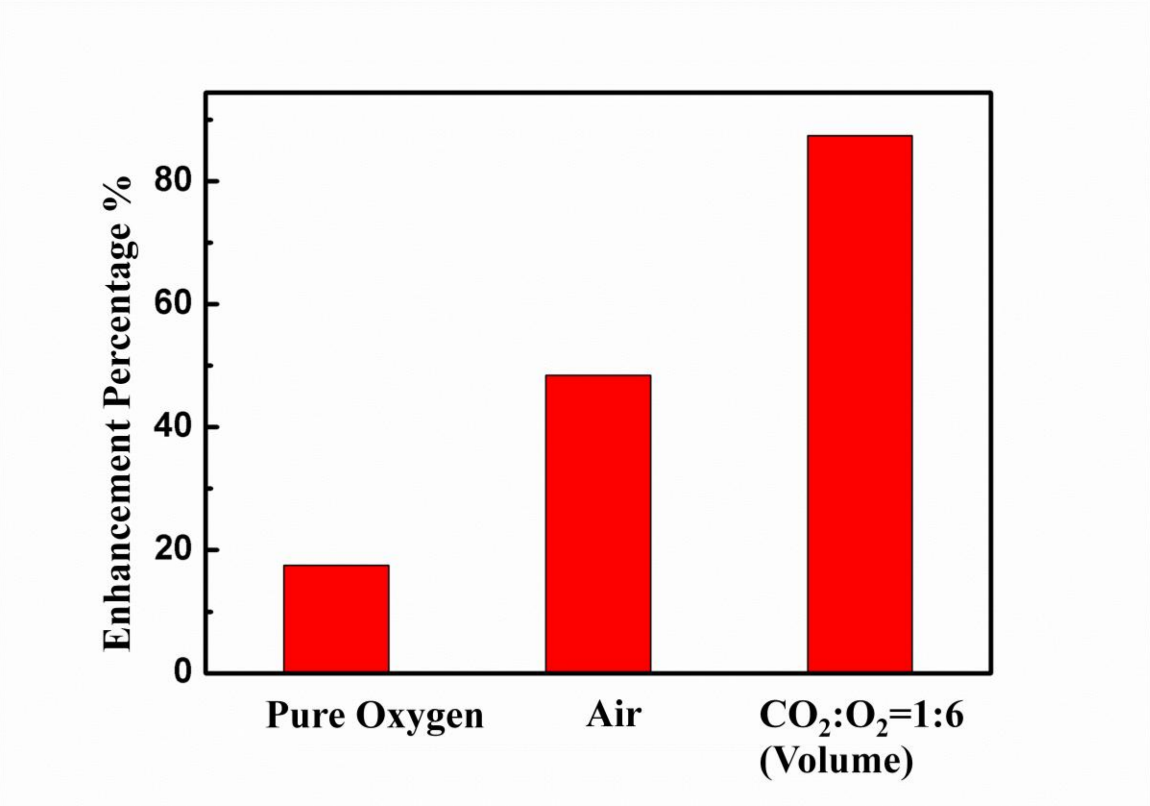

Figure 7-8 Enhancement percentage for fuel cell with pure Nafion membrane and gold coated Nafion membrane in according to the cathode input gas

As discussed in Chapter 5, the hydrogen gas prepared by natural gas reforming usually contains considerable amount of CO_2. If this reformed gas is used in hydrogen fuel cell, reversed water/gas shift reaction will occur and generate CO (Equation 7-4),

$$CO_2 + H_2 \longrightarrow CO + H_2O \tag{7-4}$$

which immediately poisons the catalyst at the anode. It is proven that our gold platelets are effective at oxidizing the CO formed at cathode, so we postulated that it may also take effect at anode side. Therefore, we test the fuel cell with uncoated and gold platelets coated Nafion membrane with H_2/CO_2 mixture gas (14% CO_2 in volume) and compare the performance change with the one using pure hydrogen as anode gas input. The results are shown in Figure 7-9, which indicate that with the presence of gold coating, the performance does not significantly change even there is around 14% CO_2 content in the hydrogen gas, while an obvious performance drop is observed when uncoated Nafion membrane is used. In order to confirm the gold platelets indeed catalyze the CO oxidation reaction, we analyzed the content of carbon dioxide from the output gas of the anode by gas chromatography (Figure 7-10). It is shown that without gold platelets, the CO_2 content decreases, which is mainly due to the reversed water gas shift reaction that consumes $CO_{2.}$ However, with the presence of gold coating, the CO_2 content slightly increases instead of decreasing, which means the gold induced CO oxidation indeed occurs and generates CO_2 as the compensation for the consumption.

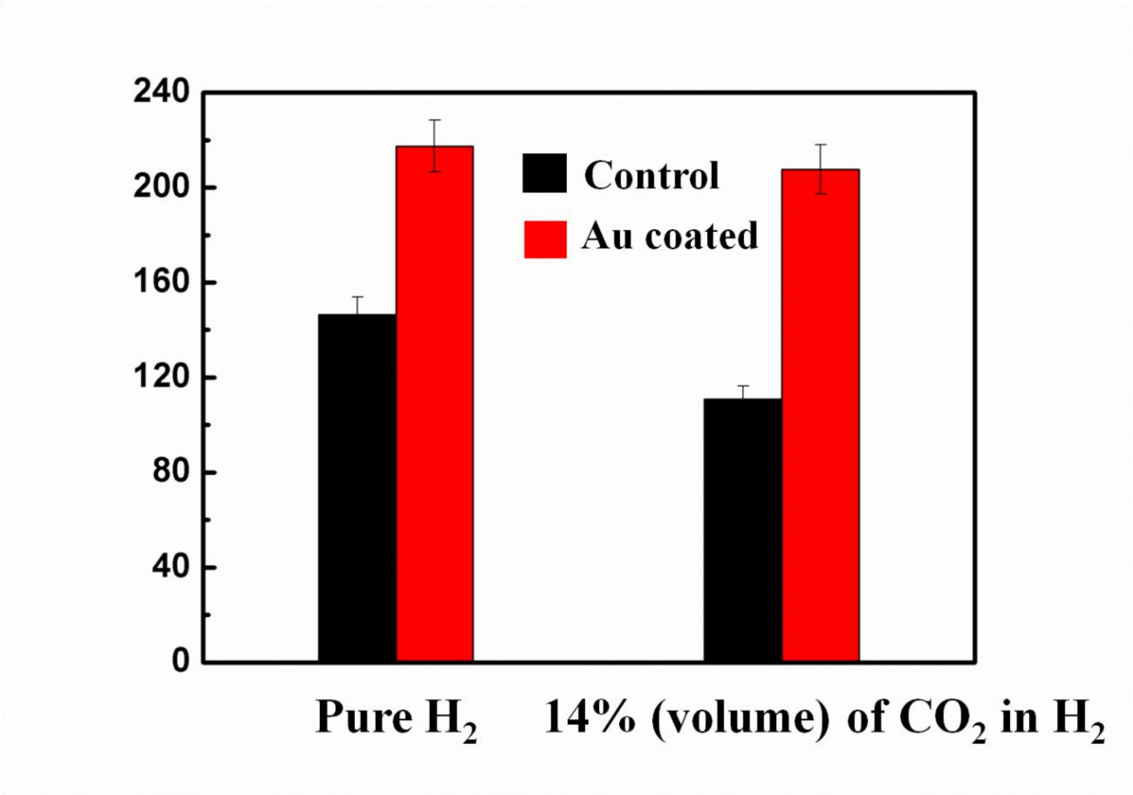

Figure 7-9 Fuel cell performance with uncoated and coated Nafion membrane for pure H_2 gas input and mixture H_2/CO_2 gas input respectively

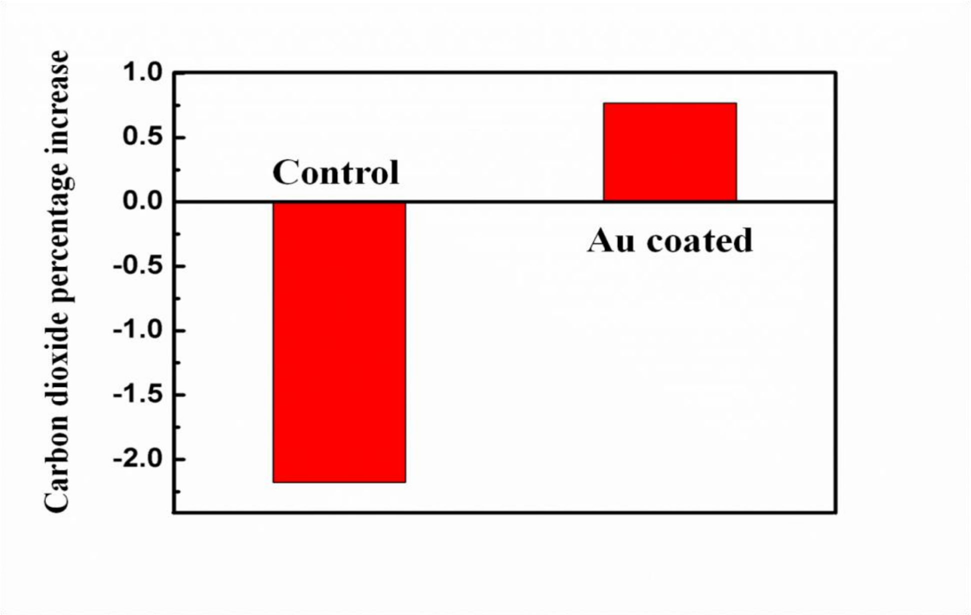

Figure 7-10 Gas chromatography analysis for CO_2 content comes out form the anode side with and without the presence of gold platelets

7.4 Conclusion

In conclusion we have shown that by using LB film technology, it is possible to produce platelet shape gold nanoparticles which act as highly efficient catalysts for the CO oxidation reaction when a monolayer of particles is deposited onto the Nafion membrane of fuel cells and thus dramatically increase the performance of the fuel cell. The particles can also minimize the decrease in fuel cell performance when highly impure streams of H_2 gas are used, making the technology of PEM fuel cells more accessible for commercial use with reformed hydrogen gas.

References

[1] Lee, Woo-kum, Chien-Hsien Ho, J. W. Van Zee, and Mahesh Murthy. "The effects of compression and gas diffusion layers on the performance of a PEM fuel cell." *Journal of Power Sources* 84, no. 1 (1999): 45-51.

[2] Dhar, H. P., L. G. Christner, and A. K. Kush. "Nature of CO adsorption during H 2 oxidation in relation to modeling for CO poisoning of a fuel cell anode."*Journal of the Electrochemical Society* 134, no. 12 (1987): 3021-3026.

[3] Ralph, T. R., and M. P. Hogarth. "Catalysis for low temperature fuel cells."*Platinum Metals Review* 46, no. 3 (2002): 117-135.

[4] Lee, S. J., S. Mukerjee, E. A. Ticianelli, and J. McBreen. "Electrocatalysis of CO tolerance in hydrogen oxidation reaction in PEM fuel cells." *Electrochimica Acta* 44, no. 19 (1999): 3283-3293.

[5] Qi, Zhigang, Chunzhi He, and Arthur Kaufman. "Effect of CO in the anode fuel on the performance of PEM fuel cell cathode." *Journal of power sources* 111, no. 2 (2002): 239-247.

[6] Mavrikakis, Manos, Per Stoltze, and Jens Kehlet Nørskov. "Making gold less noble." *Catalysis Letters* 64, no. 2-4 (2000): 101-106.

[7] Lopez, Nuria, T. V. W. Janssens, B. S. Clausen, Y. Xu, Manos Mavrikakis, T. Bligaard, and Jens Kehlet Nørskov. "On the origin of the catalytic activity of gold nanoparticles for low-temperature CO oxidation." *Journal of catalysis* 223, no. 1 (2004): 232-235.

[8] Baschuk, J. J., and Xianguo Li. "Carbon monoxide poisoning of proton exchange membrane fuel cells." *International Journal of Energy Research* 25, no. 8 (2001): 695-713.

[9] Dhar, H. P., L. G. Christner, A. K. Kush, and H. C. Maru. "Performance Study of a Fuel Cell Pt - on - C Anode in Presence of CO and CO 2, and Calculation of Adsorption Parameters for CO Poisoning." *Journal of the Electrochemical Society* 133, no. 8 (1986): 1574-1582.

[10] Camara, G. A., E. A. Ticianelli, S. Mukerjee, S. J. Lee, and J. McBreen. "The CO poisoning mechanism of the hydrogen oxidation reaction in proton exchange membrane fuel cells." *Journal of The Electrochemical Society* 149, no. 6 (2002): A748-A753.

[11] Ciureanu, Mariana, and Hong Wang. "Electrochemical Impedance Study of Electrode - Membrane Assemblies in PEM Fuel Cells: I. Electro - oxidation of H 2 and H 2/CO Mixtures on Pt - Based Gas - Diffusion Electrodes." *Journal of The Electrochemical Society* 146, no. 11 (1999): 4031-4040.

Chapter 8

Graphene-derivatives Coated Nafion Membrane for Improving the Performance in Polymer Electrolyte Membrane Fuel Cells

8.1 Introduction

Graphene is only one atom thick and arranged in a flat, honeycomb lattice structure [1]. Graphene and its derivative compounds such as graphene oxide and reduced graphene oxide have been of great interest to the researchers for their incredible mechanical, electrical, thermal, and optical properties [2][3][4][5]. Graphene shares the same honeycomb carbon lattice structure as graphite, but instead consists of several graphene layers stacked upon one another. Therefore, the physical properties of graphene are also different from those of graphite [6][7]. At first, graphene was loosely understood for its role in various stacked chemical compounds including graphite intercalation compounds. It was not until the latter half of the 20th century that the separation of graphene drew interest and its properties as an independent material became a topic of study. The first experimental exfoliation of graphene sheets has been attributed to Andre Geim and Konstantin Novoselov for their work at the University of Manchester in 2004 [8]. Geim and Novoselov demonstrated that the mechanical exfoliation of graphene was possible by using of Scotch tape to remove atomic layers from graphite until a single layer remained. In 2010 Geim and Novoselov were awarded the Nobel Prize in Physicsfor their research as it provided key foundational information about the properties of graphene [9][10][11]. Since then, research into the effect of graphene and its derivative compounds on various processes has proliferated.

Graphene oxide and reduced graphene oxide inherit the honeycomb carbon lattice structure of graphene, but are characterized by various functional groups attached throughout their surface [12][13]. Chemically, graphene oxide is derived from graphite oxide and refers to the single layers that are exfoliated from graphite oxide when it is dissolved in a basic solution [14]. Reduced graphene oxide is created when a graphene oxide solution is treated with a reducing agent (Figure 8-1) [15]. Similar to raw graphene, graphene oxide and reduced graphene oxide do not have a specific molecular weight as a result of their lattice structure. The chemical structures of the two compounds have also not been confirmed at the molecular level due to limitations in measuring equipment [16][17].

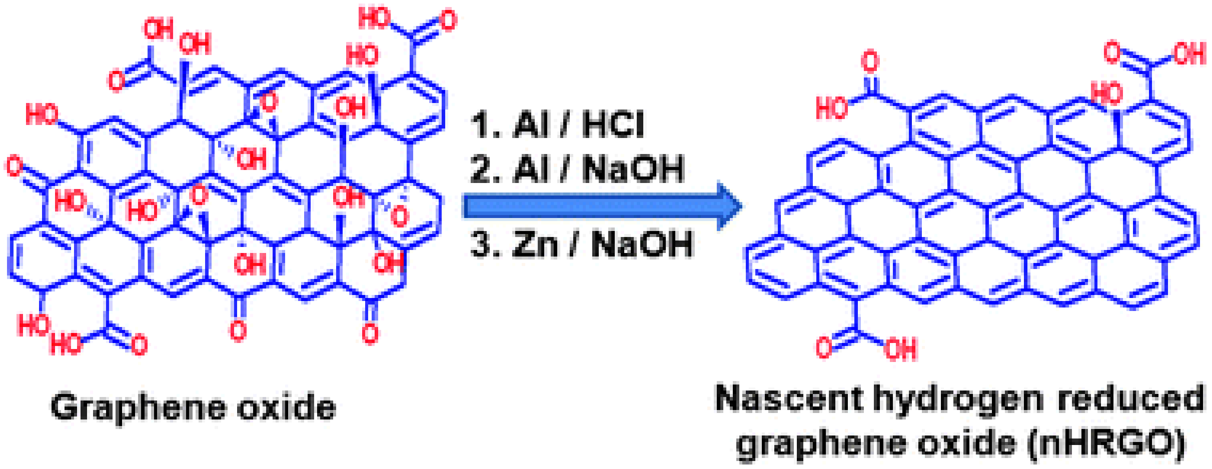

Figure 8-1 One of the chemical reduction ways from GO to rGO. Reproduced from Ref [15].

While the chemical structures of GO and RGO are not completely understood, several of the physical properties of the two substances have been tested experimentally [18][19][20]. When added to a water solvent, graphene oxide is hydrophilic and dissolves readily when sonicated. Graphene oxide is an electrical insulator as a result of its sp^2 hybridized bonding across its surface. Graphene oxide can be suspended in other organic solvents, but often experiences difficulty unless it is further functionalized with diisocyanate and effectively made amphiphilic [21][22].

Reduced graphene oxide is similar to graphene oxide, but has several of its planar functional groups removed either through mechanical or chemical means. An effective reducing agent for graphene oxide is sodium borohydride which has demonstrated an ability to remove most of the hydroxyl and carboxyl groups throughout the surface of the carbon honeycomb lattice [24]. When these functional groups are removed and the graphene oxide is reduced, its properties change dramatically. The reduced graphene oxide becomes more electrically conductive than graphene oxide [25] and also slightly hydrophobic. Both graphene oxide and reduced graphene oxide are valuable for their unique properties as derivative forms of graphene.

Improved production methods have greatly decreased the price of graphene and made interdisciplinary experimentation with graphene compounds possible. However, the effectiveness of graphene oxide and reduced graphene oxide on fuel cell performance when coated on a Nafion membrane has not yet been thoroughly explored.

In this experiment, we apply two derivative forms of graphene, graphene oxide and reduced graphene oxide, to the Nafion membrane in a PEM fuel cell to test if they have any positive effect on fuel cell power output. It will be necessary to find a suitable solvent for graphene oxide and reduced graphene oxide so that the nanosheets can be distributed well on the surface of a Langmuir-Blodgett trough [26]. Also, because of graphene oxide and reduced graphene oxides' tendency to sink to the bottom of the water subphase, suitable procedure must be developed to maximize the concentration of the nanosheets on the surface of the water.

8.2 Materials and Experiments

8.2.1 Synthesis of Graphene Oxide

Solid graphene oxide was synthesized through a modified Hummer's method [27][28] with several of the specificities in both material usage and procedural timings adapted from the methods used by Cote, Kim and Huang [26]with slight modifications reflected below. The solid, dark graphene oxide sheets produced by this procedure are shown in Figure 8-2. One gram of powdered graphite (Bay Carbon Inc., 99%, 200 mesh) was added to 23mL of sulfuric acid (Sigma-Aldrich, 98%) in a battery jar and placed into an ice bath. The mixture was continuously stirred as 0.5 grams of sodium nitrate (Sigma-Aldrich, 99%) and 3.0 grams of potassium permanganate (Sigma-Aldrich, 97%, 325 mesh) were added to it. The battery jar was removed from the ice bath and stirred for one hour at 35 ℃ until the mixture formed a thick, medium-dark paste. Exactly 23mL of de-ionized water was carefully added into the paste causing it to react wildly and jump to a temperature of 95 ℃. After the temperature of the suspension cooled to 60 ℃ (after about 15 minutes), another 35mL of deionized water was added. The dilute suspension was treated with 2.5mL of hydrogen peroxide (Sigma-Aldrich, 30%). A wash of 10mL of hydrochloric acid (Sigma-Aldrich, 36%) was added to the solution and stirred slowly for 5 minutes. The mixture was filtered and the filtrate was washed with de-ionized water six more times before being vacuum-filtered to remove any residual ions. The filtrate was left to dry in a vacuum oven for 48 hours at 80 ℃. The resulting graphene oxide flakes were removed from the inside of the jar using tweezers and transferred into glass vials.

Figure 8-2 Solid graphene oxide sheets in the glass vial.

8.2.2 Preparation of Graphene Oxide and Reduced Graphene Oxide Solutions

An ethanol/water solvent was chosen for the graphene oxide solution because it allowed the graphene oxide nanosheets to readily spread across the surface of the water subphase in the Langmuir-Blodgett trough while keeping the nanosheets from sinking to the bottom. To prepare the graphene oxide solution, a 1:3 ethanol/water solvent was prepared by adding 3.75mL of ethanol (Sigma-Aldrich, 200 proof) to 11.25mL of de-ionized water. The solvent was combined with 15mg of solid graphene oxide then placed into an ultrasonic bath at 40 kHz for 15 minutes. The ultrasound-treated solution was then centrifuged at 3000rpm for 10 minutes. The light amber-colored supernatant, shown on the left hand side in Figure 8-3, was collected and stored for use in the Langmuir-Blodgett trough as the graphene oxide solution. To produce the reduced graphene oxide solution, further treatment of the graphene oxide solution was necessary. A sodium borohydride solution was prepared by adding 1192mg of NaBH4 (Sigma-Aldrich, 98%) to 1.0mL of de-ionized water. With a micropipette, 375μL of the resulting solution were added to the graphene oxide supernatant solution. The solution was left to stir overnight on a magnetic stir plate and removed the following morning when the solution had turned a dark brown color as shown on the right in Figure 4. This reduced graphene oxide solution was stored for use in the Langmuir-Blodgett trough for membrane coating. TEM samples for graphene oxide and reduced graphene oxide are prepared by releasing one drop of the solution onto the TEM grids (Cu, 300 mesh) respectively.

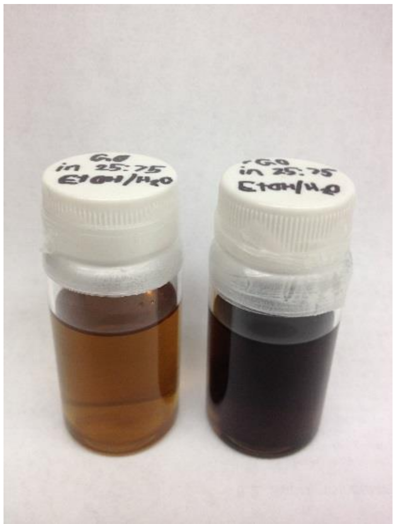

Figure 8-3 Graphene oxide solution (left) and reduced graphene oxide solution (right)

8.2.3 Coating the Nafion Membrane

In order to coat a membrane using the Langmuir-Blodgett trough, it became necessary to develop a procedure that allowed the most amount of graphene oxide or reduced graphene oxide nanosheets to be floated on the surface of the de-ionized water subphase at any time so that they would adhere to the Nafion membrane during the process of barrier compression. As the nanosheets were observed to sink to the bottom of the trough during the barrier compression in previous experiments, we developed an alternate method that involved adding more graphene oxide or reduced graphene oxide solution during the process of the compression. The procedure for adding graphene oxide to the Langmuir-Blodgett trough was identical to that for reduced graphene oxide. 1000μL of the solution was spread evenly across a clean water subphase using a microsyringe. The barrier compression was set at a rate of 5mm/min and started. At 4 minute intervals for the next 36 minutes, 1mL of the solution was added to the Langmuir-Blodgett trough for a total of 10mL, at the end of 36 minutes. This procedure resulted in a clean isotherm curve and allowed a greater number of the nanosheets to remain on the surface of the water during barrier compression.

After an isotherm curve was obtained, it became possible to coat layers of graphene oxide on the Nafion membrane at different target pressures. A 5cm x 5cm sheet of Nafion 117 was allowed to hydrate for 10 minutes, and then lowered into the Langmuir-Blodgett trough. The addition procedure used to obtain the isotherm curve was used again during the coating. Once the coating target pressure had been reached, the dipper was set to pull the Nafion membrane out of the water at a rate of 2mm/min. The coated Nafion membrane was stored in a dry petri dish and sealed until it could be tested in a fuel cell. The first fuel cells used to test the membranes were demonstration fuel cell kits obtained from h-tec with platinum-coated carbon electrodes. The coated Nafion membrane was secured in the fuel cell and the input hydrogen gas flow rate set to

40ccm at 5 psi pressure. A circuit containing a variable resistance box, ammeter, and voltmeter was connected to the anode and cathode of the fuel cell (Figure 7-2). The hydrogen fuel cell was connected and tested at resistances 0Ω, 1Ω, 2Ω, 3Ω, 4Ω, 5Ω, 6Ω, 7Ω, 8Ω, 9Ω, 10Ω, 15Ω, 60Ω, 240Ω, and infinite resistance for the circuit voltage and current. Three data values for current and voltage were collected at each resistance at the point when current and voltage stabilized.

8.3 Results and discussion

8.3.1 TEM characterization

The morphology of graphene oxide and reduced graphene oxide is first observed under the TEM. Since both of them mainly consist of carbon, which is an element with low atomic number, it is difficult to image them under ordinary TEM. Only the places where the fold of nanosheets occurs, there will be some density differential along the vertical direction [1]. In Figure 8-4, this fold can be clearly seen, which confirm the nanosheet morphology for both graphene oxide and reduced graphene oxide.

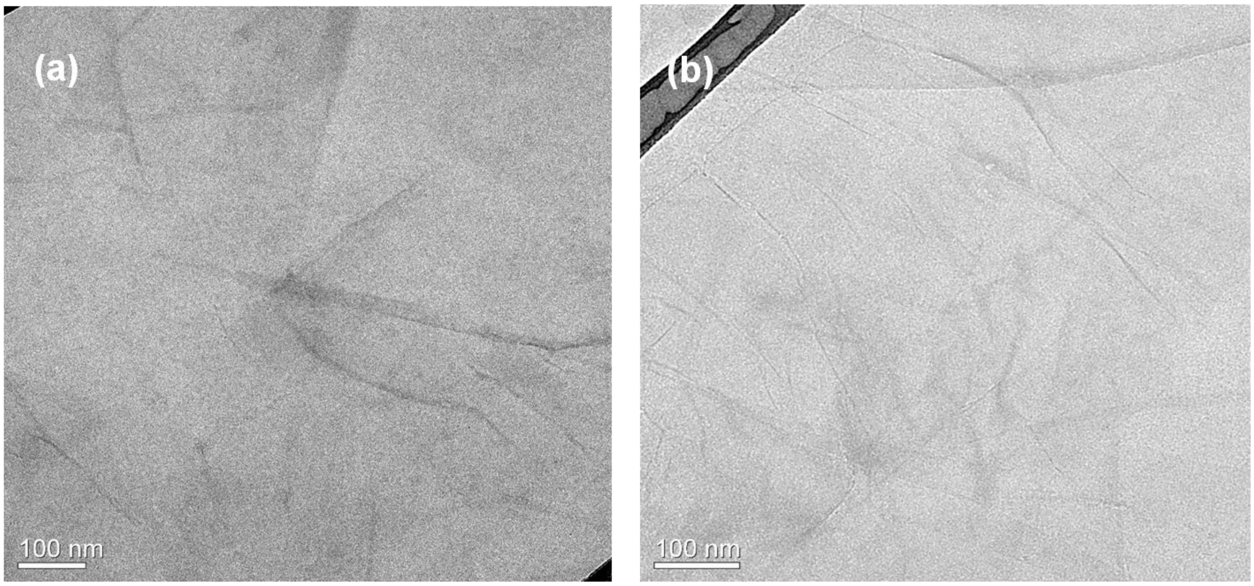

Figure 8-4 TEM characterization of (a) graphene oxide and (b) reduced graphene oxide

8.3.2 LB film preparation and AFM characterization

The isotherm curve for graphene oxide is shown is Figure 8-5. The small spikes before sudden surface pressure change are due to the addition of solution during the compression process. The final surface pressure reaches 18 mN/m, which indicates that our unique procedure can effectively keep a sufficient amount of graphene oxide on the surface of water for the further coating process.

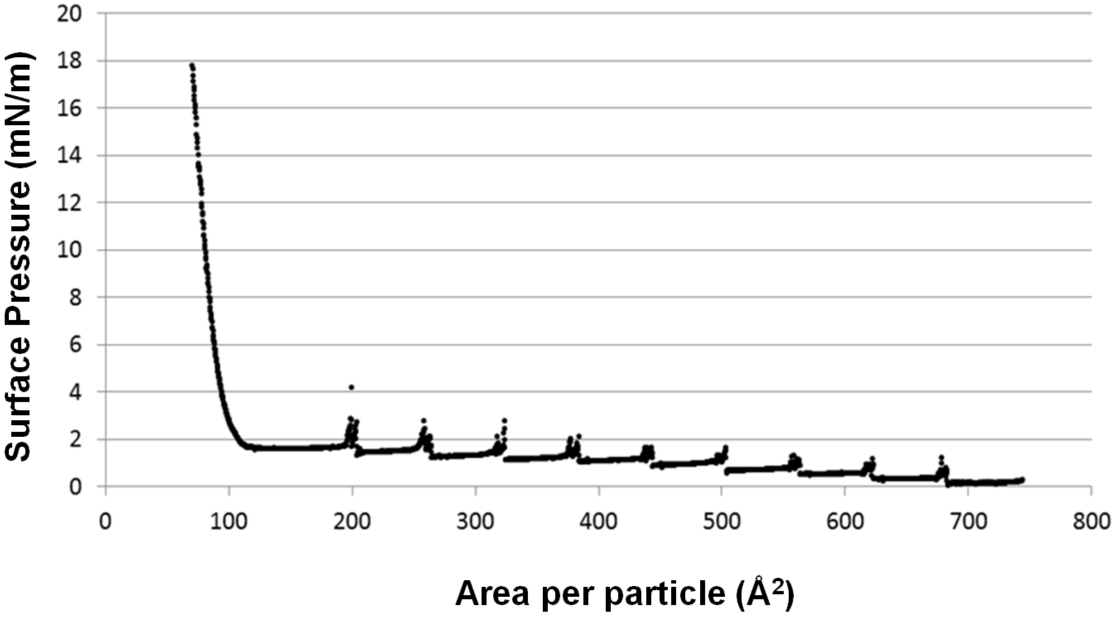

Figure 8-5 Isotherm curve of graphene oxide from Langmuir-Blodgett trough

In order to observe the morphology of GO and rGO coated onto the substrate, we deposited GO and rGO onto silicon substrate at the target surface pressure of 3mN/m, and scanned the surface morphology under atomic force microscopy (AFM). The images are shown in Figure 8-6. For graphene oxide, a lot of small pieces of nanosheets, probably due to the sonication [29], are dispersed all over the surface of the substrate. Reduced graphene oxide seems to have more mechanical strength [30] and larger pieces are found on the surface of substrate even after sonication.

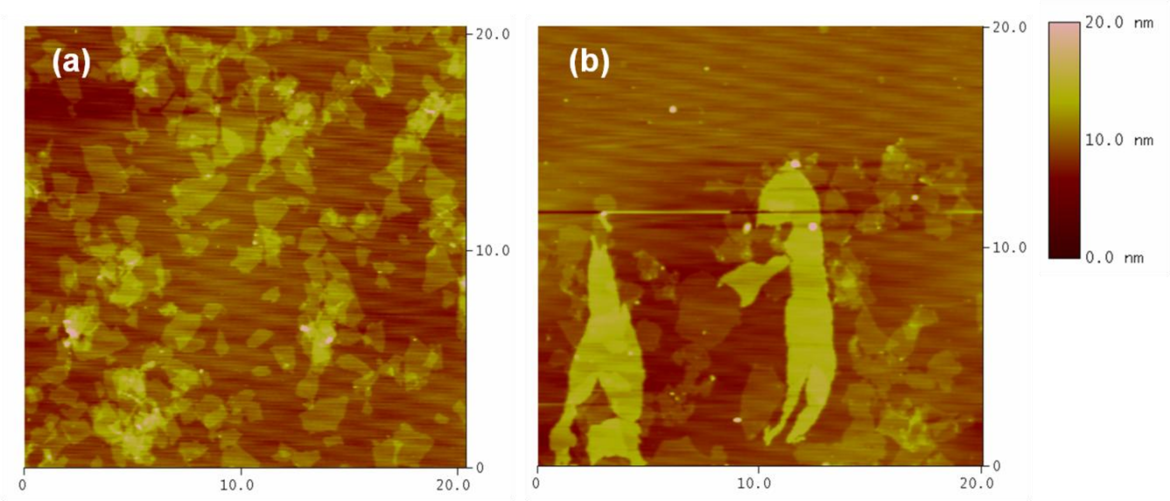

Figure 8-6 AFM characterization of (a) graphene oxide (b) reduced graphene oxide coated onto silicon substrate. The unit for the length scale is µm

8.3.3 Fuel cell performance test

Both of graphene oxide and reduced graphene oxide are then deposited onto Nafion membrane at a surface pressure of 3mN/m. The membranes are inserted to the h-tec fuel cell kit and the fuel cell performance is tested. Significant power enhancement has been observed for the application of coated membrane (Figure 8-7). Both graphene oxide and reduced graphene oxide show positive effects on increasing the performance of fuel cell. Since reduced graphene oxide possess good electronic properties due to its sp^2 conjugated structure [31][32], it has been widely used for transparent electrode for semiconductors [18][33][34]. Moreover, reduced graphene oxide supported platinum catalyst is reported to exhibit high electrochemical activity because the perfect two dimension of rGO could create more active sites exposed for catalyzing [35][36]. In our case, the function of rGO could be either enhancing the electron transportation between membrane and electrode or provide a flat surface support for platinum catalyst or synergistic effects from both. However, for graphene oxide, few reports related to electrochemistry has been reported since sheet resistance of it is extremely high due to the oxygen groups and defects of the structure [13][31]. The investigation of function of GO in enhancing the performance of fuel cell is still ongoing.

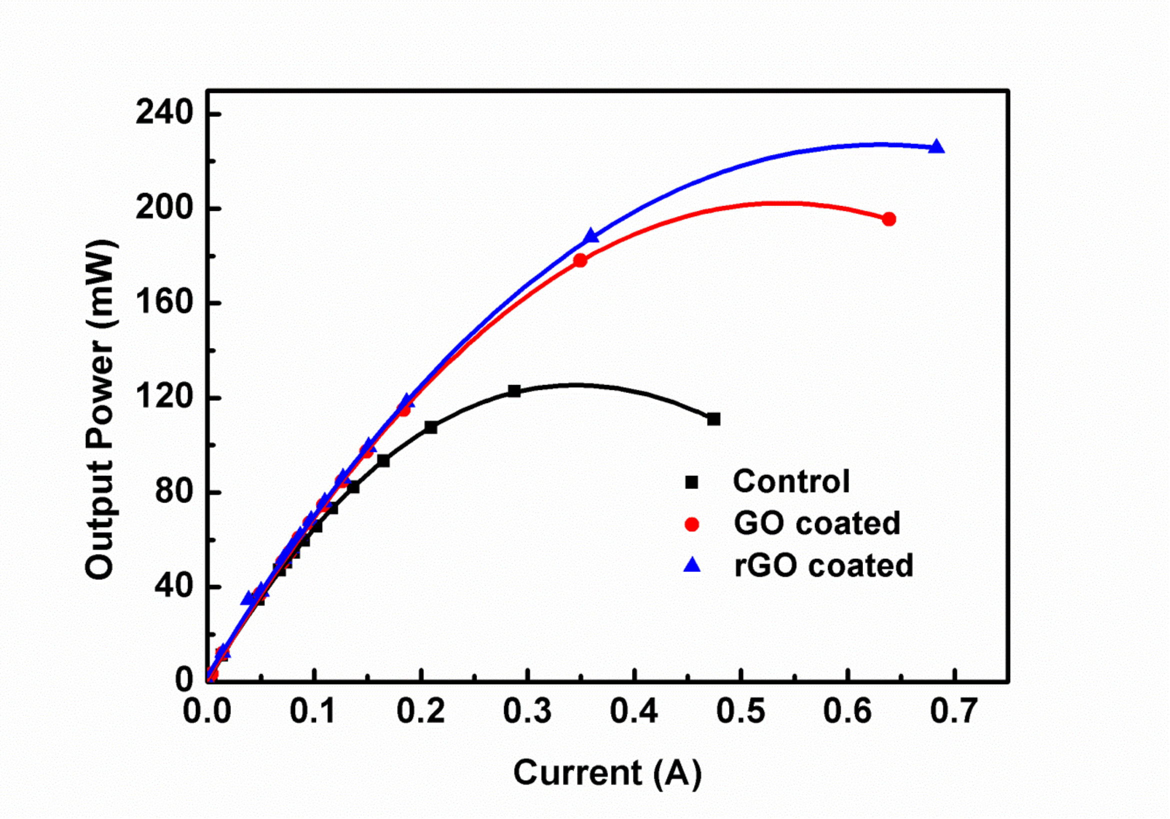

Figure 8-7 Comparison of fuel cell performance between fuel cells that use uncoated, GO coated and rGO coated Nafion membrane

8.4 Conclusion

In conclusion, we successfully coat the Nafion membrane with graphene oxide and reduced graphene oxide nanosheets. Morphologies of them before and after deposition onto substrate are observed via TEM and AFM. The coated Nafion membrane is then inserted into fuel cell and the performance is tested. Interestingly, both graphene oxide and reduced graphene oxide coating are found to significantly enhance the output power of the fuel cell. Function of reduced graphene is explained as either improving the electron transfer within the fuel cell or providing a flat surface for platinum dispersion to expose more active sites. However, mechanism for graphene oxide enhancement still remains unclear. Further research is on progress in the lab.

References

[1] Zhu, Yanwu, Shanthi Murali, Weiwei Cai, Xuesong Li, Ji Won Suk, Jeffrey R. Potts, and Rodney S. Ruoff. "Graphene and graphene oxide: synthesis, properties, and applications." *Advanced materials* 22, no. 35 (2010): 3906-3924.

[2] Chen, Da, Hongbin Feng, and Jinghong Li. "Graphene oxide: Preparation, functionalization, and electrochemical applications." *Chemical Reviews* 112, no. 11 (2012): 6027-6053.

[3] Neto, Antonio Castro, Francisco Guinea, and Nuno Miguel Peres. "Drawing conclusions from graphene." *Physics World* 19, no. 11 (2006): 33.

[4] Suk, Ji Won, Richard D. Piner, Jinho An, and Rodney S. Ruoff. "Mechanical properties of monolayer graphene oxide." *ACS nano* 4, no. 11 (2010): 6557-6564.

[5] Mao, Shun, Haihui Pu, and Junhong Chen. "Graphene oxide and its reduction: modeling and experimental progress." *RSC Advances* 2, no. 7 (2012): 2643-2662.

[6] Pimenta, M. A., G. Dresselhaus, Mildred S. Dresselhaus, L. G. Cancado, Ado Jorio, and R. Saito. "Studying disorder in graphite-based systems by Raman spectroscopy." *Physical Chemistry Chemical Physics* 9, no. 11 (2007): 1276-1290.

[7] Becerril, Hector A., Jie Mao, Zunfeng Liu, Randall M. Stoltenberg, Zhenan Bao, and Yongsheng Chen. "Evaluation of solution-processed reduced graphene oxide films as transparent conductors." *ACS nano* 2, no. 3 (2008): 463-470.

[8] Geim, Andre K., and Konstantin S. Novoselov. "The rise of graphene." *Nature materials* 6, no. 3 (2007): 183-191.

[9] Schedin, F., A. K. Geim, S. V. Morozov, E. W. Hill, P. Blake, M. I. Katsnelson, and K. S. Novoselov. "Detection of individual gas molecules adsorbed on graphene." *Nature materials* 6, no. 9 (2007): 652-655.

[10] Wehling, T. O., K. S. Novoselov, S. V. Morozov, E. E. Vdovin, M. I. Katsnelson, A. K. Geim, and A. I. Lichtenstein. "Molecular doping of graphene." *Nano letters* 8, no. 1 (2008): 173-177.

[11] Mohiuddin, T. M. G., A. Lombardo, R. R. Nair, A. Bonetti, G. Savini, R. Jalil, Nicola Bonini et al. "Uniaxial strain in graphene by Raman spectroscopy: G peak splitting, Grüneisen parameters, and sample orientation." *Physical Review B* 79, no. 20 (2009): 205433.

[12] Sofo, Jorge O., Ajay S. Chaudhari, and Greg D. Barber. "Graphane: A two-dimensional hydrocarbon." *Physical Review B* 75, no. 15 (2007): 153401.

[13] Stankovich, Sasha, Dmitriy A. Dikin, Geoffrey HB Dommett, Kevin M. Kohlhaas, Eric J. Zimney, Eric A. Stach, Richard D. Piner, SonBinh T. Nguyen, and Rodney S. Ruoff. "Graphene-based composite materials." *Nature*442, no. 7100 (2006): 282-286.

[14] Dreyer, Daniel R., Sungjin Park, Christopher W. Bielawski, and Rodney S. Ruoff. "The chemistry of graphene oxide." *Chemical Society Reviews* 39, no. 1 (2010): 228-240.

[15] Pham, Viet Hung, Hai Dinh Pham, Thanh Truong Dang, Seung Hyun Hur, Eui Jung Kim, Byung Seon Kong, Sunwook Kim, and Jin Suk Chung. "Chemical reduction of an aqueous suspension of graphene oxide by nascent hydrogen."*Journal of Materials Chemistry* 22, no. 21 (2012): 10530-10536.

[16] Erickson, Kris, Rolf Erni, Zonghoon Lee, Nasim Alem, Will Gannett, and Alex Zettl. "Determination of the local chemical structure of graphene oxide and reduced graphene oxide." *Advanced Materials* 22, no. 40 (2010): 4467-4472.

[17] Dreyer, Daniel R., Sungjin Park, Christopher W. Bielawski, and Rodney S. Ruoff. "The chemistry of graphene oxide." *Chemical Society Reviews* 39, no. 1 (2010): 228-240.

[18] Eda, Goki, Giovanni Fanchini, and Manish Chhowalla. "Large-area ultrathin films of reduced graphene oxide as a transparent and flexible electronic material." *Nature nanotechnology* 3, no. 5 (2008): 270-274.

[19] Gómez-Navarro, Cristina, R. Thomas Weitz, Alexander M. Bittner, Matteo Scolari, Alf Mews, Marko Burghard, and Klaus Kern. "Electronic transport properties of individual chemically reduced graphene oxide sheets." *Nano letters* 7, no. 11 (2007): 3499-3503.

[20] Robinson, Jeremy T., F. Keith Perkins, Eric S. Snow, Zhongqing Wei, and Paul E. Sheehan. "Reduced graphene oxide molecular sensors." *Nano letters*8, no. 10 (2008): 3137-3140.

[21] Zhou, Ming, Yueming Zhai, and Shaojun Dong. "Electrochemical sensing and biosensing platform based on chemically reduced graphene oxide." *Analytical Chemistry* 81, no. 14 (2009): 5603-5613.

[22] Qi, Xiaoying, Kan‐Yi Pu, Hai Li, Xiaozhu Zhou, Shixin Wu, Qu‐Li Fan, Bin Liu, Freddy Boey, Wei Huang, and Hua Zhang. "Amphiphilic graphene composites." *Angewandte Chemie International Edition* 49, no. 49 (2010): 9426-9429.

[23] Zhou, Ming, Yuling Wang, Yueming Zhai, Junfeng Zhai, Wen Ren, Fuan Wang, and Shaojun Dong. "Controlled Synthesis of Large‐Area and Patterned Electrochemically Reduced Graphene Oxide Films." *Chemistry-A European Journal* 15, no. 25 (2009): 6116-6120.

[24] Shin, Hyeon‐Jin, Ki Kang Kim, Anass Benayad, Seon‐Mi Yoon, Hyeon Ki Park, In‐Sun Jung, Mei Hua Jin et al. "Efficient reduction of graphite oxide by sodium borohydride and its effect on electrical conductance." *Advanced Functional Materials* 19, no. 12 (2009): 1987-1992.

[25] Gilje, Scott, Song Han, Minsheng Wang, Kang L. Wang, and Richard B. Kaner. "A chemical route to graphene for device applications." *Nano letters* 7, no. 11 (2007): 3394-3398.

[26] Cote, Laura J., Franklin Kim, and Jiaxing Huang. "Langmuir− Blodgett assembly of graphite oxide single layers." *Journal of the American Chemical Society* 131, no. 3 (2008): 1043-1049.

[27] William, S., J. R. Hummers, and E. O. Richard. "Preparation of graphitic oxide." *J Am Chem Soc* 80, no. 6 (1958): 1339.

[28] Stankovich, Sasha, Dmitriy A. Dikin, Richard D. Piner, Kevin A. Kohlhaas, Alfred Kleinhammes, Yuanyuan Jia, Yue Wu, SonBinh T. Nguyen, and Rodney S. Ruoff. "Synthesis of graphene-based nanosheets via chemical reduction of exfoliated graphite oxide." *Carbon* 45, no. 7 (2007): 1558-1565.

[29] Park, Sungjin, Jinho An, Richard D. Piner, Inhwa Jung, Dongxing Yang, Aruna Velamakanni, SonBinh T. Nguyen, and Rodney S. Ruoff. "Aqueous suspension and characterization of chemically modified graphene sheets." *Chemistry of Materials* 20, no. 21 (2008): 6592-6594.

[30] Compton, Owen C., and SonBinh T. Nguyen. "Graphene Oxide, Highly Reduced Graphene Oxide, and Graphene: Versatile Building Blocks for Carbon ‐ Based Materials." *Small* 6, no. 6 (2010): 711-723.

[31] Gómez-Navarro, Cristina, R. Thomas Weitz, Alexander M. Bittner, Matteo Scolari, Alf Mews, Marko Burghard, and Klaus Kern. "Electronic transport properties of individual chemically reduced graphene oxide sheets." *Nano letters* 7, no. 11 (2007): 3499-3503.

[32] Tang, Longhua, Ying Wang, Yueming Li, Hongbing Feng, Jin Lu, and Jinghong Li. "Preparation, structure, and electrochemical properties of reduced graphene sheet films." *Advanced Functional Materials* 19, no. 17 (2009): 2782-2789.

[33] Wei, Zhongqing, Debin Wang, Suenne Kim, Soo-Young Kim, Yike Hu, Michael K. Yakes, Arnaldo R. Laracuente et al. "Nanoscale tunable reduction of graphene oxide for graphene electronics." *Science* 328, no. 5984 (2010): 1373-1376.

[34] Eda, Goki, Yun-Yue Lin, Steve Miller, Chun-Wei Chen, Wei-Fang Su, and Manish Chhowalla. "Transparent and conducting electrodes for organic electronics from reduced graphene oxide." *Applied Physics Letters* 92 (2008): 233305.

[35] Sharma, Surbhi, Abhijit Ganguly, Pagona Papakonstantinou, Xiaopei Miao, Meixian Li, John L. Hutchison, Michael Delichatsios, and Sebastian Ukleja. "Rapid microwave synthesis of CO tolerant reduced graphene oxide-supported platinum electrocatalysts for oxidation of methanol." *The Journal of Physical Chemistry C* 114, no. 45 (2010): 19459-19466.

[36] Nie, Renfeng, Junhua Wang, Lina Wang, Yu Qin, Ping Chen, and Zhaoyin Hou. "Platinum supported on reduced graphene oxide as a catalyst for hydrogenation of nitroarenes." *Carbon* 50, no. 2 (2012): 586-596.

Chapter 9

Concluding Remarks and Future Challenge

9.1 Concluding remarks

The warning of “energy crisis” has been proposed due to the public concern about the exhaustion of fossil fuels. It has never been so urgent for the society to look for alternative energy supplies. Renewable energy, such as solar, wind and hydrogen, is considered as the most promising candidate to replace fossil fuels. However, the commercialization of energy devices that utilize renewable energy is limited due to their low power efficiency and cost effectiveness.

The first part of this dissertation focuses on enhancing the efficiency of bulk heterojunction organic solar cell by a novel approach that introduces polystyrene (PS) that organizes the poly(3-hexylthiophene) (P3HT) into columnar phases decorated by [6,6]-phenyl C61-butyric acid methyl ester (PCBM) at the interface. This structure represents a realization of an idealized morphology of an organic solar cell, in which, both exiciton dissociation and the carrier transport are optimized leading to increased power conversion efficiency. This research begins with an idea to build up ideal morphology within active layer for enhancing the efficiency of BHJ solar cell by introducing a second polymer, followed by theoretical simulation- molecular dynamics (MD) simulation to figure out that this morphology can be achieved only when the second polymer is immiscible with neither P3HT nor PCBM. Neutron scattering investigation helps us understand the miscibility between P3HT-PCBM-PS and determine PS is suitable to create columnar structure as indicated from MD simulation results. Then, multiple characterization technologies, including TEM and AFM, are utilized to confirm the formation of proposed structure with the presence of PS. Finally, this structure is applied onto the real BHJ solar cell device and the significant enhancement of power conversion efficiency is observed, which validates our original idea.

The second part of this dissertation focuses on increasing the output power of hydrogen fuel cell by coating the polymer electrolyte membrane-Nafion with gold or graphene-derivatives.

Gold nanoparticles attracts intense of interests due to its active catalytic properties for CO oxidation under room temperature. Meanwhile, the CO poisoning effects limit the commercialization of hydrogen fuel cell since it leads to poor performance, fast degradation and high cost for utilizing pure hydrogen. Therefore, the idea that introduces gold nanoparticles into the hydrogen fuel cell system to resist CO poisoning effect comes out naturally. However, not all gold nanoparticles are active for CO oxidation. As proposed by theoretical and electrochemical chemists, platelet shaped gold nanoparticles with less than 5 nm size possess the highest catalytic activity due to the high fraction of corner atoms on the surface of particles that are considered as active sites. According to the previous research, when thiol-stabilized gold nanoparticles prepared via Brust method are dispersed at the water-air interface, some gold atoms with thiol chain will be removed due to the strong hydrophobic properties of thiol group and become platelet shape. After these references check, we start with the synthesis of thiol-stabilized gold nanoparticles, followed by TEM and HRTEM characterization to confirm they are smaller than 5nm and are crystallized. The as prepared gold nanoparticles are then dispersed on the water surface of Langmuir-Blodgett trough, which helps us create water-air interface and deposit these nanoparticles onto certain substrates, followed isotherm curve measurement for determination of target pressure where monolayer is formed. The silicon wafers coated with gold nanoparticles at different surface pressure are investigated under X-ray reflectivity to check the thickness of deposition layer. Combining with the TEM characterization, the formation of gold platelets on the substrate and distribution of gold nanoparticles on the surface are determined. Finally, these gold platelets are deposited onto the surface of Nafion and tested with fuel cell kit and industry use fuel cell. Results are encouraging that gold platelets coating indeed take effects and dramatically enhance the performance of both fuel cell kit and industry use fuel. In order to fully understand the function of gold platelets, we first vary the cathode gas feed by changing the CO_2 content and find that gold platelets are most active (highest output power enhancement is achieved) when CO_2 content is high. Considering the addition of CO_2 can generate CO at the cathode and poisons the Pt catalyst, it is strong evidence that gold platelets are oxidizing CO to resist poison effects. To see whether gold platelets can also help resist CO poisoning from anode side, we use H_2/CO_2 mixture, which is a common combination in reformed hydrogen gas, as anode gas feed since CO can be generated from reversed water gas shift reaction. It is found that the performance drop is much less when gold platelets are present. The gas chromatography analysis further confirms the occurrence of CO oxidation at the presence of gold platelets.

Graphene and its derivatives are the most popular topics in recent years because they exhibit extraordinary mechanical, electrical, optical, thermal properties, which almost cover every aspect of materials research. However, few reports have been found discussing about the direct deposition of graphene oxide and reduced graphene oxide onto Nafion membrane and its effects. Therefore, we make the Nafion membranes coated with graphene oxide and reduced graphene oxide. Surprisingly, we find both of them can significantly enhance the output power of the fuel cell. Considering their low cost of fabrication and large sources of precursors, they are very promising to reduce the loading of noble catalysts on electrodes and thus lower down the cost fuel cell manufacture.

9.2 Future Challenges

Although the research work described in this dissertation has made a significant progress in enhancing the efficiency of BHJ solar cell and hydrogen fuel cell, there are still many challenges remained to be solved. As for BHJ solar cell, since the polystyrene we use to help create columnar structure is a non-photoactive polymer and electrical insulator, it cannot generate any exciton and may block the carrier transportation where columns are not totally formed. We are considering either to remove it by solvent rinse without changing the morphology or replace it with some photoactive polymer to realize the same structure. However, although we establish the solvent that can only dissolve polystyrene, it is very difficult to keep the columnar morphology after the removal. Meanwhile, the photoactive polymer we found is either very miscible with PCBM or has low solubility in the solvent. Further research has to be conducted to solve these problems. As for hydrogen fuel cell, the function of gold has been figured out by varying gas feed from cathode and anode, but the most direct way should be electrochemical characterization, such as cyclic voltammetry. Theoretical simulation, such as density functional theory, would be another powerful tool to confirm the proposed mechanism. Both of these two methods are also helpful to understand the exact function of graphene oxide and reduced graphene oxide in improving the performance of hydrogen fuel cell.